Performance of Radiation Hard Pixel Sensors for the CMS Experiment

Dissertation

zur

Erlangung der naturwissenschaftlichen Doktorwürde (Dr. sc. nat.)

vorgelegt der

Mathematisch-naturwissenschaftlichen Fakultät

der

Universität Zürich

von

Andrei Dorokhov

aus Russland

Promotionskomitee

Prof. Dr. Claude Amsler (Leitung der Dissertation)

Dr. Roland Horisberger

Prof. Dr. Ulrich Straumann

Zürich, 2005

Abstract

Position sensitive detectors in particle physics experiments are used for the detection of the particles trajectory produced in high energy collisions. To study physics phenomena at high energies the high particle interaction rate is unavoidable, as the number of interesting events falls with the energy and the total number of events is dominated by the soft processes. The position resolution of vertex detectors has to be of few microns in order to distinguish between particle tracks produced in b–quark or τ–decays, because of the short flight path before the decay. The high spatial position resolution and the ability to detect a large number of superimposed track are the key features for tracking detectors. Modern silicon microstrip and pixel detectors with high resolution are currently most suitable devices for the tracking systems of high energy physics experiments.

In this work the performance of the sensors designed for the CMS pixel detector are studied and the position resolution is estimated. In the first chapter an introduction to the LHC and the CMS experiment is given. In addition, the CMS pixel detector and its sensors designs are described. In the second chapter the physical processes in semiconductor position sensitive detectors are discussed and the effects due to irradiation are described. In the third chapter the beam test setup used for the sensors study is presented and the data reconstruction is described. The fourth chapter presents the data analysis and the results. The charge collection efficiency and the Lorentz angle are measured. The charge collection efficiency is about 60% of the unirradiated sensors after a fluence up of $1\times10^{15}\,\mathrm{n_{eq}/cm^2}$. This value drops to 25% after a fluence of $2.6\times10^{15}\,\mathrm{n_{eq}/cm^2}$. The p–spray design and p–stop design with two openings exposed to a fluence of $6\times10^{14}\,\mathrm{n_{eq}/cm^2}$ have a particle detection efficiency of 99% with a threshold of 2000 electrons. The respective value for the p-stop design with one opening is 95%. The Lorentz angle does not depend on irradiation or sensor design but strongly depends on the bias voltage. The Lorentz angle with a magnetic field of 4 T is about 26° for the unirradiated devices and a bias voltage of 100 V. It drops to 8.3° for the sensors irradiated at $1\times10^{15}\,\mathrm{n_{eq}/cm^2}$ and a bias voltage of 600 V.

A new method for the extraction of the electric field in the silicon sensor bulk is developed and applied to the data. The method is based on the measurement of the Lorentz deflection of the charge carriers in the sensor bulk. The measured electric field is implemented in the sensors simulation and the performances of the CMS pixel detector are estimated in the fifth chapter. The simulation is validated with the test beam data and is used to estimate the position resolution of the CMS pixel detector. The resolution of the pixel barrel sensors along the azimuthal angle is in the range between 10 μm and 20 μm. It strongly depends on irradiation and weakly depends on the polar angle of the particle track. The position resolution along the beam direction averaged over the azimuthal angle is in the range between 15 μm and 40 μm. In this case the resolution along the beam direction weakly depends on irradiation and strongly depends on the polar angle of the particle track.

Zusammenfassung

In modernen Teilchenphysikexperimenten werden dünne, hochsegmentierte positionsempfindliche Detektoren benötigt, um die Teilchenspuren zu vermessen, die bei den Kollisionen von hochenergetischen Teilchen entstehen. Zur Untersuchung der physikalischen Erscheinungen bei höchsten Energien ist eine hohe Teilchenrate unumgänglich, da die Anzahl der interessierenden Ereignisse mit ansteigender Energie abfällt und die Gesamtzahl der Ereignisse von Stössen mit relativ kleinem Impulübertrag dominiert wird. Die Positionsauflösung der, dem Wechselwirkungspunkt nächstliegenden, sogenannten Vertex-Detektoren, muss im Bereich von einigen Micrometern liegen, um Teilchenspuren zu erkennen, die aus den Zerfällen von schweren Quarks oder τ-Leptonen stammen. Eine hohe räumliche Positionsauflösung und die Fähigkeit eine grosse Anzahl von Spuren zu trennen sind daher, mit die wichtigsten, grundlegenden Eigenschaften solcher Detektoren. Moderne Silizium-Micro-Streifen- oder Pixel-Detektoren werden diesen Anforderungen gerecht, wodurch sie eine fundamentale Stellung in den meisten Experimenten der Teilchenphysik eingenommen haben.

In dieser Arbeit wurden die Eigenschaften der Prototyp-Silizium-Sensoren untersucht, die im Pixel-Detektor des CMS Experiments am *Large-Hadron-Collider* (LHC) des Europäischen Zentrums für Teilchenphysik (CERN) zur Verwendung kommen werden. Am Ende der Arbeit wird eine Abschätzung der zu erwarteten Positionsauflösung des entgültigen Sensors gegeben. Das erste Kapitel gibt zunächst eine Übersicht über den neuen Ringbeschleuniger LHC und das CMS Experiment. Weiterhin liefert es eine Beschreibung des CMS Pixel-Detektors, sowohl der darin verwendeten Sensoren. Im zweiten Kapitel werden die physikalischen Prozesse besprochen, die in einem positionsempfindlichen Halbleiterdetektors stattfinden, sowie die Effekte, die durch Strahlenschäden eintreten. Im dritten Kapitel wird der Aufbau für die Studien der Sensoren in Teststrahlen und die Datenrekonstruktion beschrieben. Das vierte Kapitel enthält eine Beschreibung der Datenanalyse und der Resultate, insbesondere von Ladungssammeleffizienzen und Lorentzwinkeln. Für Sensoren, die vor den Messungen mit bis zu $1\times10^{15}\,\mathrm{n_{eq}/cm^2}$ bestrahlt wurden, konnten noch 60% der Ladungen nachgewiesen werden, die ein unbestrahlter Sensor produziert. Dieser Wert sank auf 25%, wenn der Bestrahlungsfluss $2.6\times10^{15}\,\mathrm{n_{eq}/cm^2}$ betrug. Sensoren, die mit zweifach-geöffneten *p-stop*-Ringen oder nach dem *p-spray*-Verfahren hergestellt wurden, konnten nach einer Strahlendosis von $6\times10^{14}\,\mathrm{n_{eq}/cm^2}$ und einer Ladungsschwelle von 2000 Elektronen noch 99% aller Spuren nachweisen. Der entsprechende Wert für das Sensordesign mit einfach-geöffneten *p-stop*-Ringen beträgt 95%. Der Lorentzwinkel ist nur schwach abhängig von der Bestrahlung des Sensors, verkleinert sich jedoch mit steigendem elektrischen Feld. Für unbestrahlte Sensoren (285 µm dick) wurde ein Wert von 26° bei einem magnetischen Feld von 4 T und 100 V Detektorspannung bestimmt, für Sensoren einer Bestrahlung von $1\times10^{15}\,\mathrm{n_{eq}/cm^2}$ und 600 V Detektorspannung sinkt der Lorentzwinkel auf 8.3° .

Weiterhin wurde im Rahmen dieser Arbeit eine neue Methode entwickelt, den elektrischen Feldverlauf in einem Sensor zu messen. Dies wurde auf die Daten aus den Teststrahlmessungen angewandt und ist im fünften Kapitel beschrieben. Das gemessene elektrische Feld wurde in einer elektronischen Simulation der Sensoren verwendet, die den Grundstein für eine Bestimmung der Leistungsfähigkeit des CMS Pixel-Detektors darstellt, vor allem der Positionsauflösung. Teststrahldaten wurden benutzt um die Simulation zu verifizieren. In azimutaler Richtung des Pixel-Detektors wurde dafür ein Wert zwischen 10 und 20 µm ermittelt, der stark von der Bestrahlungsstärke und schwach vom polaren Winkel der Teilchenspur abhängt. Die Ortsauflösung entlang der Strahlrichtung, gemittelt über den azimutalen Winkel, liegt

im Bereich von 15 bis 40 µm. In diesem Fall hängt die Ortsauflösung nur schwach von der Bestrahlungsstärke, aber stark vom polaren Winkel ab.

Contents

1. Introduction

1.1. The LHC and the CMS experiment

The Large Hadron Collider (LHC) is an accelerator being built at the European Organization for Nuclear Research (CERN) to explore particle physics beyond energy ranges of previous accelerators. It will reach a center of mass energy of 14 TeV with high luminosity proton beams, 10^{34}protons/cm^{2}s, crossing every 25 ns. This combination of the high energy scale and high event rate (about 20 events per crossing) provides the potential to explore Standard Model (SM) physics and possible new physics beyond it.

There are five experiments around the LHC ring: A Large Ion Collider Experiment (ALICE), A Toroidal LHC ApparatuS (ATLAS), the Compact Muon Solenoid (CMS), the Large Hadron Collider beauty experiment (LHCb) and TOTal cross section, Elastic scattering and diffraction dissociation Measurements (TOTEM). The main focus of the ATLAS and the CMS experiments is the search for the Higgs boson. In addition to their primary goals, studies of CP violating and rare B–decays will also be performed. However, the LHCb experiment primarily designed for B–physics. TOTEM is designed to provide these experiments with the measurement of the total proton–proton cross section, including elastic scattering and diffractive processes. ALICE is a heavy ion experiment aimed to explore the properties of strongly interacting matter at very high energy densities, where the formation of a new phase of matter, the quark–gluon plasma, is expected. The experimentally accessible Higgs decay channels as a function of the mass, m_H, are summarized in Table. 1.1. The branching fractions of the

Mass range	Decay channel
100 GeV $\leq m_H \leq$ 150 GeV	$H \to \gamma\gamma$
90 GeV $\leq m_H \leq$ 120 GeV	$H \to b\bar{b}$ in $t\bar{t}H$
130 GeV $\leq m_H \leq$ 200 GeV	$H \to ZZ^* \to 4l$ (e or μ)
140 GeV $\leq m_H \leq$ 180 GeV	$H \to WW \to l\nu l\nu$
200 GeV $\leq m_H \leq$ 750 GeV	$H \to ZZ \to 4l$
500 GeV $\leq m_H \leq$ 1 TeV	$H \to ZZ \to 2l2\nu$
$m_H \approx$ 1 TeV	$H \to WW \to l\nu + 2jets$
$m_H \approx$ 1 TeV	$H \to ZZ \to 2l + 2b\ jets$

Table 1.1. Experimentally accessible Higgs decay channels as a function of the mass [1].

Standard Model Higgs boson as a function of m_H calculated with HDECAY [2] are shown in Fig. 1.1. The pixel detector provides a tag for b–decays by measuring of the Impact Parameter (Section 1.2). The b–tagging is important for the decay channel $H \to b\bar{b}$ in the associated

production $t\bar{t}H$. For the channels $H \to ZZ^* \to 4l$, $H \to WW \to l\nu l\nu$ the background due to the $Zb\bar{b}$ and $Wb\bar{b}$ channels can be rejected using the b–tagging.

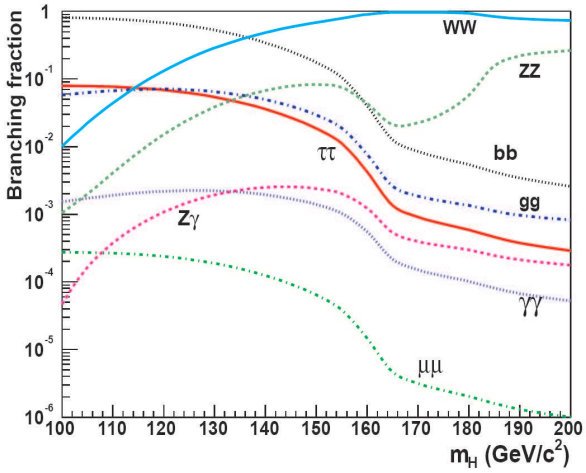

Figure 1.1. Branching fractions of the Standard Model Higgs boson as a function of m_H calculated with HDECAY [2].

The measurements discussed in this work were performed on sensors designed for the CMS experiment. The experiment contains several sub–detectors (Fig. 1.2): silicon pixels and microstrips tracker, electromagnetic and hadronic calorimeters, preshower and muon detectors. The detector contains a high–field superconducting solenoid (4 Tesla) leading to a compact

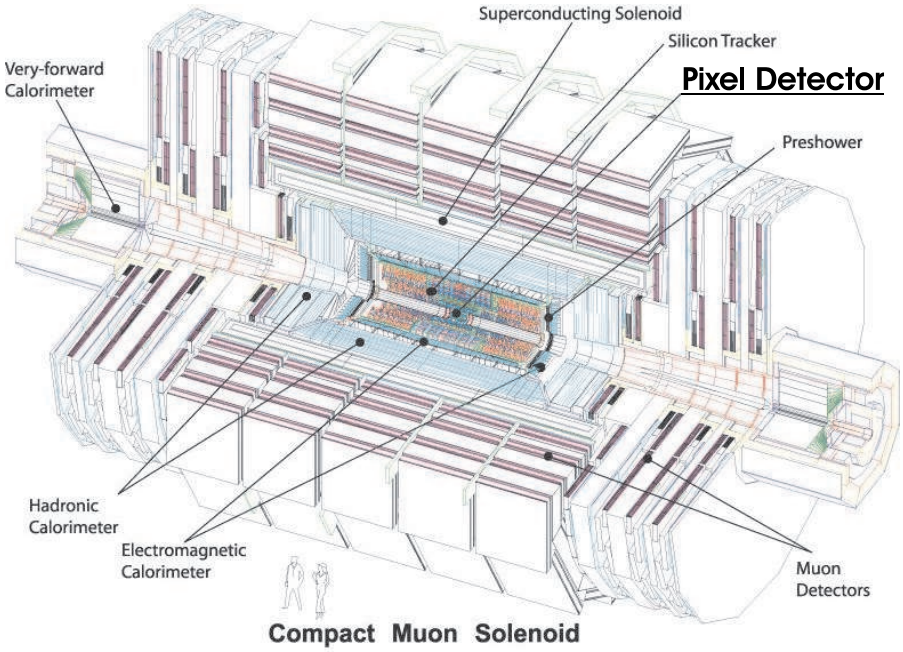

Figure 1.2. Schematic view of the CMS experiment and its sub–detectors.

muon spectrometer. The detector is optimized to identify and measure the energies of muons, photons and electrons. The muon spectrometer system consists of muon chambers. In the barrel part Drift Tube Chambers are used, whereas Cathode Strip Chambers have been chosen for the end–caps. The electromagnetic calorimeter will be built with Lead Tungsten Crystals and the hadronic calorimeter will be made with copper and plastic–scintillator tiles. The electromagnetic calorimeter is used to measure the energy and angular position of photons and electrons, while the hadron calorimeter is used for the detection of hadronic jets.

1.2. The CMS Tracker

A cross section of the tracker quarter is shown in Fig. 1.3. The tracker consists of the pixel and microstrip sub-detectors. The innermost part of the tracker, where the occupancy is very high, is the pixel detector, while the outer part is made of microstrip detector modules. The pixel detector consists of three barrel layers and two disks at each side of the barrel. In order

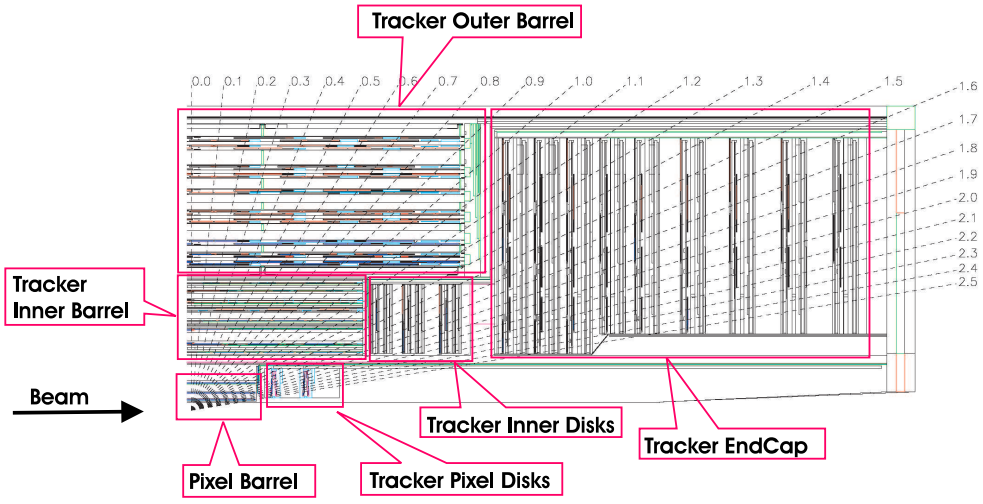

Figure 1.3. Overview of the quarter of the CMS tracker.

to fulfill the experiment primary goals the tracker (Fig. 1.3) needs to achieve an excellent spatial resolution. If the Higgs mass is below 130 GeV it mainly decays into two photons and a precise identification of the primary interaction vertex is needed. If the Higgs mass is above 130 GeV, the transverse momenta p_T of the decay products must be measured precisely: $\delta p_T/p_T < 1.5 \times 10^{-4} p_T(\text{GeV})$ [3]. The transverse momentum is determined from the curvature of the particle track [4] (Fig. 1.4) as

$$p_T = 0.3 z B R, \tag{1.1}$$

where p_T is the transverse momentum in GeV/c, z is charge of the particle in electrons, B is the magnetic field in Tesla and R is the curvature radius in meters. The error on the transverse momentum is

$$\frac{\delta p_T}{p_T} = \frac{\delta R}{R}. \tag{1.2}$$

Using the geometrical relations shown in Fig. 1.4 the error on the curvature radius in the barrel region can be estimated as

$$\frac{\delta R}{R} = \frac{2R\delta y}{r^2}, \tag{1.3}$$

where δy is resolution of a plane in th y direction, r is the radius of the barrel, assuming that the track origins at the center of the barrel and $R >> r$. Using the Eqs. 1.1, 1.2, 1.3 the error

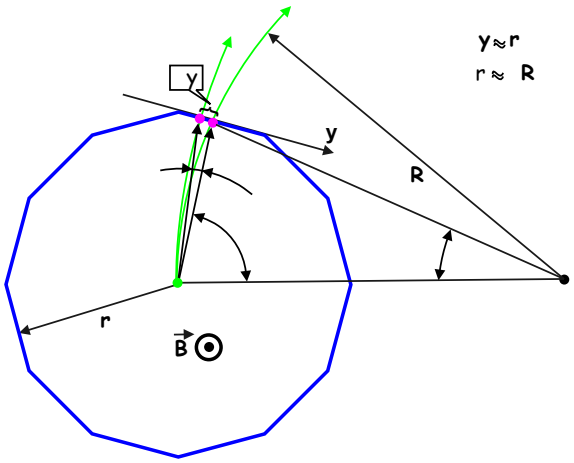

Figure 1.4. Transverse momentum reconstruction. The particle track is shown in green. The error on the position measurement, δy, implies an error on the radius of the track curvature.

on the transverse momentum can be written as

$$\frac{\delta p_T}{p_T} = \frac{2R\delta y}{r^2}. \tag{1.4}$$

Due to the r^{-2} dependence of the error in the transverse momentum, its resolution, is better for the microstrip tracker, because the radius range is 20 cm < r < 110 cm, while the radius range for the pixel detector is 4.3 cm < r < 11.7 cm. However, because of the excellent spatial resolution of the pixel detector (Chapter 5) the pixel detector can be used to improve the transverse momentum resolution, especially for low energy <10 GeV particles.

The most important aim of the pixel detector is to precisely reconstruct the primary interaction vertex and secondary vertices from the decay of short flight–path particles. The primary and secondary vertices can be distinguished by measuring the impact parameter distance (IP) (Fig. 1.5). The impact parameter is

$$IP \approx L\alpha \approx c\tau\gamma\frac{1}{\gamma} = c\tau, \tag{1.5}$$

where c is the speed of light and τ it the flight–time of the particle before the decay. Assuming that the angle α is small and three barrel layers of pixel detector are used for the track reconstruction, the error on the impact parameter can be estimated, for simplicity, from the error of a straight–line fit

$$\delta IP = \delta y\sqrt{\frac{\sum_{i=1}^{3} {r_i}^2}{3\sum_{i=1}^{3} {r_i}^2 - (\sum_{i=1}^{3} r_i)^2}}, \tag{1.6}$$

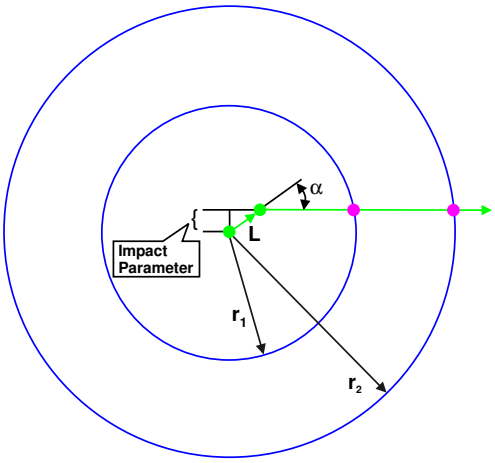

Figure 1.5. Impact parameter reconstruction using two barrel layers of the pixel detector. Particle tracks are drawn in green.

where r_i are the radii of barrel layers. For the CMS pixel detector geometry $\delta IP \approx 2\delta y$. The spatial resolution of the pixel detector is estimated in Chapter 5 and is about 10 µm, therefore the impact parameter resolution is about 20 µm. The impact parameter is $c\tau \approx 100$ µm for τ decays and $c\tau \approx 500$ µm for b decays, and with the spatial resolution of the pixel detector it is therefore possible to distinguish between the primary interaction point and secondary vertices. The complexity of the event topology in CMS (with about 20 minimum bias events) and the enormous number of tracks per bunch crossing require a high granularity tracker system.On average, about 1000 tracks have to be detected every 25 ns, and only the pixel detector can achieve this goal without ambiguity, since pixels cells are placed every 100×150 µm^2.

1.3. The CMS silicon pixel detector

The CMS silicon pixel detector is designed to measure secondary vertices of short–lived particles such as B decays. Therefore it is located very close to the interaction point and is the innermost part of the CMS tracker [5]. The sensors and front end electronics must withstand large doses of radiation. For this reason the sensors were designed using an "n–on–n" concept and frontend electronics are implemented on 1/4 µm technology. The pixel detector is expected to survive and operate without significant degradation for few years. The pixel detector consists of three concentric barrel layers and two end disks, as shown in Fig. 1.6. The barrel layers have radii of 4.4 cm, 7.3 cm and 10.2 cm and are 53 cm in length. The end disks extend from 3 cm to 7.5 cm in radius and are located at ±34.5 cm and ±46.5 cm from the center of the barrel. The barrels and end disks are made up of modules. The total number of pixels is 66×10^6, of which 48×10^6 are in the barrels.

The charge sharing (along ϕ) in the barrel modules is due to the Lorentz force in presence of the magnetic field. While, the modules in the disks are tilted by 20° in a turbine–like geometry to increase charge sharing between pixels. The barrel detector modules are composed of a sensor bump bonded to 16 readout chips glued to a base plate, also shown in Fig. 1.6. Each readout chip is responsible for the read out of a 80×52 pixel array. The base plates

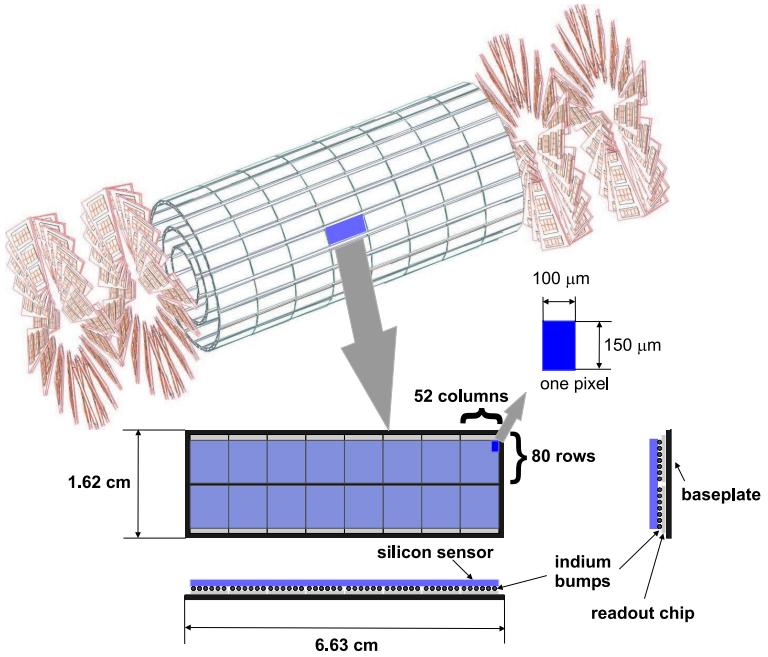

Figure 1.6. Layout of the CMS pixel detector (top) and a barrel module (bottom).

are attached to cooling pipes which also provide the main mechanical support the detector. The operating temperature of the detector is -10°C. On the top of the silicon sensors there is a High Density Interconnect (HDI) (not shown in the Fig. 1.6) that is used to connect the readout chips with the supplementary control chips and power. The HDI consists of tree layers of cooper lines of 7 μm separated by a polyimide insulator layers.

The pixel readout chip reads out signal amplitudes from the 80 row × 52 column pixel array. Each readout chip consists of 80×52 pixel unit cells (PUCs) that are individually connected to the pixels in the sensor. The PUCs are organized in 26 double–columns that are connected to a column periphery. Each pixel unit cell consists of an analog and a digital block, shown in Fig. 1.7. The analog block contains a preamplifier, a shaper, a comparator and a 3–bit DAC (digital–to–analog converter) to adjust threshold of the comparator. Both the preamplifier and the shaper are inverter circuits with integrating RC–feedback. These circuits provide a shaping time below 25 ns. Two time constants (RC) can be adjusted via a fast I^2C protocol to compensate for changes in performance caused by irradiation. The comparator threshold for each pixel is the sum of a global threshold and an individual 3–bit programmable threshold.

When a hit above threshold occurs the digital block stores the analog amplitude in a sample–and–hold capacitor. The stored amplitude and pixel address on the double column are transferred to a column periphery circuit when a readout token reaches the unit cell. The column periphery encodes the analog amplitude information of the hit pixels, its addresses in the double column and the address of the double column into a sequence of analog pulses. Thus at this stage the analog sequence contains both the location and the amplitude of the pixel. Sequences from different pixels are daisy chained together. The readout chip identification number is then attached to the daisy chained sequence to create a readout unit sequence.

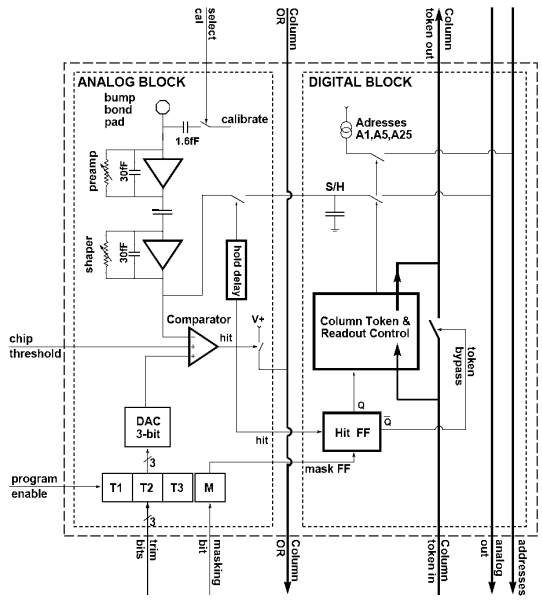

Figure 1.7. Pixel unit cell conceptual design [6].

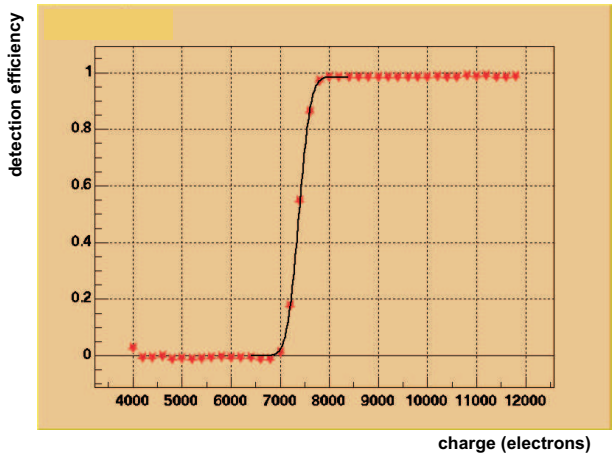

Figure 1.8. Detection efficiency for one pixel as a function of the charge injected into the preamplifier

These readout unit sequences are then consecutively passed to the digitizing electronics. Data are zero suppressed during read out since only information from pixels with amplitudes above a threshold is sent to the digitizing electronics. Noisy pixels are excluded by the setting a mask bit in the analog block, thus they are excluded before generating a sequence. The threshold for the signal in the analog block of the i–th pixel is

$$TH_i = F_i(th_i), \tag{1.7}$$

where th_i is the discriminator threshold, and F_i is the response function of the discriminator for each pixel. The threshold value in electrons is determined by scanning the detection efficiency

as a function of injected charge into the preamplifier, as shown in Fig. 1.8. The injected charge value at which the detection efficiency is 50% defines the measured signal threshold TH_i in electrons. The discriminator response function F_i varies from pixel to pixel.

Hence the same discriminator threshold value th_i for all pixel will not yield a unique signal threshold for all the pixels, which is ideal for a good zero–suppression mechanism. Therefore, the discriminator threshold is composed of the sum of common threshold th_c and a pixel–unique 3–bit adjustable threshold $thvar_i$. Fig. 1.9 illustrates the distributions where the 3–bit threshold is not utilized to minimize the variation in pixel–by–pixel thresholds. Each colored

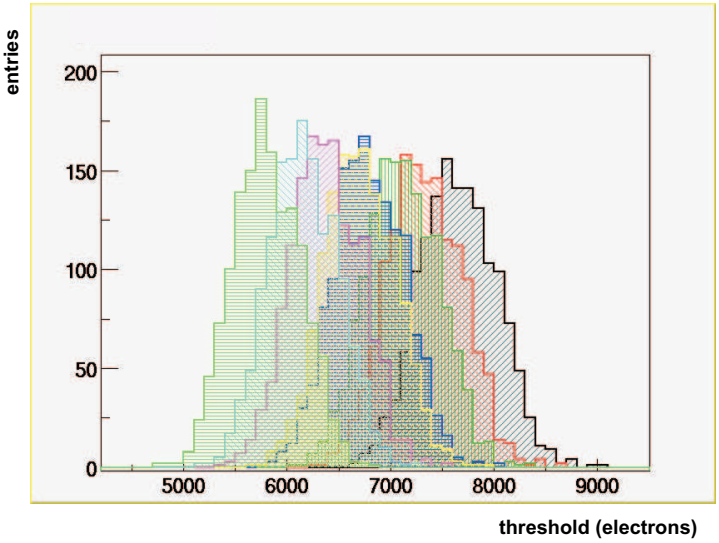

Figure 1.9. Distribution of pixel thresholds with the same 3–bit threshold setting. The eight distributions are for the eight settings of the 3–bit threshold.

histogram represents distribution of the signal thresholds TH_i, when the same discriminator threshold $thvar_i$ is set for all pixels. Different colors represent 8 different levels for $thvar_i$. The standard deviation of the signal thresholds distributions is about 1000 electrons, which is comparable to the optimum threshold of 2000 electrons. Thus, appropriately setting the individual 3–bit thresholds is important. The smallest variation of the measured thresholds is obtained by optimizing the individual $thvar_i$ for each pixel such that the distribution of thresholds TH_i has the minimal width, as shown in Fig. 1.10. In this case the standard deviation is below 100 electrons, which is smaller than the noise of the preamplifier (approximately 400).

1.4. Silicon sensor designs

Radiation hardness is the main concern in the design of the silicon sensors. It is found[7] that oxygen enriched silicon substrate is superior to non–oxygenated silicon after irradiation with charged hadrons[1]. In addition the n–on–n design technique, where the active volume is made of n–type silicon, provides better radiation tolerance then the p–on–n technique, where

[1] One of the possible explanation is that the radiation hardness increases due to the vacancy-oxygen complex formation (VO) and, hence, the donor removal process is suppressed

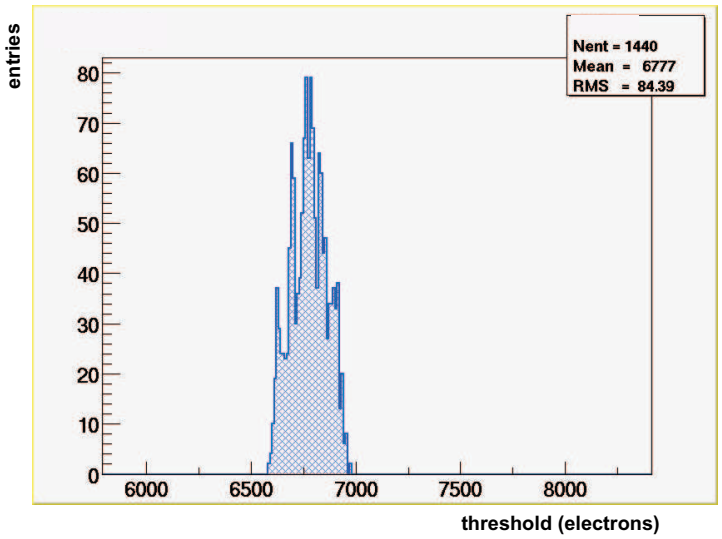

Figure 1.10. Threshold variation distribution when the optimum 3–bit threshold values are set in each pixel.

the active detector volume is made of p–type silicon. Irradiation converts n–type silicon to p–type, i.e. irradiation introduces acceptors. The concentration of acceptors increases with irradiation and the depletion depth decreases. After some time the detector becomes unusable. During the type conversion process the concentration of donors and acceptors is small and it can be fully depleted. Therefore, if the initial bulk material is n–type silicon, the lifetime of the detector increases by the type conversion time.

Different sensor designs for the CMS pixel detector [8], [9] are shown in Fig. 1.11. The layout of masks for the for p–spray design is shown in Fig. 1.12(a) and Fig. 1.12(b). The bulk material is diffusively–oxygenated float zone (DOFZ) n–type silicon of $\langle 111 \rangle$ orientation and has a resistivity 2–5 kΩ cm for the p–spray design. For the p–stop design the silicon is cut in $\langle 100 \rangle$ orientation.

The pixels are formed by p–spray isolated n^+ implants, while the pn junction is formed by a large p^+ implant on the backside. The thickness of the sensor is 285 µm and the pixel size is 100×150 µm^2. The pixels must be separated by p^+ type isolation in order to prevent conductive interconnection between them caused by electron accumulation close to the surface between pixels. The separation is only required for n–in–n design and tends to make the sensor production more expensive. Several designs of p^+ dopants separations are possible. Ring (so–called p–stop rings) structures with very high boron concentration can surround every pixel or a moderate boron spray concentration can be diffused in between pixels. The latter approach is called p–spray and has the advantage that the inter–pixel gaps can be smaller, and no additional masks have to be produced for the rings. In order to keep the pixel potential close to the readout chip potential, e.g. if a pixel looses the indium bump connection, the pixels are not completely isolated from each other. The high resistive inter–pixels connection is fulfilled by putting a gap in the p–stop rings or in case of the p–spray design special punch–through structures connect pixels to a bias grid. The advantage of having the bias grid is that the complete sensor can be tested with IV curve measurements. These tests can be performed prior to the expensive bump–bonding procedure. The potential of the segmented side of the

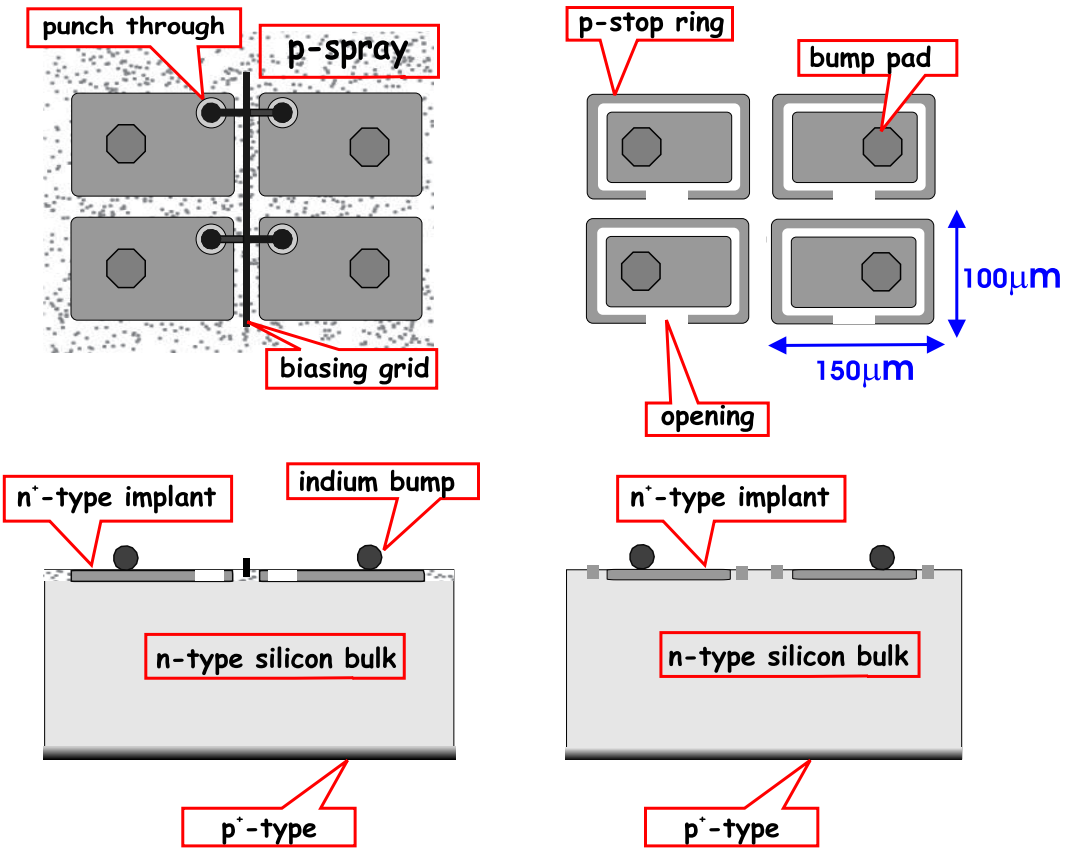

Figure 1.11. Sensor designs for the CMS barrel detector (left) and end–caps (right).

sensors has to be kept very close to the potential of the readout chip in order to prevent a discharge in air, especially when sensors are operated at a high bias voltage (600 V) to compensate for irradiation damage. On the backside of the sensors outer guard ring structures are made (Fig. 1.12(b)) to gradually drop potential between the front and back surface of the sensor.

Both sensors designs perform similarly and will be used in the CMS pixel detector. The barrel part of the detector will consists of p–spray sensors produced by CiS[2]. While the disks are made up of the p–stop type that are manufactured by Sintef[3].

1.5. Goal of the present work

The pixel detector spatial resolution of 10 μm in the direction orthogonal to the B-field can only be achieved using charge sharing between pixels. Charge sharing in silicon sensors is increased by the magnetic field, which causes charge carriers to be deflected by the Lorentz force. Therefore the charge drift and the Lorentz deflection in the magnetic field have to be carefully studied. Furthermore, the pixel detector is placed in the most radiation harsh region,

[2]Institute for Micro Sensors, Erfurt, Germany.
[3]SINTEF, Oslo, Norway.

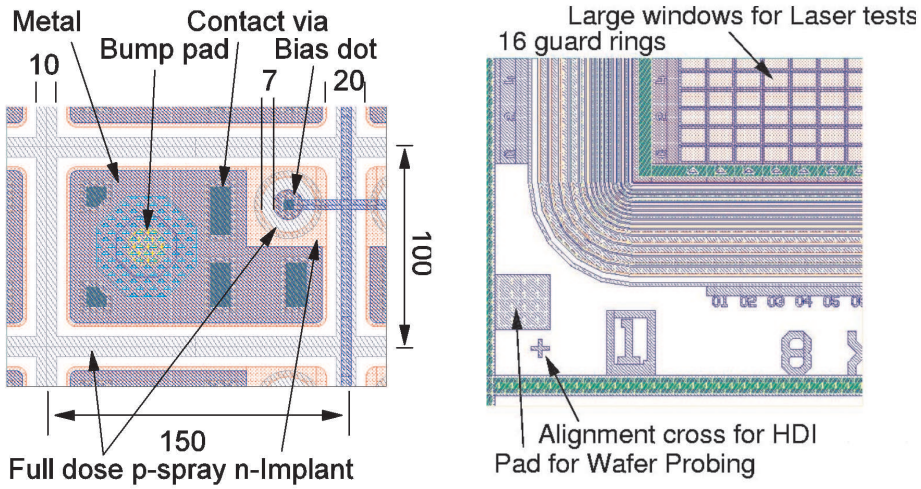

(a) (b)

Figure 1.12. The masks for the p–spray design. Left: The mask layout of the pixel side. The distances are in μm. Right: The mask layout of the backside.

close to the beam interaction point (starting from 4.4 cm). During the first four years of operation the innermost barrel layer will be exposed to hadron fluences[4] up to 6×10^{14} n_{eq}/cm^2 . Therefore, the radiation damage of the silicon sensors has to be investigated and the properties of the detector after irradiation have to be measured. Due to the high number of tracks per bunch crossing the occupancy of each single pixel is in the order of 10^{-4} and the dead time of the readout electronics should be minimized. The total number of pixels is about 66×10^6, which implies that the readout electronics must implement a zero–suppressed readout mode: the signal in each pixel has to be compared with the threshold, and only pixels with signal above it have to be read out. The threshold requirement implies that the degradation of the signal–to–noise ratio after irradiation has also to be studied. In this work the following properties of different pixel designs (p–spray, p–stop) will be studied before and after irradiation:

- the charge collection efficiency as a function of position on the pixel
- the signal-to-noise ratio
- the particle detection efficiency with and without the magnetic field
- the Lorentz angle as a function of bias voltage
- the position resolution as a function of bias voltage

[4]All particle fluences are normalized to 1 MeV neutrons (n_{eq}/cm^2).

2. Basic physical processes in semiconductor detectors

Position sensitive detectors are used for the measurement of particles tracks. Particles crossing the detector sensitive volume generate charge carriers, which form the detector signal. Irradiation modifies the lattice structure of the detector material and, hence, the properties of the detector. The basic physical processes in semiconductor detectors such as depletion, charge collection and signal formation are discussed in this chapter. In addition, the consequences of irradiation are presented.

2.1. The pn diode

The sensitive volume of a semiconductor detector is formed by the space charge region (SCR) of a pn diode. The SCR is often called *depleted region*, because it is depleted of mobile charge carriers and the resulting electric field is not zero. The pn diode is made of a low–doped silicon bulk which can be of n–type if it is doped with *donor* impurity atoms or of p–type if it is doped with *acceptor* impurity atoms. At the sides of the detector highly doped implants of n^+–type and p^+–type are created and connected to the electrodes. In order to create the SCR the pn diode has to be depleted by applying a reverse biasing voltage, i.e. applying positive voltage to the n^+–side and negative voltage to the p^+ side. The dopant atoms become ionized and they form the space charge region. The depletion voltage is determined from the solution of the Poisson equation and is given by

$$V_{dep} = \frac{eNd^2}{2\epsilon} - V_{bi}, \tag{2.1}$$

where d is the detector bulk thickness, N is the doping concentration in the silicon bulk, $V_{bi} \approx 0.5$V is the built–in voltage in silicon, usually much smaller than the applied voltage and can be neglected, ϵ is the dielectric constant, e is the electron charge. The charge density in the SCR and the electric field in the sensor bulk as a function of depth for depleted, over–depleted and not fully depleted detectors are shown in Fig. 2.1, where n–type silicon is chosen as bulk material. When the bias voltage V_b is equal to V_{dep}, the electric field increases linearly from zero to $E_{max} = eNd/\epsilon$ (Fig. 2.1). If the applied bias voltage V_b is larger than V_{dep} the detector becomes over–depleted, and the electric field linearly increases from $(V_b - V_{dep})/d$ to $(V_b + V_{dep})/d$. If the applied bias voltage is smaller than V_{dep} the electric field is zero in the depth range from 0 to $d - \sqrt{(2\epsilon V_b)/(eN)}$, then it linearly increases up to $2V_b/d$. In the case of a not fully depleted detector, the SCR depth, usually called *depletion depth*, is

$$W_d = \sqrt{\frac{2\epsilon V_b}{eN}} \tag{2.2}$$

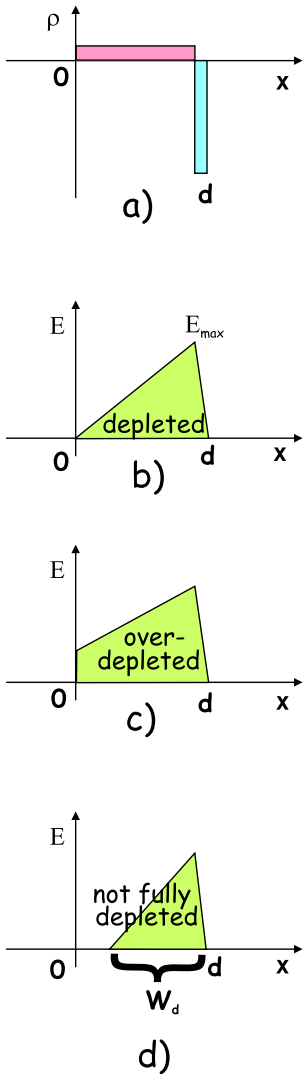

Figure 2.1. a) The charge density in the space charge region. The ionized donors are in red, the ionized acceptors are in blue. The electric field in the sensor bulk as a function of depth for depleted (b), over–depleted (c) and not fully depleted (d) detectors.

and the sensor bulk capacitance is given by

$$C_d = \frac{\epsilon}{W_d}. \tag{2.3}$$

The SCR in this case is smaller than the detector bulk thickness, and the rest of the bulk, where the electric field is zero, is called space neutral region (SNR).

The current at reverse biasing is called *leakage current* and it is usually very small, because it is produced only by thermal generation of electron–hole pairs and is in the order of 1nA/cm^2.

2.2. Generation of charge carriers

Particles traversing the detector, loose energy in the detector sensitive volume. The average energy loss per unit path length is given by the Bethe–Bloch formula [4]

$$-\frac{dE}{dx}[\mathrm{MeVg^{-1}cm^2}] = Kz^2\frac{Z}{A}\frac{1}{\beta^2}\left[\frac{1}{2}\ln\frac{2m_ec^2\beta^2\gamma^2T_{max}}{I^2} - \beta^2 - \frac{\delta}{2}\right], \tag{2.4}$$

where $K = 4\pi N_A {r_e}^2 m_e c^2 = 0.307\ \mathrm{MeVg^{-1}cm^2}$, I is the mean excitation energy, δ is the density effect correction, T_{max} is the maximum kinetic energy which can be imparted to a free electron in a single collision. The energy loss only depends on the incoming particle's velocity (β), and not directly on its mass. The energy loss therefore shows four regions: a rapid decrease proportional to $1/\beta^2$ at lower velocities, a minimum at $E \approx 3Mc^2$ i.e. $\gamma \approx 3$, a slow logarithmic "relativistic rise", proportional to $\ln(\gamma)$ and a plateau as ionization is limited by the density effect. The changes in energy loss for E above the minimum are smaller than those in the low velocity region. For this reason, any particle with $\gamma > 3$ is often called a *minimum ionizing particle* (mip). The energy loss of a minimum ionizing particle is about 82 keV in 290 µm of silicon [10]. The fluctuation of the energy loss can be approximated by the Landau distribution [11]

$$f_L(\epsilon, x) = \frac{\phi(\lambda)}{\zeta}, \tag{2.5}$$

where ϵ is the lost energy, x is the material thickness. ζ (in MeV) is

$$\zeta = 0.1535\frac{z^2 Z\rho x}{\beta^2 A}, \tag{2.6}$$

where z and βc are the charge and the velocity of the incoming particle, Z, A and ρ are the atomic number, atomic weight and density of the material respectively. The function $\phi(\lambda)$ has been tabulated in [12]. The dimensionless variable λ is given by

$$\lambda = \frac{1}{\zeta}[\epsilon - (\epsilon_{mp} - \zeta\lambda_0)], \tag{2.7}$$

where λ_0 is the value for which ϕ has a maximum, ϵ_{mp} is the most probable energy loss. This energy is expended to create electron–hole (e–h) pairs. In silicon about 3.62 eV at 300 K [13] are needed to create one e–h pair. Therefore, in 285 µm thick silicon bulk the total number of e–h pairs created by a mip is about 22400.

2.3. Kinematics of the charge carriers

In the presence of the electric field free charge carriers (electrons and holes) in the SCR region drift toward the electrodes due to the electrostatic force. The drift velocity of electrons, v_e, and holes, v_h, depend on the electric field strength E

$$v_e = \mu_e E, \quad v_h = \mu_h E, \tag{2.8}$$

where μ_e is the electron mobility and μ_h is the hole mobility. The mobility dependence on the electric field E and temperature T in low doped silicon are given by the empirical formulas [14]

$$\mu_e = \frac{\mu_{e0}}{[1 + \mu_{e0}E/v_{esat})^{\beta_e}]^{1/\beta_e}}, \tag{2.9}$$

$$\mu_h = \frac{\mu_{h0}}{[1 + \mu_{h0}E/v_{esat})^{\beta_h}]^{1/\beta_h}}, \tag{2.10}$$

where

$$\begin{array}{ll} \beta_e = 1.395, & \beta_h = 1.215, \\ v_{esat} = 8.64 \times 10^6 - 2.68 \times 10^3\, T, & v_{hsat} = 10.65 \times 10^6 - 2.68 \times 10^3\, T, \\ \mu_{e0} = 88.0\left(\frac{T}{300}\right)^{-0.57} + 1252.0\left(\frac{T}{300}\right)^{-2.33}, & \mu_{h0} = 4.3\left(\frac{T}{300}\right)^{-0.57} + 407.0\left(\frac{T}{300}\right)^{-2.33}. \end{array}$$

In these empirical formulas the temperature T is expressed in Kelvins, the mobility is in $\frac{\mathrm{cm}^2}{\mathrm{Vs}}$, the velocity is in cm/s. and the electric field is in V/cm. The v_{esat} and v_{hsat} are the saturation velocities for electrons and holes, respectively. Charge carriers are subject to diffusion and the diffusion coefficient for electrons D_e and for holes D_h is given by the Einstein relationships

$$D_e = \frac{kT}{q}\mu_e, \tag{2.11}$$

$$D_h = \frac{kT}{q}\mu_h, \tag{2.12}$$

where k is the Boltzmann constant, T is the temperature and q is the carrier charge. The standard deviation of of charge carriers density is given by

$$\sigma_e = \sqrt{2D_e t_e}, \tag{2.13}$$

$$\sigma_h = \sqrt{2D_h t_h}, \tag{2.14}$$

where t_e and t_h are the drift times for electrons an holes, respectively.

In the presence of a magnetic field $\vec{B}$, the charge carriers q are subject to the Lorentz force, and the resulting force $\vec{F}$ is given by

$$\vec{F} = q(\vec{E} + \vec{v} \times \vec{B},) \tag{2.15}$$

where $\vec{v}$ is the velocity of the charge carriers. The combination of the force and the scattering in the silicon lattice results in a deflection along an angle Θ_L, which is called the Lorentz angle. If the magnetic field is perpendicular to the electric field the Lorentz angle is

$$\Theta_L = \mu_H |\vec{B}|, \tag{2.16}$$

where $\mu_H = r_H \mu$ [1].

The charge carriers drift toward the electrodes under the influence of the electric field. A charge sensitive preamplifier connected to the electrodes, amplifies and integrates the current induced at the electrodes. This current is given by the Ramo–Shockley [15, 16] theorem,

$$I = q\vec{v} \cdot \vec{E}, \tag{2.17}$$

where q is the moving charge, $\vec{v}$ is its velocity and $\vec{E}$ is the effective field. This effective field is obtained by solving the Poisson equation under the boundary condition given by the potentials on the electrodes. All electrodes are set to zero potential, except the electrode where the induced current has to be calculated. The potential at this electrode is set to 1 V. The signal is obtained by integrating the current, Eq. 2.17.

[1] $r_H = 1.15$ for electrons and $r_H = 0.7$ for holes.

2.4. Position reconstruction

The volume of the semiconductor is partitioned into sub–volumes in order to measure the impact position of the incoming particle. The segmentation is usually done by splitting one (or both) of the collection electrode(s) into strips or pixels. The strip spacing or the size of the pixels is called the pitch. The single pixel resolution is given by the standard deviation of a flat distribution, the pitch divided by $\sqrt{12}$. However a better resolution is obtained when charge is shared between a few sub–volumes. The charge sharing can be accomplished in several ways:

- orientating the detector in such a way that most particle track are inclined with respect to the detector surface,
- with the Lorentz force in a magnetic field (the method is used for the CMS pixel barrel),
- by creating a non–uniform drift field,
- or by optimizing diffusion in the active volume.

With charge sharing position is determined by a weighted sum of the signal amplitudes from the sub–volumes or with other position finding algorithms [17]. Typically the error in the position, the position resolution, is affected by the fluctuation of the energy loss and by the noise of the preamplifier.

2.5. Semiconductor detectors after irradiation

Irradiation of silicon detectors with high energy particles causes displacement of primary knock–on atoms (PKA) out of the silicon lattice site. An interstitial atom and a left–over vacancy (Frenkel pair) are created in the silicon lattice. If the energy transferred to the PKA is high enough, it can displace other lattice atoms from their regular sites before stopping. These "secondary atoms" may further displace other atoms. This process results in a displacement cascade.

These defects can be *point–like* in case of gamma irradiation or in *clusters* for high energetic hadrons or leptons. The temperature increases lattice defects mobility. Defects can merge or dissociate into components. This process is called *annealing*. The defects of the lattice can act as donors and acceptors that alter the macroscopic properties of the silicon sensor, such as the depletion voltage and leakage current. The defects can also trap and release charge carriers. The effective dopant concentration is given by the difference between the ionized donors and acceptors in the SCR. Therefore, the dopant concentration N in Eq. 2.1 has to be replaced with the absolute value of the effective concentration of charge carriers [18], i.e. effective dopant concentration N_{eff}

The change in the leakage current after irradiation is given by [18]

$$\Delta I = \alpha \Phi V, \tag{2.18}$$

where Φ is the particle fluence[2], V is the detector volume and α is the current related damage rate. The rate was found to be equal to $\alpha = 3.99 \pm 10^{-17}$A/cm [18] for 1 MeV neutrons irradiation and detectors annealed at 60°C for 80 minutes. The current related damage rate

[2]The fluence is the time integrated particles flux.

can be used to compare the damage produced by fluences from different types of particles and at different energies. Other particles fluences are typically expressed in terms of the current related damage rate produced by a flux of 1 MeV neutrons, 1 MeV n_{eq}/cm^2 .

The amount of drifting charge decreases as charge carriers are trapped. The induced signal is calculated by substituting the charge value q in the Ramo–Shockley theorem (Eq. 2.17) with a time dependent charge value. The time dependence is given by

$$q_e(t) = q_e(t=0)e^{-t/\tau_e} \quad \text{and} \quad q_h(t) = q_h(t=0)e^{-t/\tau_h}, \tag{2.19}$$

respectively for electrons and holes. Where τ is the trapping time constant and is given by

$$\frac{1}{\tau_e} = \beta_e \Phi_{eq} \quad \text{and} \quad \frac{1}{\tau_h} = \beta_h \Phi_{eq}. \tag{2.20}$$

Where Φ_{eq} is the particles fluence, and β is the parameter for protons given by

$$\beta_e = 5.6 \pm 0.2 \times 10^{-16}\,\mathrm{cm}^2/\mathrm{ns} \quad \text{and} \quad \beta_h = 7.2 \pm 0.2 \times 10^{-16}\,\mathrm{cm}^2/\mathrm{ns}\ [19]. \tag{2.21}$$

The signal in the semiconductor detector decreases after the irradiation because of the trapping of charge carriers. The signal also decreases due to an incomplete charge collection, i.e. a decrease of the depletion depth, while noise increases because of an increase in the leakage current and an increase of the detector capacitance.

The leakage current, formed by the thermal generation of the electrons and holes, increases dramatically after heavy irradiation. Thermally generated electrons and holes are trapped during their drift. This additional charge density must be added to the charge density of ionized donors and acceptors. Hence the additional charge density and effective dopant concentration is not constant as a function of depth. The leakage current is given by

$$j = Gd, \tag{2.22}$$

assuming that the thermal current is generated at a constant rate G throughout the detector thickness d (also shown in Fig. 2.2). Thus the continuity equations are

$$\begin{aligned} \nabla \cdot j_e &= G, \quad j_e(d) = 0; \\ \nabla \cdot j_h &= G, \quad j_h(0) = 0. \end{aligned} \tag{2.23}$$

Solving these continuity equations, the electron and hole currents are

$$\begin{aligned} j_e &= G(d-x) \\ j_h &= Gx. \end{aligned} \tag{2.24}$$

Furthermore, if the trapped charge is proportional to the current then the charge densities are

$$\begin{aligned} \rho_e &\propto G(d-x) \\ \rho_h &\propto Gx. \end{aligned} \tag{2.25}$$

The contribution to the total N_{eff} concentration from the trapped charge carriers can be larger then the concentration of the dopants. Thus, N_{eff} can change sign within the depth, which results in a non–uniform electric field, the so–called "double junction" or "double peak" [20] electric field profile, shown in Fig. 2.2. The electric filed is different in an unirradiated detector where the field strength grows linearly, as shown in Fig. 2.1. The behavior of the electric field (double junction) is very different from the one expected for non irradiated detector, Fig. 2.1.

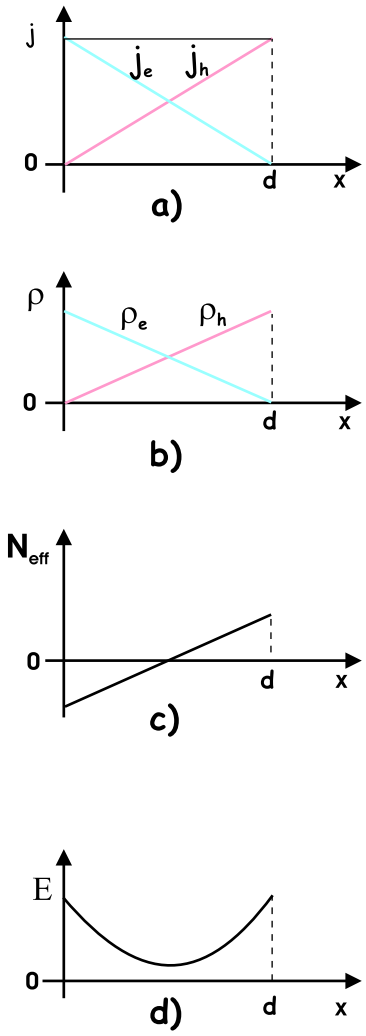

Figure 2.2. The "double–junction" model in the irradiated detector. a) The leakage current density for electrons j_e and holes j_h. b) The trapped charge density for electrons ρ_e and holes ρ_h. c) The effective dopant concentration N_{eff}. d) The electric field E for the irradiated detector as a function of the depth.

3. Experimental setup and data reconstruction algorithm for the silicon sensors study

3.1. The experimental setup

The tested sensors are different from the sensors that will be used in the CMS pixel detector. However the only difference is in the pixel implants geometry: the pixel size is 125×125 μm^2 (instead of 100×150 μm^2). The sensor has 22 columns an 32 rows of pixels.

The experimental setup for the measurements of the sensor properties (Fig. 3.1) includes a pixel sensor bump–bonded to a readout chip, the pixel readout electronics, a cooling system, a trigger system, a silicon microstrip telescope and a data acquisition systems (DAQ). The

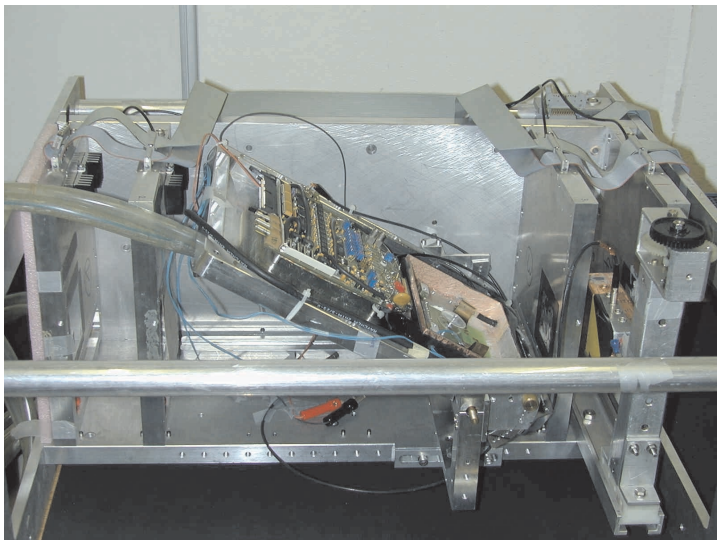

Figure 3.1. Test setup.

whole setup was placed in a open 3 T Helmholtz magnet (Fig. 3.2) with magnetic field parallel or perpendicular to the beam. The measurements were performed at the H2 beam line of the CERN SPS using 150–225 GeV pions. The test have to be done with large energy beams to minimize multiple scattering. The particles were structured in 5 s spills arriving in 15 s intervals.

The mechanical construction of the setup is shown in Fig. 3.3. A silicon beam telescope [21], [22] was used to allow a precise determination of the particle hit position in the pixel detector. The beam telescope consists of 4 modules. Each module consists of two 300 μm thick

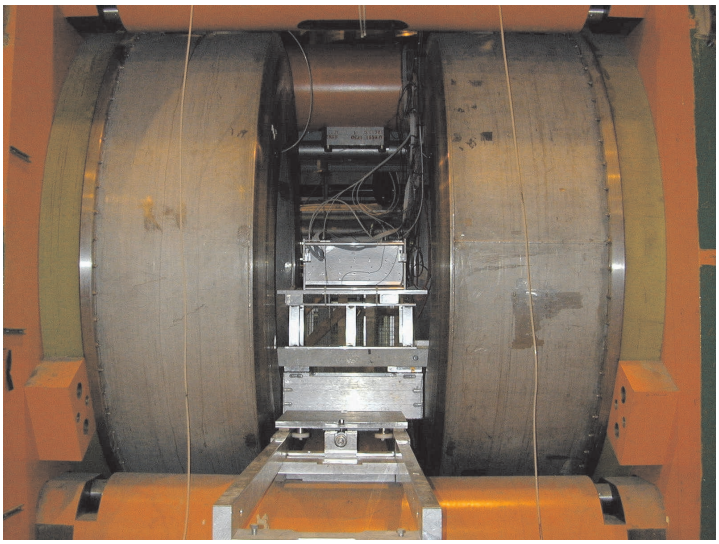

Figure 3.2. Test setup placed in a open 3 T Helmholtz magnet.

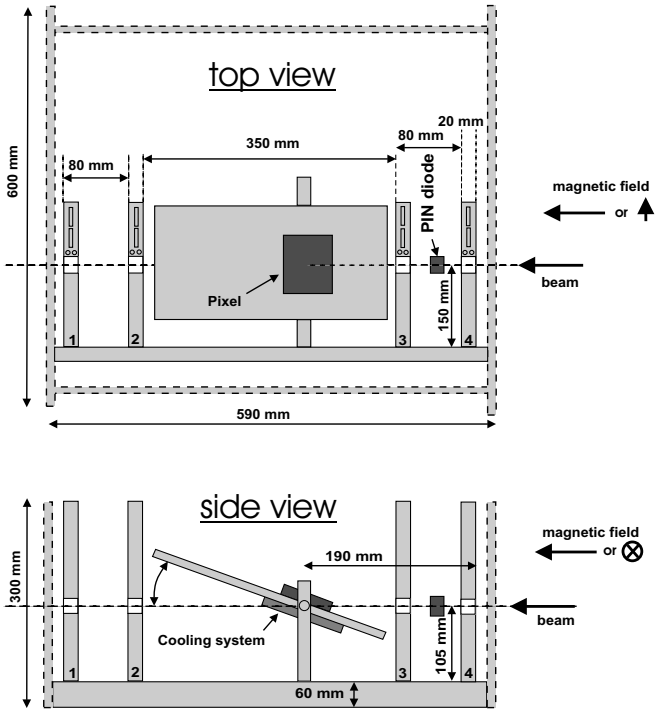

Figure 3.3. Top and side views of the setup.

single–sided silicon strip detectors with a sensitive area of 32×30 mm^2. The strip pitch is 25 µm and the readout pitch is 50 µm. In each module the two sensor planes are oriented perpendicularly. The integration time of the amplifier is about 2 µs. The signals from the silicon strips are read out by two CAEN V550 CRAMs and controlled by the CAEN V551

sequencer module. The intrinsic position resolution of the beam telescope is about 1 µm [21]. Four beam telescope modules are mounted vertically on a support frame. The pixel sensor is bump–bonded to the readout chip which is connected to the pixel readout card via a short flat cable. The pixels sensors are tested at a temperature of -10°C [1]. The pixels sensor and the readout chip are enclosed in a thermo–isolated plastic box and flushed with dry nitrogen to avoid water condensation. The readout chip is coupled to two Peltier elements which are used to set the temperature of the sensor. The temperature is measured with a PT1000 platinum resistor and stabilized by regulating the voltage applied to the Peltier elements. The hot side of Peltier elements is cooled with the circulating water. The coolant temperature is regulated by means of a circulation chiller.

The pixel readout card and the plastic box are mounted on a frame, which can be rotated along the horizontal axis with a precision of 0.2° . The pixel support frame is placed between the second and third beam telescope module. A trigger signal is generated by a silicon PIN diode which is placed between the third and fourth telescope plane. The position of the diode can be adjusted with about 100 µm precision.

The schematic view of the readout is shown in Fig. 3.4. The data acquisition system is

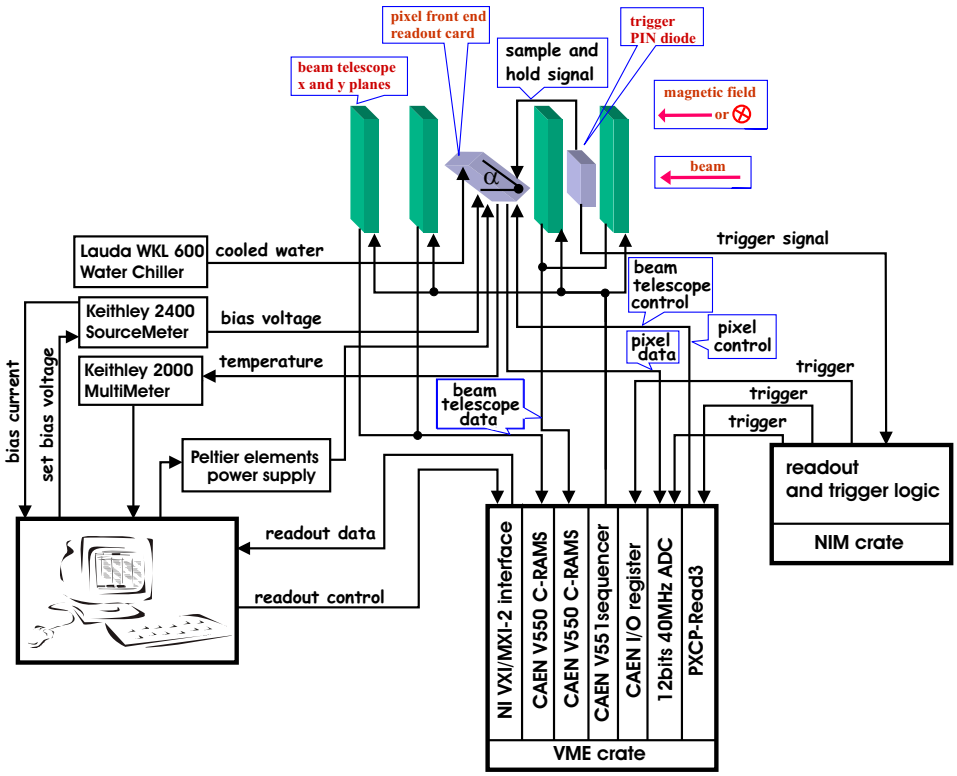

Figure 3.4. Schematic diagram of the readout system.

written in LabView and LabWindows CVI[2] and runs on a PC. The analog signals are digitized in a VME based readout system by two CAEN V550 and one custom built ADCs [23]. The

[1] To prevent annealing and decrease leakage current the operation temperature of the CMS pixel detector is set -10°C .

[2] LabView and LabWindows are products of National Instruments.

digital control for the beam telescope and pixel readout is provided by a CAEN V551 sequencer and PXCP Read3 modules [23]. The PIN diode provides a sample and hold signal to latch the analog amplitudes in the pixel readout chip (Section 3.1.1). In addition, the trigger signal is used to starts the readout of the beam telescope. The data acquisition includes a slow control part which sets the bias voltage of the pixel sensor, monitors its current and stabilizes the its temperature with 0.1°C precision. The data reconstruction includes: the correction for common–mode noise, the track reconstruction with the beam telescope and pixel, and alignment of pixel plane with the beam telescope planes. The events selection is done using a simple straight line topology. The calibration of the pixel signals is performed and the signals in pixel and the incident particle position are available for further analysis.

3.1.1. Pixel readout

The analog signals of all the 22×32 pixels are read out by the `PSI30/AC30` readout chip [24]. In the chip each pixel cell includes a preamplifier and a shaper with a shaping time of about 30 ns, which can be set via the DAQ.

The readout occurs when the particle crosses the PIN diode area. The trigger pulse is sent to the sample–and–hold (S/H) input of the readout chip. The active level of the S/H pulse disconnects a capacitance attached to the shaper output. The signal amplitude is therefore stored in the capacitance (Fig.1.7). At the same time, the trigger pulse is sent to the FADC via the PXCP Read3 module and all stored amplitudes are read out. The analog amplitudes are then digitized by the 12 bits 40 MHz analog–to–digital converter [23]. The particles are structured in 5 seconds spills in 15 seconds intervals. The PXCP–Read3 module does not send clock pulses during the time between spills. Thus, the common mode noise increases during the spill. To decrease this noise, the PXCP–Read3 module was modified and the clock pulses were sent continuously. After the modification the common mode noise fluctuation is below 10%.

After digitization the pixel signals are stored in a data file. The pedestals values of each pixel cell are measured between spills and stored in the same file.

A calibration of the analog readout chain can also be performed with the DAQ system. The calibration pulse is sent to the input of each preamplifier via a 1.7 pF capacitance. The sampling position of the S/H and the linearity at this position can be measured with test pulses. The waveform was obtained by scanning the output as a function of delay time between a calibration pulse and the trigger pulse sent to the S/H, as shown in Fig. 3.5. The charge of the calibration pulse is known and injected through the 1.7 pF capacitance into the `PSI30/AC30` readout chip. The most probable ADC value in the test beam data, 710 ADC counts, corresponds to a S/H position of 55 ns on the 1 mip waveform. This position is within 90% of the waveform maximum and within the region of good signal to noise.

At the sampled position, 55 ns, the output signal is proportional to the input charge, as shown in Fig. 3.6. However, above calibration pulses of 1.5 mip the output signal saturates.

3.1.2. Data acquisition system

The data acquisition system (DAQ) controls the VME crate via a VXI/MXI bus, the Keithley 2000 multimeter, the Keithley 2400 Sourcemeter and the National Instruments PCI–6704 static analog output card (Fig. 3.4). The Keithley 2400 Sourcemeter is used for biasing the pixel sensor and the Keithley 2000 multimeter is used to measure the resistance of the PT1000

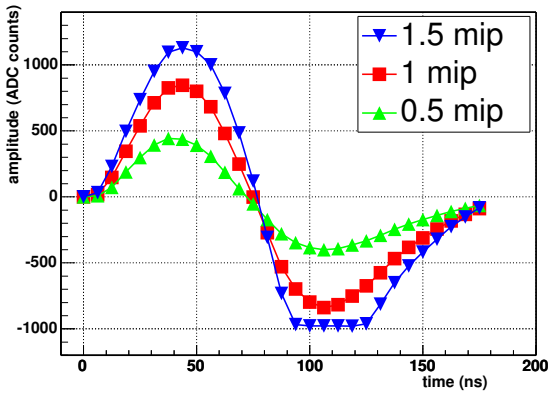

Figure 3.5. Waveform at the shaper output of the PSI30/AC30 readout chip for different calibration charge values.

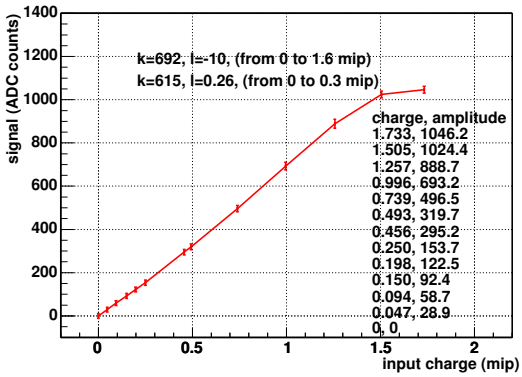

Figure 3.6. Calibration of signal in the pixel cells. Amplitude as a function of the input charge.

temperature sensor. The National Instruments PCI–6704 is used to set the voltage for the Peltier elements. The pixel settings and the acquisition modes, e.g. data taking, pedestals and calibration are controlled from the main DAQ program (Fig. 3.7). In addition, data at several bias voltages can be taken automatically. The part of the code for which the execution time is critical is written in C. The DAQ program includes an online display of the pixel and strip amplitudes. The signals recorded in the pixel cells and in the strips are histogramed for data quality control. The telescope and pixel pedestals as well as the signal amplitudes are stored in the data file. In addition each event is marked with a time stamp. The bias voltage and current and the pixel sensor temperature are also stored.

The size of the PIN diode is larger than the pixel array size. In particular, the pixel frame may be tilted at 15 degrees with respect to the beam and some tracks might not cross the pixel area. The spatial correlation between the hits in the beam telescope and in the pixel matrix is used to discard events where the particle track does not cross the pixel area.

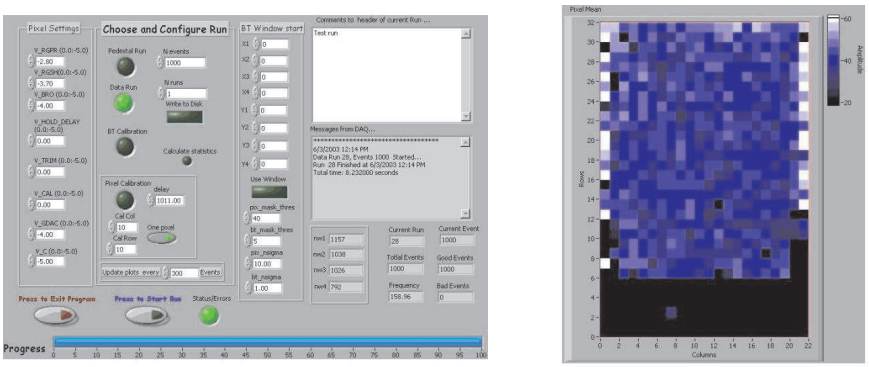

Figure 3.7. Screen shots of the main DAQ window (left) and the pixel event display (right), showing the signal amplitudes recorded in each pixel cell.

3.1.3. Trigger electronics

A PIN diode coupled to a low–noise fast amplifier is used to start the beam telescope and pixel readout. The response of the trigger system has to be faster than 30 ns, as required by the

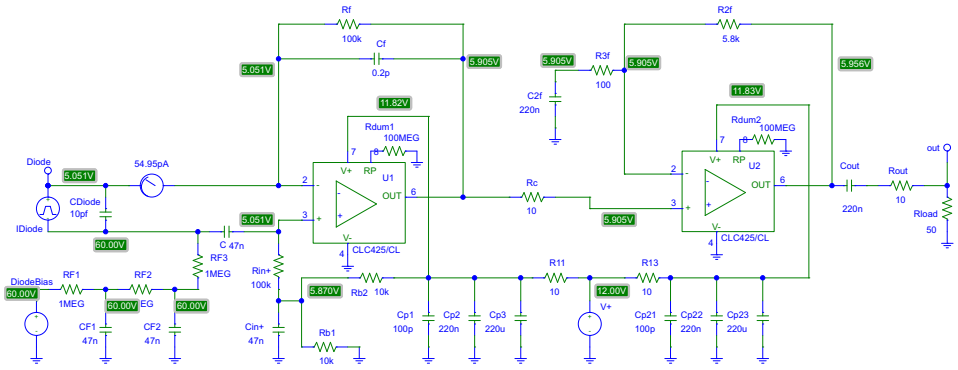

Figure 3.8. Schematics of the low–noise fast preamplifier for the trigger.

pixel readout. The amount of triggers caused by the preamplifier noise has to be reduced in order to maximize the purity of the recorded data sample. The preamplifier includes a CLC425 low noise operational amplifiers and the signal–to–noise ratio is increased by improving the coupling of the PIN diode to the operational amplifier. Both terminals of the PIN diode are coupled to the inputs of the differential preamplifier. This schematics improves the signal–to–noise ratio by a factor $\sqrt{2}$ respect to the conventional differential amplifier configuration, where one of the inputs is connected to ground. A fast comparator with variable amplitude threshold and a monostable circuit are used to provide TTL and NIM pulses needed by the readout electronics. A simulation with PSpice was performed to estimate the pulse shape and the noise of the preamplifier. The simulated output noise voltage integrated over a frequency range as a function of the integration limit is shown in Fig. 3.9. The simulated pulse shape at the output of the preamplifier is shown in Fig. 3.10 The pulse height measured with particles at the output of the preamplifier is shown in the top part of Fig. 3.11. The trigger pulse at

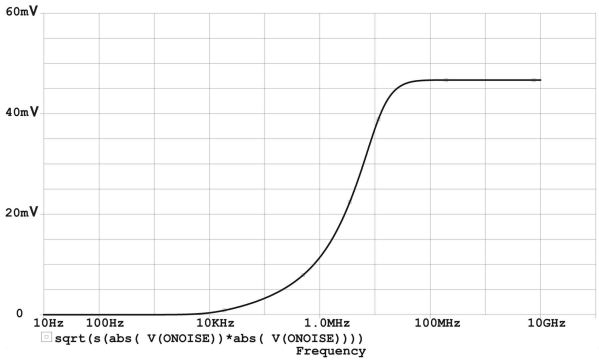

Figure 3.9. Output noise integrated over frequency range as a function of the frequency range.

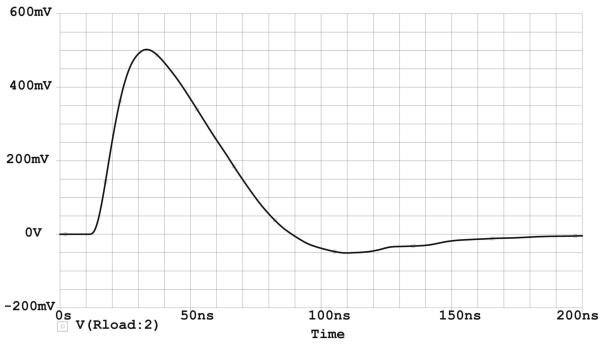

Figure 3.10. Pulse height at the output of the preamplifier for an input signal of 10k electrons.

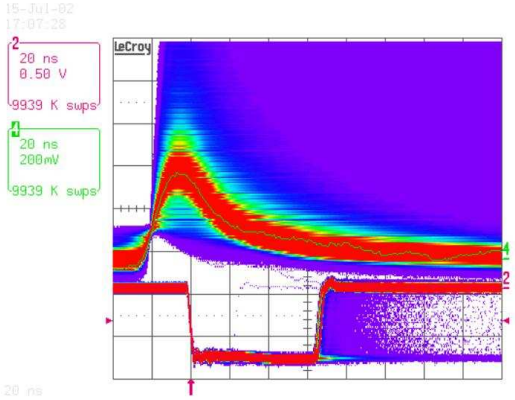

Figure 3.11. Signals from pions measured at the output of the PIN diode preamplifier (top) and at the output of the discriminator (bottom).

the output of the discriminator is shown in the bottom plot in Fig. 3.11. The signal peak corresponds to the most probable energy loss in the silicon PIN diode and has an amplitude of about 450 mV. The discriminator threshold was set to ∼130 mV. With this threshold the

trigger efficiency is higher than 95%, while the random trigger frequency due to the preamplifier noise is lower than 0.1 Hz.

3.1.4. Cooling system and temperature regulation

The cooling system consists of two high performance Peltier elements attached to a water cooled heat sink. The coolant liquid is circulated by a chiller. The sensor temperature can be stabilized down to -35°C . Heat conducting paste is used to improve the thermal contact between the cold aluminum plates and the small printed circuit board (PCB) containing the pixel readout chip. The power consumption of the pixel readout chip and the readout card is more than 20 W. This heat has to be removed by the cooling system. The heat transfer power of each Peltier element is 172 W when the difference between the cold and the hot sides is zero degrees. The power is halved if the temperature difference is 30°C .

The most efficient way to dissipate heat from the hot side of the Peltier element is to flow the coolant liquid with direct contact to the element's ceramic surface. In Fig. 3.12 the drawing of the aluminum cavity flushed with the coolant is shown. The Peltier element (not shown in the figure) is glued onto the cavity. With this design it is possible to reach the temperature

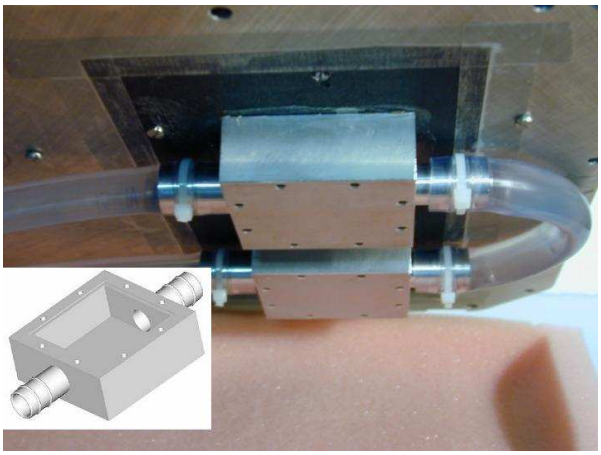

Figure 3.12. Photograph and CAD drawing of the heat sinks containing the Peltier elements (not shown).

required [3] for the sensor tests (-10°C) and efficiently remove the heat produced by the pixel front end electronics.

The sensor is attached to the readout chip which is glued onto a PCB. The temperature sensor was placed on the same PCB. Since the readout chip radiates heat the sensor temperature is higher than the PCB temperature. Therefore, the regulated temperature has to be below -10°C . In order to determine the regulated temperature, the dependence of the sensor leakage current on its temperature was used. The power of the readout chip and the readout card was switched off to remove all heat sources in the isolated box. In these conditions the temperature of the sensor and the temperature of the PCB equalized after some time. The temperature was then set to -10°C and the leakage current at a bias voltage of 150 V was measured. When the power was switched on, the temperature and the leakage current of the

[3] This temperature will be the pixel operation temperature in the CMS experiment.

sensor increased. The regulated temperature was then adjusted to the value reproducing the leakage current value measured without front end power. The temperature at the PCB was found to be about 5°C lower than the pixel sensor temperature.

3.2. Data reconstruction

3.2.1. Signal reconstruction

Pixel cell amplitudes are reconstructed with the following procedure:

1. Pixel pedestals that are stored in the data file are subtracted from the amplitudes cell–by–cell
2. The amplitudes of six unconnected pixel rows are averaged and subtracted to reduce common mode fluctuation.
3. Hit pixels above threshold, depending on the irradiation fluence, are further analyzed. The threshold was optimized for each sample and ranges between 35 – 50 ADC counts, or 1000 – 1500 electrons.
4. The pixels are checked for the expected hit frequency. If the hit frequency is below 0.1 or above 10.0 of the expected one, then the pixel is marked as bad and excluded from the amplitude reconstruction.
5. Improved pedestals and the common mode values, based on the good pixels with the amplitudes below the threshold, are calculated and subtracted from the pixel amplitudes.
6. Steps 3, 4 and 5 are repeated until the mean value of noise amplitude distribution is less than 0.1% of standard deviation or until a satisfactory number of iterations (4) have occurred.

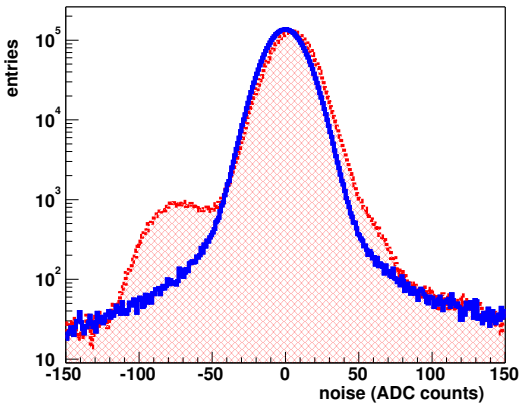

Figure 3.13. Pixel noise amplitude distributions before (red histogram) and after corrections (blue histogram). The corrections are described in the 5th step.

Even though the recorded pedestals used before step 2 differ from the values during data taking, signal amplitudes are distinguishable from noise. One advantage after step 2 is that the improved pedestal and common mode corrections are based on the good data from step 4. A comparison of the original and improved noise distributions is shown in Fig. 3.13. This reconstruction is performed in order to get precise amplitudes for the study of the noise and the signal in the silicon sensors.

The signal amplitudes from the telescope strips are reconstructed and corrected in the same way as for the pixels.

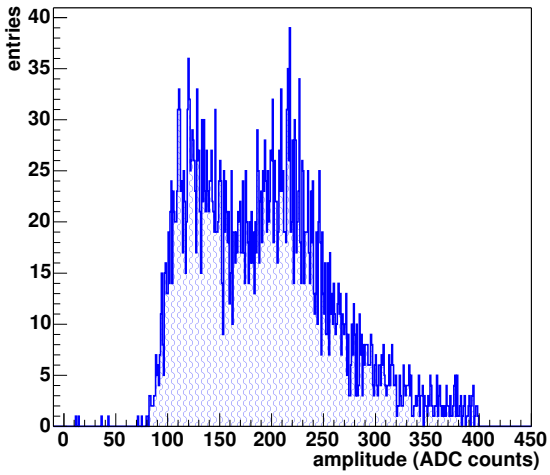

Figure 3.14. Analog signal from the beam telescope plane. The double peak is due to the floating strips.

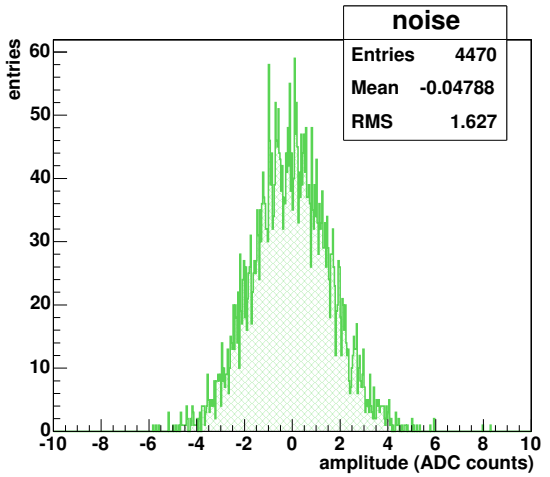

Figure 3.15. Noise of beam telescope plane after pedestal subtraction.

Only every second strip in the telescopes is readout, while the is inner strip is capacitively coupled to them. Therefore there are two peaks in the distribution of the maximum amplitudes, as shown in Fig. 3.14. When a track crosses in the close vicinity of a readout strip almost all of the charge is collected by that strip. On the other hand when a track crosses in the close vicinity of a non–readout strip, the charge is more evenly shared between the two neighboring readout strips. This latter case results in about half the signal on the strip with maximum amplitude, and produces the second peak in Fig. 3.14. The distribution of noise of the beam telescope preamplifier's is shown in Fig. 3.15. The signal–to–noise ratio is higher than 100 for the beam telescope planes.

3.2.2. Events selection using the beam telescope and events topology

Events used in the measurements described in Chapter 4 are selected with the procedure described here. The selection procedure discards the events with multiple tracks and tracks which do not fit to a straight line. The angular distribution of the particles tracks is very narrow and well below 10^{-6} radiance. Therefore, there is a strong correlation between the

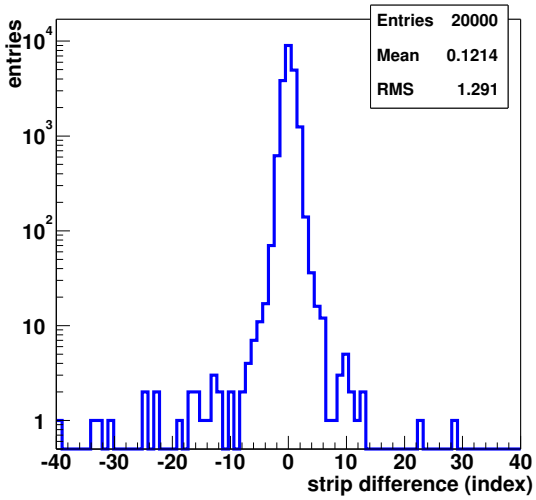

Figure 3.16. Difference distribution between indexes of the hit strips in two planes of the beam telescope. The angular distribution of the particles tracks is below 10^{-6} radian. Therefore, there is a strong correlation between the indexes of the hit strips in all beam telescope planes and, hence, the peak is clearly seen.

indexes of the hit strips in all beam telescope planes. This correlation is used to select the events with a single straight track. The event selection involves the following steps.

1. Find up to four isolated strips in the beam telescope planes with amplitudes from 30 to 350 ADC counts. The strips in each plane must be separated by at least five strips below 30 ADC counts. Their indexes are used in the following steps.

2. Build all unique pair combinations of the indexes found in step 1. Each index in a pair belongs to a different plane. The procedure is done separately for the x and y planes.

3. Histogram the index differences in the pair found in step 2 and determine the most probable value of this difference.

4. Repeat step 1 with a looser amplitude range, from 10 to 400 ADC counts.

5. Repeat step 2 for the indexes found in step 4.

6. Discard the pairs found in step 4 with index differences deviating by more than one strip from the most probable value found in step 3.

7. The events are selected if each plane has only one strip with a index not rejected in the step 6.

The procedure described above rejects approximately 50% of all events. On the other hand, the selected events consist of clean single straight tracks.

3.2.3. Reconstruction of the particle impact position using the pixel data

The determination of the particle impact position in the pixel coordinates system depends on the particle incident angle α with respect to the pixel plane, as shown in Fig. 3.17. If

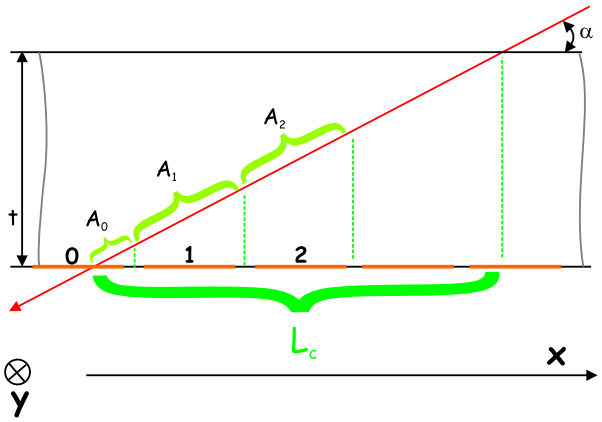

Figure 3.17. Position determination in the pixel coordinates system. For a shallow angle α only the three first rows are used for the position reconstruction.

the angle α is in the range from $60°$ to $120°$, a central pixel is found by locating the pixel with the highest amplitude above threshold. The crossing position along both coordinates is reconstructed using a center of gravity algorithm. The algorithm uses the central pixel and the surrounding eight. If the angle α is below $60°$, the length of the track projection along the x axis is larger than three pixels. In this case the three columns starting from the track exit point are used (e.g. the "0","1","2" pixels in Fig. 3.17). The pixel through which the particle exits is defined as the first pixel above threshold along the x axis and with the highest signal along the y direction. The central row of the cluster includes the two following pixels along the x axis, which are also required to be above the threshold. In addition the corresponding upper and lower rows are also included, The resulting cluster size is of 3 by 3 pixels. The y coordinate of this cluster is calculated with the center of gravity of the signal collected in three rows. The x coordinate of the exit point is calculated using the signal distribution between the three

columns in the cluster. The signal collected in the three columns defined as A_0, A_1 and A_2 and the charge sums defined as $Q_0 = A_0$, $Q_1 = A_0 + A_1$ and $Q_3 = A_1 + A_2 + A_3$. The x position is found by fitting with a line the charge sums Q_i as function of the x coordinates corresponding to A_i. The intercept of the linear fit with the abscissa defines the impact position along x.

The reconstructed position described in this section is used only to align the pixel detector with the beam telescope. At this stage no correction is applied to the reconstructed particle impact position.

3.2.4. Reconstruction of the particle impact position in the beam telescope planes

In each beam telescope plane the position of the impact point is reconstructed using a center of gravity algorithm of the cluster of two consecutive strips. Only events selected in the previous section are used. The first strip is the one found in step 5 of the previous section. The second strip is given by the neighbor with the highest amplitude. The position is corrected using the η algorithm described in [17]. The asymmetry in amplitudes of adjacent strips, η, is given by

$$\eta = \frac{A_r}{A_l + A_r}, \tag{3.1}$$

where A_r is signal of the right strip, A_l is signal of the left strip. The position of the cluster with respect to the left strip is given by

$$X_{\eta_0} = \frac{\int_0^{\eta_0} \frac{dN}{d\eta} d\eta}{\int_0^1 \frac{dN}{d\eta} d\eta}, \tag{3.2}$$

where $dN/d\eta$ is the differential η distribution. An example of the position of the cluster with respect to the left strip as a function of η is shown in Fig. 3.18. In order to estimate the spatial

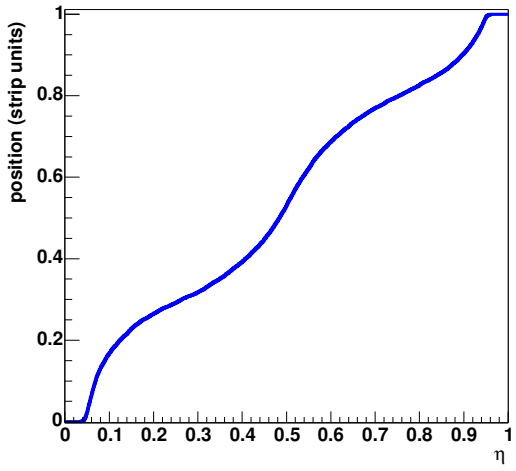

Figure 3.18. Position of the cluster with respect to the left strip as a function of η.

resolution of the beam telescope, each plane k is aligned with all the others, by minimizing

residuals in the system of linear equations

$$\sum_{i=1;\, i\neq k}^{8} [X_{ij} A_{ik}] + A_{0k} - X_{kj} = R_{kj} \tag{3.3}$$

where X_{ij} is the impact position in the plane i for the event j, R_{kj} are the residuals of the plane k for the event j. For each plane k the solution of this system are given by the coefficients A_{ik} and A_{0k}, which minimize the sum of residuals

$$\sum_{j=1}^{N} {R_{kj}}^2, \tag{3.4}$$

where N is the total number of events. For each beam telescope plane the residuals distribution was fitted with a Gaussian and the sigma is shown in Table 3.1: The residuals distribution for

X-Plane	Gaussian σ		Y-Plane	Gaussian σ
X1	1.2 µm		Y1	1.3 µm
X2	1.2 µm		Y2	1.2 µm
X3	1.5 µm		Y3	1.4 µm
X4	1.5 µm		Y4	1.6 µm

Table 3.1. Gaussian σ of the residuals distribution of each beam telescope plane.

the plane with the largest σ is shown in Fig. 3.19. Assuming that all planes have resolution as

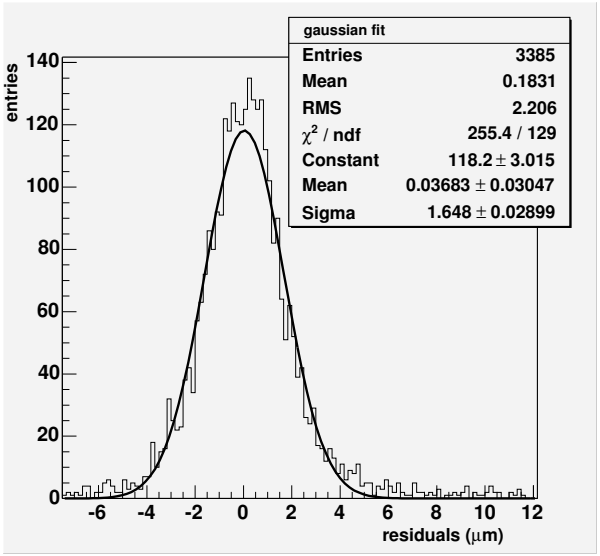

Figure 3.19. Residuals distribution for the 4^{th} Y plane of the beam telescope.

the worst plane, the intrinsic resolution of each beam telescope plane is roughly given by 1.6 µm/ $\sqrt{3}$. For the worst plane the resolution is better than 1 µm.

3.2.5. Alignment of pixel detector with the beam telescope

The purpose of the alignment is to find the relative displacements of all the detectors and predict the position of the particle track in the pixel sensor only using the beam telescope planes. A precise and independent determination of the impact position in the pixel plane is necessary to study charge collection efficiency as function of the intra pixel position. In addition, it is also used to measure the Lorentz angle and the resolution of the pixel sensors.

As the pixel sensor under study can be very noisy or contain unconnected pixels, especially if it operates at low bias voltage or after heavy irradiation, events in the pixel sensors have to be carefully selected. The hit pixels, given by the pixels with amplitude above a certain threshold, are searched in the detector. The indexes of the hit pixels are correlated with the ones in the beam telescope planes due to the event topology. The x position reconstructed with the pixel detector is shown in Fig. 3.20 as function of the x coordinate in one of the beam telescope planes. Correlation plots as the one shown in Fig. 3.20 are plotted for each coordinate and are used to set a restricted range in the pixel sensor where hits are reconstructed. Hits in the pixel sensors are searched a second time only in this range and are used for the alignment procedure. For the found hits the position in the pixel sensor and in the beam telescope planes

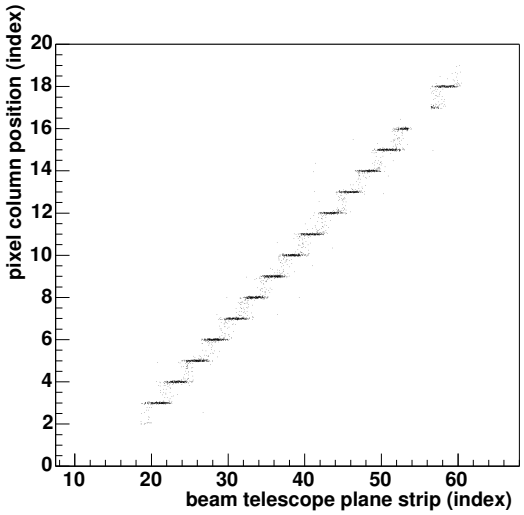

Figure 3.20. Correlation between positions in the pixel and the beam telescope planes.

are reconstructed as described in the Sections 3.2.2 and 3.2.4. The alignment is performed by minimizing residuals in the following system of equations

$$\sum_{i=1}^{8} [P_{ij} C_{xi}] + C_{x0} - X_j = R_{xj}, \tag{3.5}$$

$$\sum_{i=1}^{8} [P_{ij} C_{yi}] + C_{y0} - Y_j = R_{yj}, \tag{3.6}$$

where P_{ij} is the position in the beam telescope plane [4] i for the event j, X_j and Y_j are the x

[4]The index $i = [1, ..., 4]$ corresponds to the position in the x planes, while $i = [5, ..., 8]$ to the position in y

and y positions in the pixel coordinate system for the event j, R_{xj} and R_{yj} are the residuals in the x and y coordinates, respectively.

The solution of the system is a set of coefficients (C_{xi}, C_{x0}, C_{yi}, C_{y0}), which minimizes the squared sums of the residuals

$$\sum_{j=1}^{N} R_{xj}^2, \qquad \sum_{j=1}^{N} R_{yj}^2, \tag{3.7}$$

where N is the total number of events. The positions in the pixel coordinate system predicted by the beam telescope are given by

$$X_j = \sum_{i=1}^{8} [P_{ij} C_{xi}] + C_{x0}, \tag{3.8}$$

$$Y_j = \sum_{i=1}^{8} [P_{ij} C_{yi}] + C_{y0}. \tag{3.9}$$

The residuals distributions in the x and y direction are shown in Fig. 3.21 and Fig. 3.22, respectively.

The pixel residuals distribution is binary with a standard deviation equal to $1/\sqrt{12}$, because of events with no charge sharing between the pixels. In addition, no η correction to the pixel hit position is applied in the alignment procedure. However, the mean of the residual distribution is very close to zero, which indicates that the pixel plane is very well aligned with the beam telescope. Therefore, the precision of the position predicted by the beam telescope is limited only by the intrinsic resolution of the beam telescope itself, which is less than 1 μm. Since this precision is at least five times smaller than the expected pixel sensor resolution, the position predicted by the beam telescope position is defined as the true position of the beam entry point.

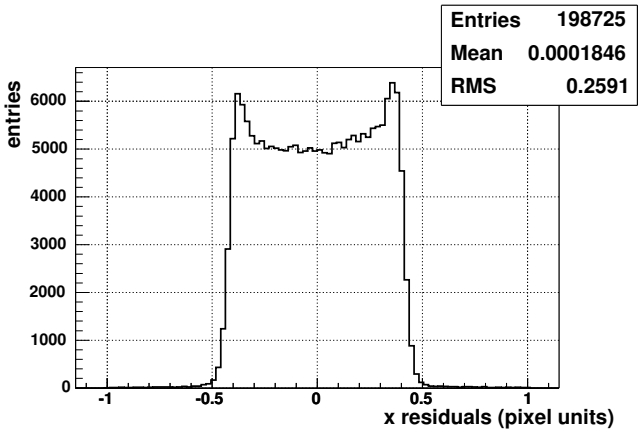

Figure 3.21. Residuals distribution in the x direction calculated with the alignment procedure. The magnetic field is 0 T.

planes.

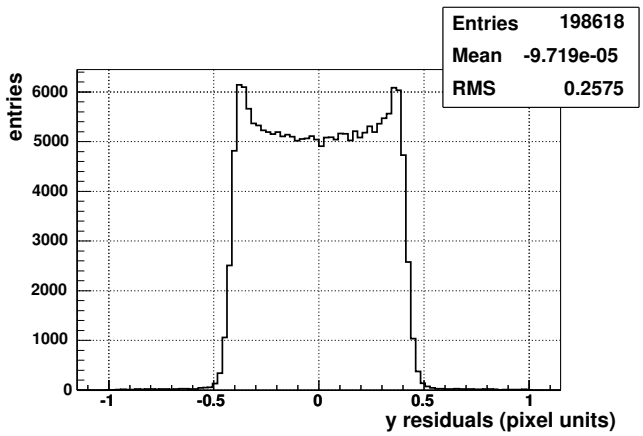

Figure 3.22. Residuals distribution in the y direction calculated with the alignment procedure. The magnetic field is 0 T.

Once the data reconstruction and the alignment are performed, the precise beam entry point in the pixel coordinates system and the corrected pixel amplitudes are available for further analysis. The reconstructed data are stored into `root` files which are used in the data analysis described in the next chapters.

4. Measurements of the silicon sensors properties

Physical properties of the sensors designed for the CMS pixel detector are measured and presented in this chapter. Charge collection efficiency, signal to noise ratio and the Lorentz angle are studied for both unirradiated and irradiated sensors. Measurements of the electric field in the bulk of silicon are also presented and validated with a simulation.

4.1. Tested sensors

The tested sensor designs, p–spray and p–stop, are shown in Fig. 4.1. Operation principles of these designs are described in Section 1.4. There are two geometries for the p–spray design,

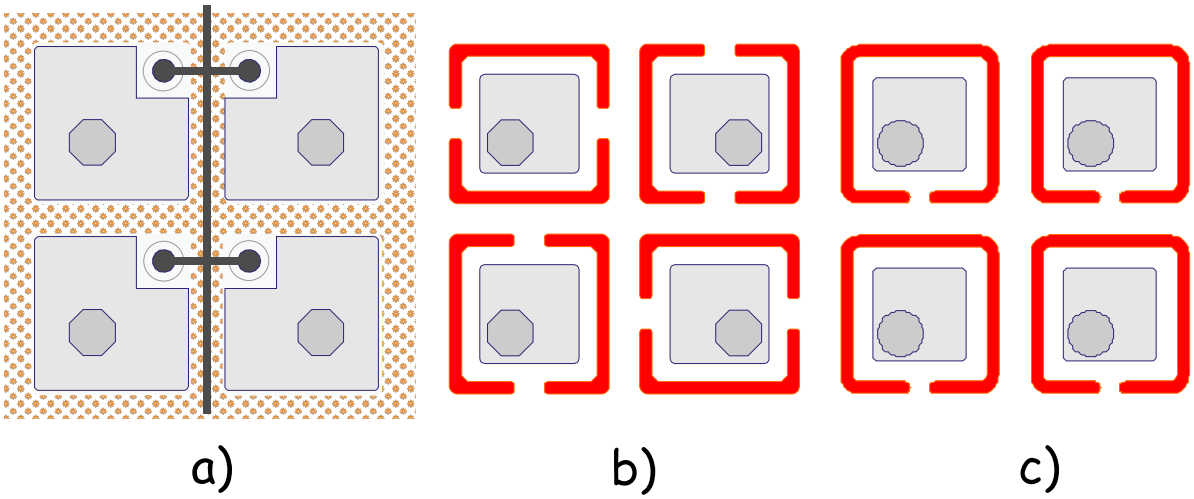

Figure 4.1. Sensor designs. a) p–spray manufactured by CiS, b) p–stop manufactured by CiS, c) p–stop manufactured by Sintef

which differ by the width of the inter–pixel gap. Sensors with an inter–pixel gap of 20 µm are called "Dot1", while the 30 µm are called "Dot3". A smaller gap size would improve the charge collection efficiency, but would also decrease the production yield. These sensors were produced by CiS[1].

The p–stop designs, called "OneRing", have different ring geometries. This ring geometry defines the resistivity between the pixel and it's neighbors. The symmetry of the interconnections in the two–opening ring geometry (Fig. 4.1b) produces a more uniform coupling between

[1]Institute for Micro Sensors, Erfurt, Germany.

the pixels, than the single opening geometry (Fig. 4.1c). The former were produced by CiS and the latter were produced by Sintef[2].

The sensors were irradiated at different hadron fluences, from 5×10^{13} to 2.6×10^{15} n_{eq}/cm^2, with 24 GeV protons from the CERN SPS. The sensors were then stored at -20°C and some later annealed at 30°C for 48 hours. All tested samples are summarized in Table 4.1. The readout chip used in the test beam setup is not radiation hard. Therefore the sensors were irradiated without the readout chips connected. The heat treatment to form the indium bumps on the sensors had to be performed before irradiation, to prevent annealing caused by the heating. After irradiation, sensors were connected to the readout chip. Thus, the second heat treatment that securely connects the readout chips to the sensors could not be performed. This procedure resulted in bad connections, that caused a lower connection stability and yield. The leakage current was measured as a function of bias voltage before and after irradiation,

Irradiation fluence, n_{eq}/cm^2	Annealed	design	sample name	note
0		p–spray	Dot1(CiS)	20 μm gap
0		p–stop	OneRing(CiS)	two openings
0		p–stop	OneRing(Sintef)	1 opening
5×10^{13}	48 hours at 30°C	p–spray	Dot1(CiS)	20 μm gap
6×10^{13}	48 hours at 30°C	p–stop	OneRing(Sintef)	1 opening
2×10^{14}	48 hours at 30°C	p–spray	Dot1(CiS)	20 μm gap
2×10^{14}	48 hours at 30°C	p–spray	Dot3(CiS)	30 μm gap
3×10^{14}		p–stop	OneRing(CiS)	two openings
6×10^{14}	48 hours at 30°C	p–spray	Dot1(CiS)	20 μm gap
6×10^{14}	48 hours at 30°C	p–stop	OneRing(Sintef)	1 opening
6.7×10^{14}		p–spray	Dot1(CiS)	20 μm gap
6.7×10^{14}		p–stop	OneRing(CiS)	two openings
9.7×10^{14}		p–spray	Dot1(CiS)	20 μm gap
1.2×10^{15}	48 hours at 30°C	p–spray	Dot1(CiS)	20 μm gap
2.6×10^{15}	48 hours at 30°C	p–spray	Dot3(CiS)	30 μm gap

Table 4.1. The tested silicon sensors.

as shown in Fig. 4.2. The measurements were done with Keithley 2400 Sourcemeter at a temperature -20°C. The current is very small for the unirradiated samples, while after the irradiation it increases by a few orders of magnitude and can reach 0.1 mA per sensor at -20°C. The voltage at which the current starts to sharply rise, the breakdown voltage, is much higher than the operational voltage, approximately 100 V for unirradiated and 450 V for irradiated.

[2]SINTEF, Oslo, Norway.

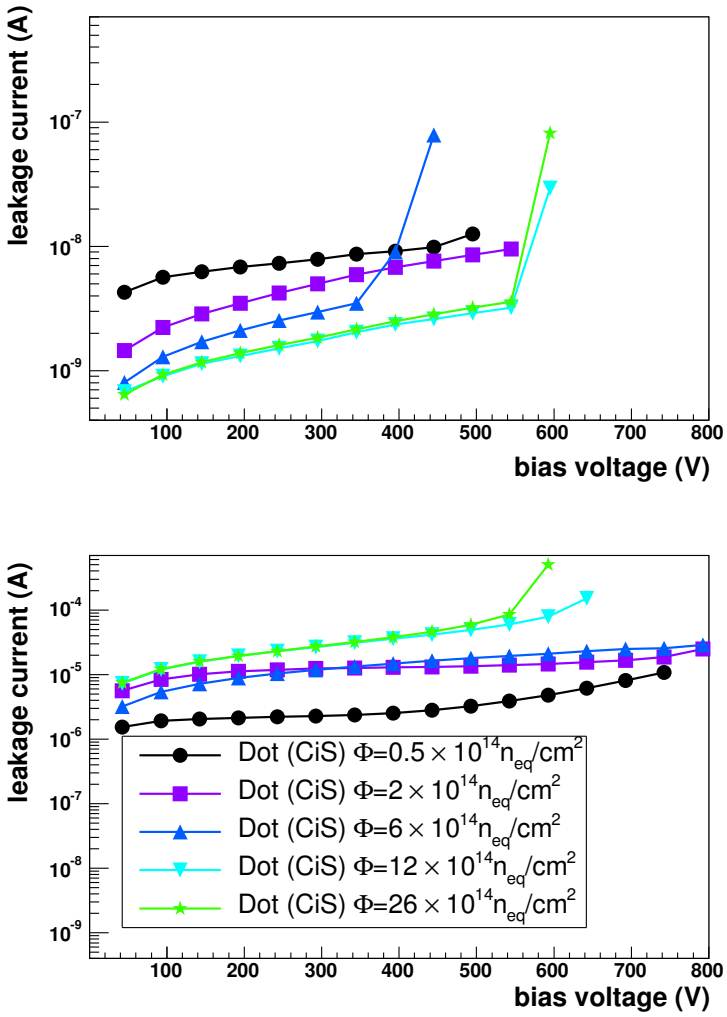

Figure 4.2. Leakage current before (top) and after irradiation (bottom) for the same sensors. The same sensors are represented by the same markers on both plots.

4.2. Position dependence of charge collection

The signal depends on the position of the incident particle within the pixel cell. The region with the highest collection efficiency is in the central part of the pixel, a centered square of 40×40 μm^2. Signals from tracks that crossed this area perpendicularly were used to mea-

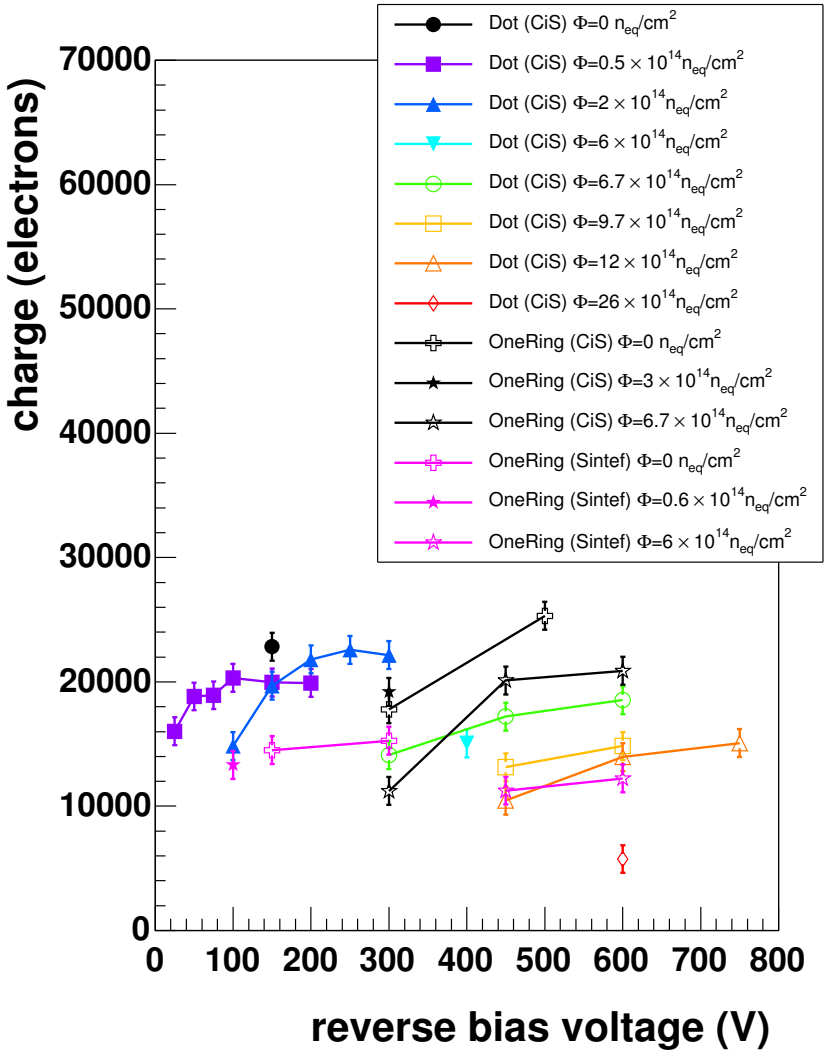

Figure 4.3. Average charge collected in the central part of the pixels, a square region of 40×40 μm^2. Particle tracks are normal to the pixel plane.

sure the maximum charge collection efficiencies. The average signals are shown in Fig. 4.3 as a function of applied bias voltage. The charge collection efficiency is about 60% for all designs after irradiation with fluence below $1.2\times10^{15}\,n_{eq}/cm^2$, while only 25% for a fluence of $2.6\times10^{15}\,n_{eq}/cm^2$. The fluence after first four years of operation at the innermost barrel layer is $6\times10^{14}\,n_{eq}/cm^2$.

The signal of the hit pixel as a function of the impact position is shown in Fig. 4.4. The

p–spray design is shown in the left column, while the p–stop design is in the right column. Measurements are performed at different irradiation fluences and bias voltages. For the

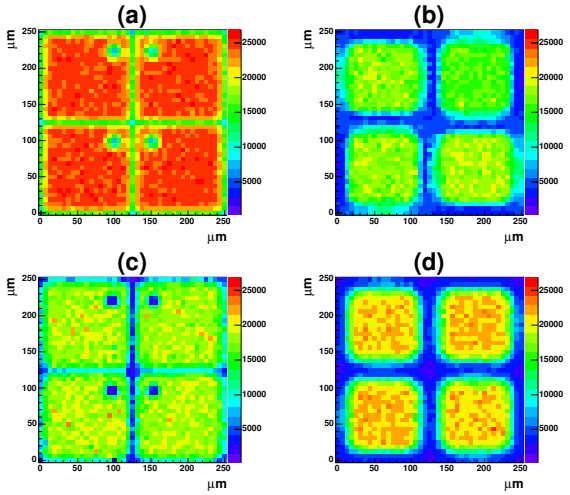

Figure 4.4. Average charge collected in the hit pixel at different irradiation fluences and bias voltages. The left column shows the Dot1(CiS): (a) unirradiated at 150 V, (c) $6.7\times10^{14}\,n_{eq}/cm^2$ at 450 V. Right column shows the OneRing(CiS) design: (b) unirradiated at 300 V, (d) $6.7\times10^{14}\,n_{eq}/cm^2$ at 450 V.

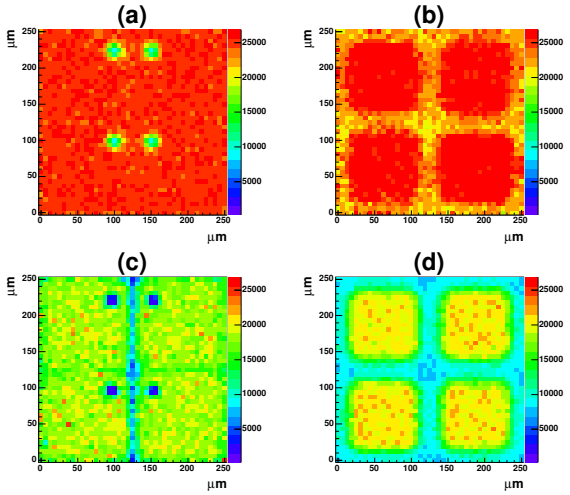

Figure 4.5. Sum (in electrons) of the signals of the hit pixel and its nearest neighbors in 3×3 cluster. Left column is Dot1(CiS): (a) unirradiated at 150 V, (c) $6.7\times10^{14}\,n_{eq}/cm^2$ at 450 V. Right column is OneRing(CiS): (b) unirradiated at 300 V, (d) $6.7\times10^{14}\,n_{eq}/cm^2$ at 450 V.

p–stop design the signal in the regions corresponding to the p–stop rings is lower than what observed in the pixel center. For the p–spray design a lower signal is observed in the punch–

through structures and along the biasing grid. From the Fig. 4.4 one can conclude, that unirradiated p–spray and p–stop designs have both inter–pixel region with reduced charge collection. However, the size of this region can be reduced by increasing the bias voltage. After irradiation a fraction of the charge is trapped and the charge collected in the pixel center is lower. The signal measured in the center of the p–stop pixel cell is lower than the respective value for the p–spray design (Fig. 4.4(a) and (b)). This effect due to the larger signal sharing between neighboring pixels in the case of the p–stop design.

The sum of the signals of 3×3 pixels clusters around the hit pixel are shown in Fig. 4.5 for the two designs. For the unirradiated sensors of both designs, the total signal is almost uniformly distributed within the pixel area with the exception of the regions corresponding to the punch–through structures of the p–spray design. By comparing Fig. 4.4(a,b) and Fig. 4.5(a,b) we observe that before irradiation the charge between pixels is not lost but shared between neighboring pixels. On the other hand, charge losses are observed after irradiation along the bias grid for the p–spray design. For the p–stop design the charge losses are located along the p–stop rings. The regions with the punch-through structures show always charge losses independently on irradiation. The charge collection efficiency in the pixel center and in the

Design	Fluence, n_{eq}/cm^2	Bias, V	CCE , center, %	CCE 3×3 pixels, center, %	CCE , gap, %	CCE 3×3 pixels, gap, %
p–spray	0	150	100	103	62	101
p–stop	0	300	71	110	22	92
p–spray	6.7×10^{14}	300	61	59	27	47
p–stop	6.7×10^{14}	300	48	45	10	23
p–spray	6.7×10^{14}	450	76	76	32	58
p–stop	6.7×10^{14}	450	88	84	15	37

Table 4.2. The charge collection efficiency (CCE) for p–spray and p–stop designs in the center of the pixel and in the gap. All values are referenced to CCE for the unirradiated p–spray sensor.

gap is summarized in Table 4.2. The values are normalized to the unirradiated p–spray sensor. The CCE increases with bias voltage for the irradiated sensors. The irradiated p–spray and p–stop sensors at the same bias voltage have similar CCE in the center of the pixel, but the CCE in the gap approximately twice larger for the p–spray design.

The signal of the hit pixel as function of the particle position for different irradiation fluences is shown in Fig. 4.6 for the p–spray design. The signal decreases in all areas of the pixel cell with the irradiation fluence and at the highest fluence of $2.6\times10^{15}\,n_{eq}/cm^2$ is about 25% of the signal of the unirradiated sensor (Table 4.3).

The corresponding measurements for the p–stops designs is shown in Fig. 4.7. The design with one opening is shown in left column, while the design with two openings is shown in the right column. In both cases, the signal losses become more pronounced after irradiation in the regions between pixels. The charge collection efficiency for different p–stop designs is shown in Table 4.4. The CCE for the design with two openings is higher, and the p–stop design with one openings needs to be improved.

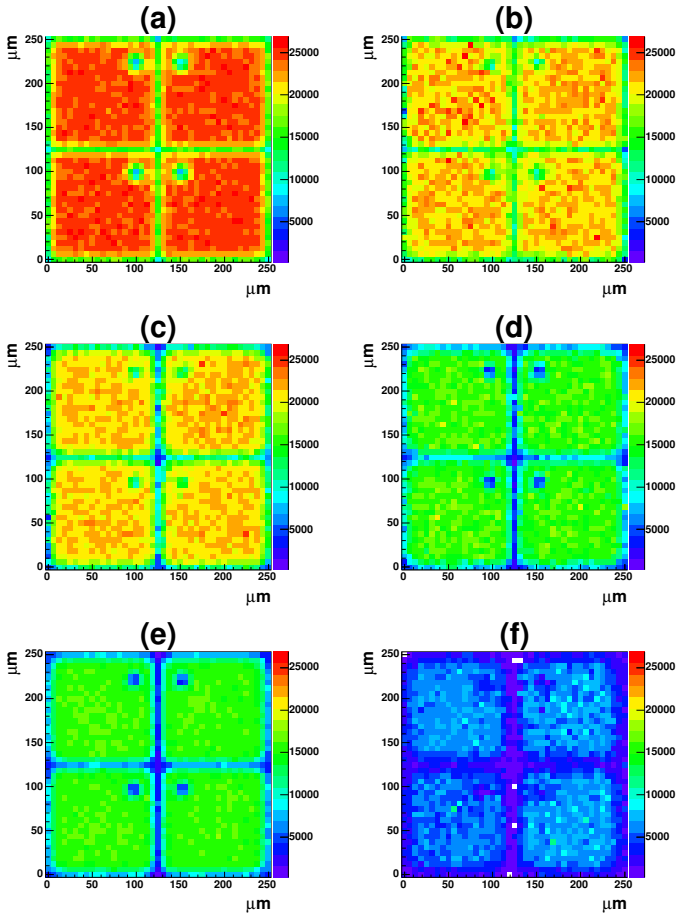

Figure 4.6. Signal in the hit pixel (p–spray design) for different fluences and bias voltages. (a) at 150 V, (b) 0.6×10^{14} n_{eq}/cm^2 at 100 V, (c) 2×10^{14} n_{eq}/cm^2 at 200 V, (d) 6×10^{14} n_{eq}/cm^2 at 400 V, (e) 12×10^{14} n_{eq}/cm^2 at 750 V, (f) 26×10^{14} n_{eq}/cm^2 at 600 V,

Irradiation fluence, n_{eq}/cm^2	CCE , center %	CCE, gap %
0	100	62
6×10^{13}	88	55
2×10^{14}	88	42
6×10^{14}	65	29
1.2×10^{15}	64	26
2.6×10^{15}	27	8

Table 4.3. The charge collection efficiency (CCE) for p–spray design in the center of the pixel and in the gap for different fluences. All values are referenced to CCE for the unirradiated p–spray sensor.

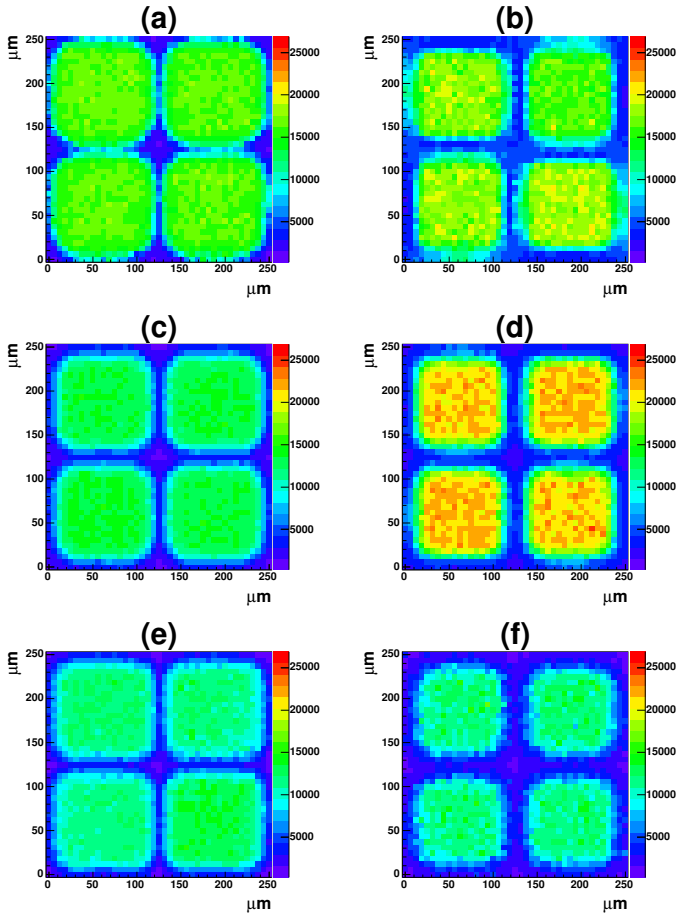

Figure 4.7. Signal in the hit pixel, (a) OneRing(Sintef) at 300 V, (b) OneRing(CiS) at 300 V, (c) OneRing(Sintef) $0.6\times10^{14}\,n_{eq}/cm^2$ at 100 V, (d) OneRing(CiS) $8\times10^{14}\,n_{eq}/cm^2$ at 450 V, (e) OneRing(Sintef) $6\times10^{14}\,n_{eq}/cm^2$ at 450 V, (f) OneRing(CiS) $8\times10^{14}\,n_{eq}/cm^2$ at 300 V

Design feature	Fluence, n_{eq}/cm^2	Bias, V	CCE , center, %	CCE , gap, %
one opening	0	300	67	34
two openings	0	300	71	35
one opening	6×10^{13}	100	55	20
two openings	6.7×10^{14}	300	48	15
one opening	6.7×10^{14}	450	50	20
two openings	6.7×10^{14}	450	88	24

Table 4.4. The charge collection efficiency (CCE) for p–stop designs with one and two openings in the rings. All values are referenced to CCE for the unirradiated p–spray sensor.

4.3. Signal–to–noise ratio

The noise is determined from the Gaussian fit (σ) of the pixel amplitudes recorded during the SPS spill gaps. The signal is defined as the average charge in the hit pixel measured with tracks normal to the sensor plane. Events are uniformly distributed over the detector surface. The bias voltage for each sensor was set to a value found using the charge collection efficiency measurements described in Section 4.4.4. These measurements are performed at different bias voltages and the bias voltage is set to the minimal value at which the charge collection efficiency reaches the plateau. The signal–to–noise ratio for the p–spray design is shown in Fig. 4.8 as a function of the irradiation fluence [3].

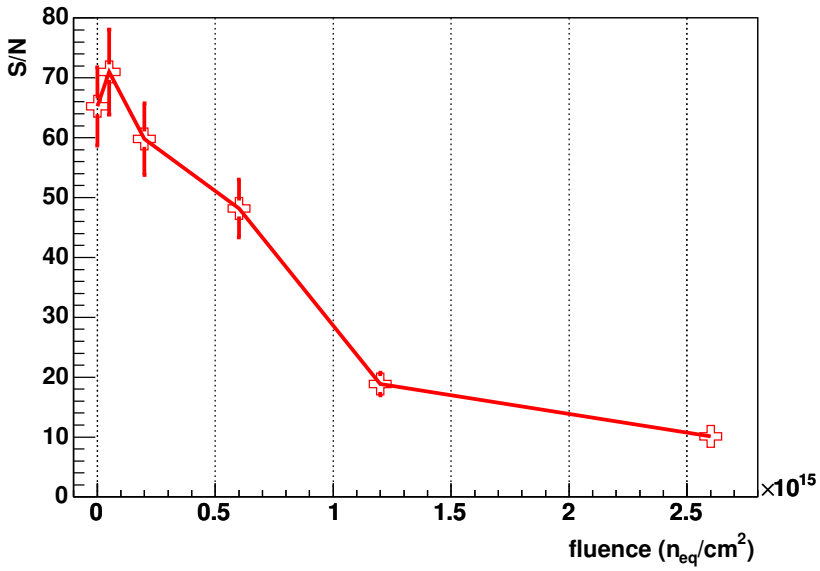

Figure 4.8. Signal–to–noise ratio measured with the p–spray sensors as a function of irradiation fluence.

The signal–to–noise ratio is about 70 at low irradiation fluences, while it drops down to 10 after $2.6\times10^{15}\,\mathrm{n_{eq}/cm^2}$.

The signal–to–noise after first four years of operation of the CMS pixel detector at the innermost layer is about 48, which is still rather high (for p–spray). In addition, these measurements are not performed with the final version of the pixel readout chip, which is expected to have a lower noise.

The signal–to–noise ratio for the two p–stop designs exposed to different fluences is shown in Table 4.5. The signal–to–noise ratio for p–stop is almost half of the corresponding p–spray values, because the signal spreads among several pixels. Therefore, the signal collected in the hit pixel is smaller. However the signal–to–noise ratio for p–stop designs is still high and weakly dependent on irradiation.

[3] The sensor exposed to $2.6\times10^{15}\,\mathrm{n_{eq}/cm^2}$ is "Dot3" of Table 4.1, while all other sensors are of the "Dot1" type.

Detector type	Bias	Irradiation fluence	S/N
OneRing (CiS)	500 V	0 n_{eq}/cm^2	34
OneRing (CiS)	300 V	3×10^{14} n_{eq}/cm^2	38
OneRing (CiS)	450 V	6.7×10^{14} n_{eq}/cm^2	41
OneRing (Sintef)	300 V	0 n_{eq}/cm^2	51
OneRing (Sintef)	100 V	6×10^{13} n_{eq}/cm^2	42
OneRing (Sintef)	450 V	6×10^{14} n_{eq}/cm^2	44

Table 4.5. Signal–to–noise ratio measured with the p–stop sensors.

4.4. Particle detection efficiency

4.4.1. Event and pixels selection

The particles detection efficiency is determined using tracks normal to the pixel plane. Events are selected using the impact position reconstructed using the beam telescope as described in Section 3.2.2. The predicted position must be located inside the pixel sensor area. The pixels were carefully selected in order to be used for particles detection efficiency calculation. The pixels on the borders, not connected pixels and noisy pixels were excluded from the analysis. Some pixels had bad connection to the amplifier and the signals from them were too small

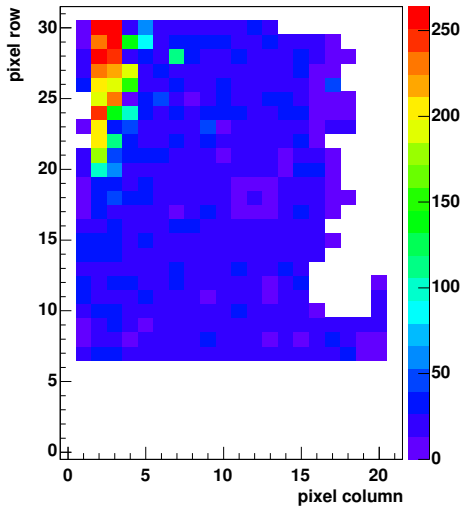

Figure 4.9. Number of events (color scale) with amplitudes below 0.2 mip in each of 22×32 pixels. The well defined region in the pixel sensor (upper left corner) is the location of badly connected pixels.

in comparison to the good pixels. These pixels usually were located in a certain region. The location of badly connected pixels was found and the pixels were excluded from analysis.

The example of the selection procedure is given below for the unirradiated p–spray sensor

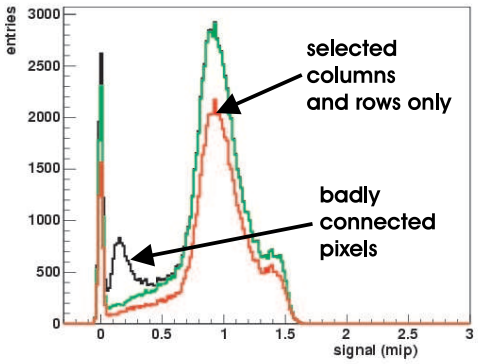

Figure 4.10. Signal amplitude distributions. The black histogram corresponds to all pixels. The green histogram corresponds to pixels which have good connections to the amplifier. The red histogram represents the signal distribution, excluding entire columns and rows which contain bad pixels.

in 0 T magnetic field and with tracks perpendicular to the sensor surface. The same selection procedure was applied to all sensors.

Badly connected pixels can be located by calculating the number of events with amplitudes below 0.2 mip in each pixel as shown in Fig. 4.9. The signal distribution for all pixels is plotted

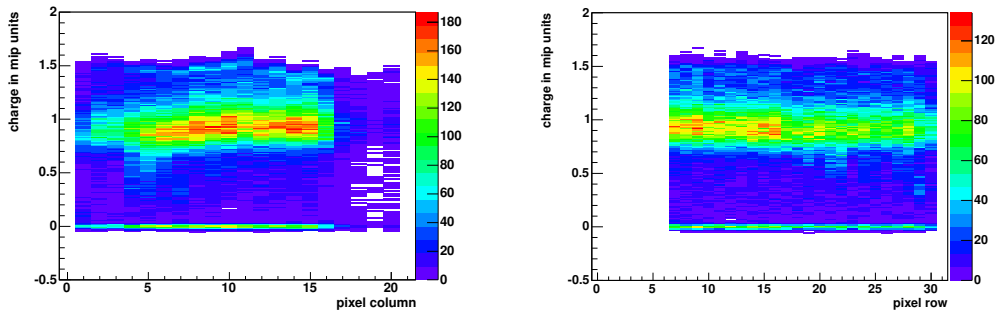

Figure 4.11. Column (left) and row (right) dependence of the pixel amplitude distribution. The color scale represents the number of events of a certain amplitude in a column (left) or in a row (right).

as a black histogram in Fig. 4.10. There is a peak around 0.2 mip which corresponds to badly connected pixels. Badly connected pixels were excluded and the signals distribution of the remaining pixels is represented by the green line in Fig. 4.10. The observed region of badly connected pixels can be explained by modification of the bump bonding procedure. The heat treatment of the bump bonded sensors is not possible after irradiation and, hence, some bumps have bad connection. These pixel cells usually have a low signal. Therefore, pixels with excess of events with signal below 0.2 mip are excluded from further analysis.

The signal distribution in each column and row is presented in Fig. 4.11. The color scale

represents the number of events of a certain amplitude in a column (left) or in a row(right). It was observed that the peak of the signal distribution for some columns or rows different from the other columns or rows. For example, the columns 1,2,3,4 in the left part of the Fig. 4.11 have peak of the distribution around 0.8 mip[4], while the rest columns have the peak around 1 mip. Such columns and rows were excluded from the analysis and the signal distribution for the remaining pixels is shown as red line in Fig. 4.10.

The readout related inefficiencies were investigated and excluded. From the measurements in Section 4.2 we observe that the average signal depends on the particle impact position, but there are no areas where zero charge is collected. In the distribution shown in Fig. 4.10 there is a peak around zero. The width of this peak is mainly attributed to the pixel preamplifier noise. In addition, the impact position of the events in the peak is not correlated to any region with low charge collection (e.g. punch–through structures, p–stop rings, pixes borders etc.). The fraction of events and the width of this peak is not sensitive to the track crossing angle. Even for data for tracks at a shallow impact angle where particles spread signal across up to eight consecutive pixels. In this case, none of the eight pixels detects a signal above noise. The conclusion from these observations is the following: the excess of events around zero amplitude is not related to the pixel sensor inefficiency, but rather to inefficiencies in the time correlation between the beam telescope and a sensor. The beam telescope preamplifier has a much higher integration time (2 μs) respect to the pixel preamplifier, which is about 30 ns. Therefore, good tracks may be reconstructed in the beam telescope that are not recorded during the pixel integration time. In order to exclude these events from the efficiency analysis the peak around zero was fitted with the sum of a Gaussian and a first order polynomial function, and the Gaussian part was subtracted from the signal distribution.

4.4.2. Particle detection efficiency without magnetic field

The signal distributions of the selected events for the irradiated p–spray design are shown in Fig. 4.12 for different irradiation fluences. With increasing fluence the bias voltage has to be increased until the sensor collects charge from the whole sensor thickness. Events with a low signal are located along the biasing grid and along the pixel borders. The average signal of the sensor irradiated at the highest fluence is about 25% of the respective value of the unirradiated sensor.

The number of hits below a certain threshold is given by the integral of the signal distribution up to the threshold value. The particles detection inefficiency (or fraction of lost hits) is obtained by dividing this number by the total number of events. The fraction of lost hits for the p–spray design as a function of the threshold is shown in Fig. 4.13 for different irradiation fluences. Assuming that the threshold is set to five times the noise value, i.e. 2000 electrons, the fraction of lost hits for the p–spray design after four year of operation is about 1% in the innermost layer. The signal amplitudes distribution and the fraction of lost hits for the p–stop designs are shown in Fig. 4.14 and Fig. 4.15, respectively. The corresponding fraction of lost hits for the p–stop design with two openings is 1% with a threshold of 2000 after the first four years of operation. The respective value for the p–stop design with one opening is 5%. This difference for two p–stop designs is related to the different geometry of the p–stop rings and to the larger charge spread observed with the one–opening type. For the p–stop design the increase of the particles detection inefficiency with increasing threshold is faster than for the

[4]This cut value was adjusted individually for each sensor, for example for irradiated sensors it was smaller.

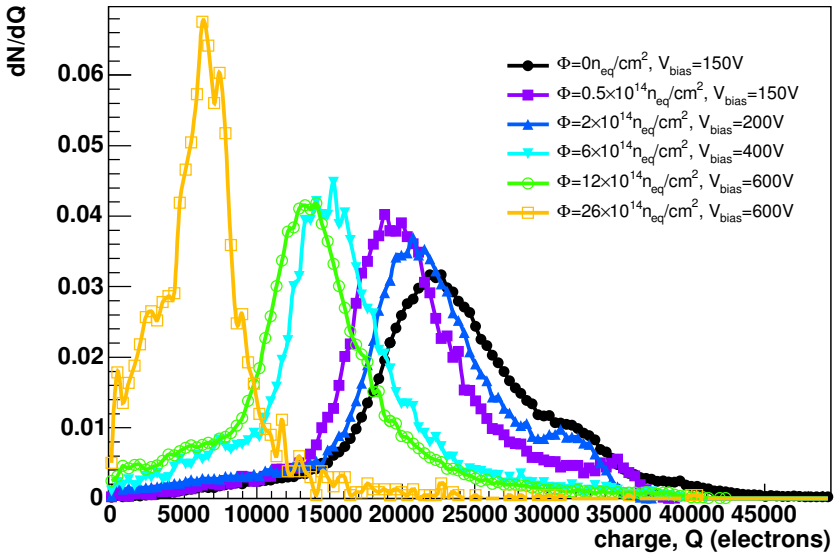

Figure 4.12. Signal distribution for the p–spray design for different irradiation fluences The distributions are normalized to the total number of events.

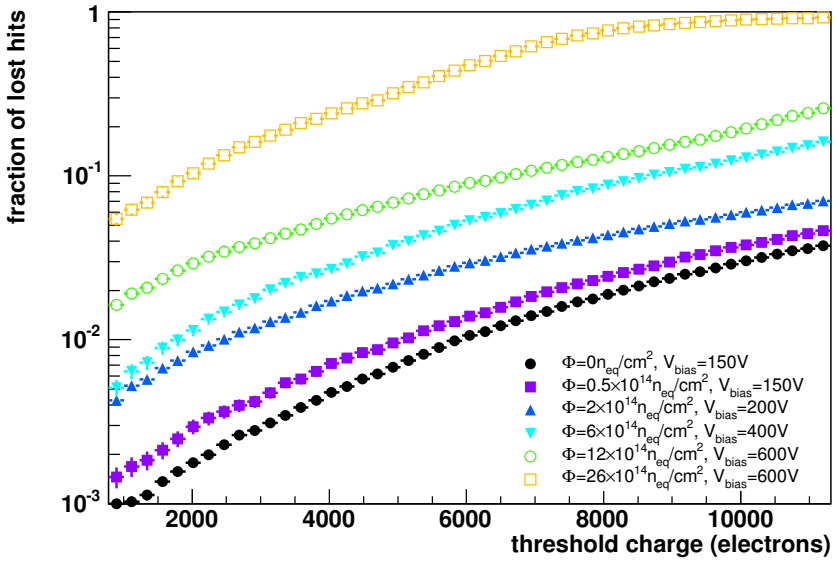

Figure 4.13. Particles detection inefficiency for the p–spray design for different irradiation fluences as a function of threshold.

p–spray design. This is due to the smaller area of reduced charge collection in the p–spray design (Fig. 4.4 and 4.7).

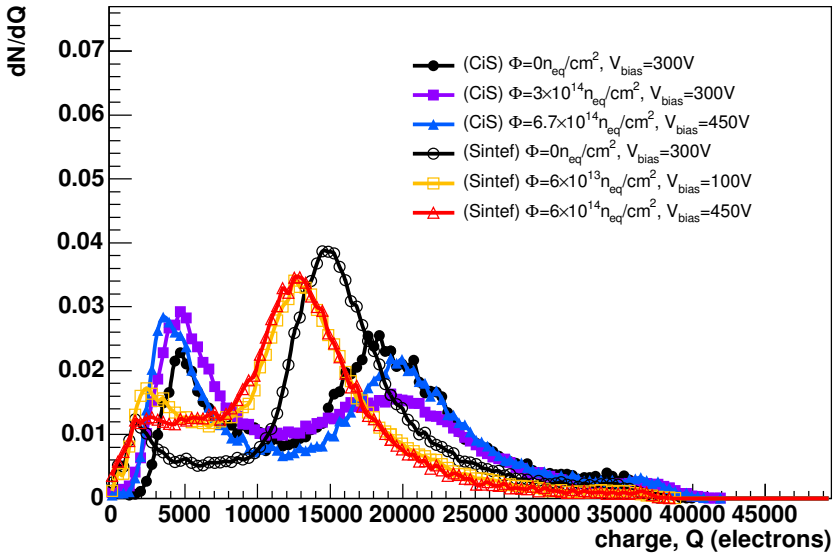

Figure 4.14. Signal distribution for the p–stop design at different irradiation fluences.

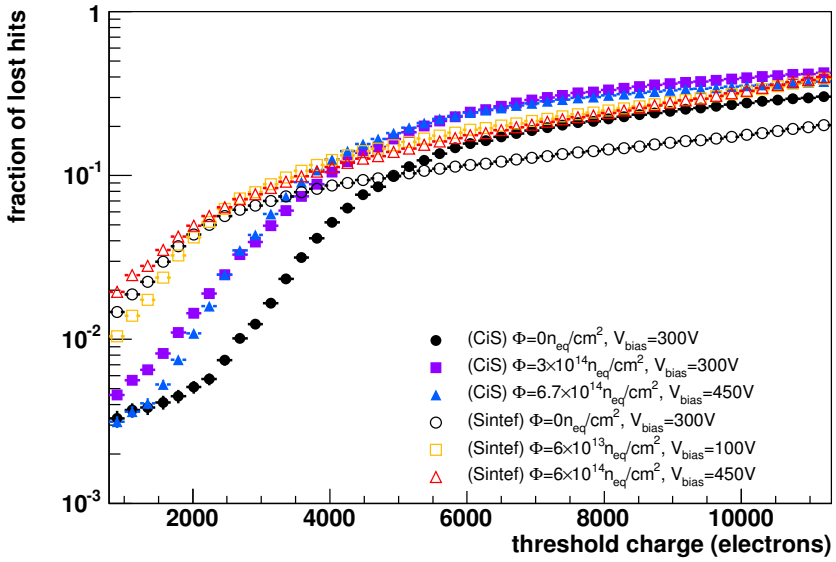

Figure 4.15. Particles detection inefficiency for the p–stop design at different irradiation fluences as a function of threshold.

4.4.3. Particle detection efficiency in the magnetic field and at different incident angles

In the presence of magnetic field electrons and holes are deflected by the Lorentz force. Therefore, the signal spreads between more pixels. This effect can influence the particle detection

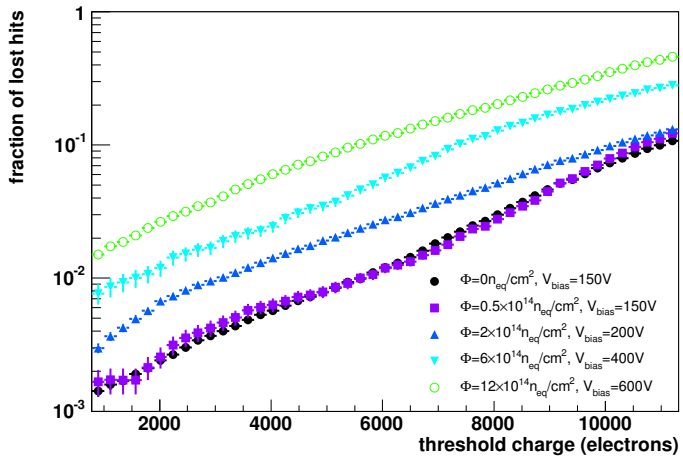

Figure 4.16. Particles detection inefficiency of the p–spray design for different irradiation fluences in the presence of the magnetic field of 3 T. The particle tracks are perpendicular while the magnetic field is parallel to the pixel plane.

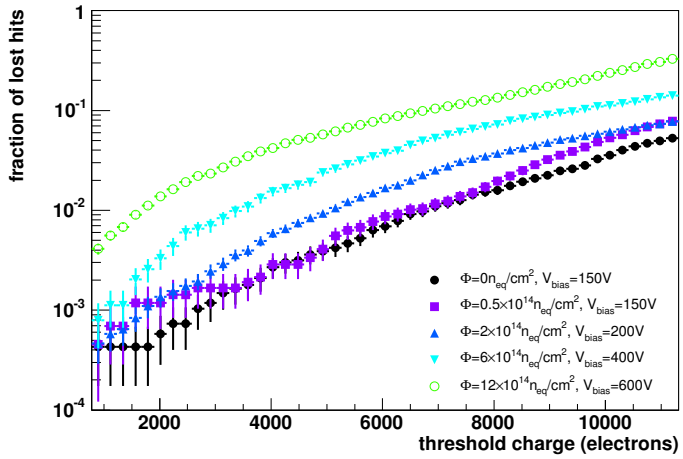

Figure 4.17. Particles detection inefficiency of the p–spray design for different irradiation fluences in the presence of the magnetic field of 3 T. The particles are incident at angle 10° to the normal of the pixel plane. The magnetic field is parallel to the pixel plane.

efficiency. The fraction of lost hits as a function of thresholds in the presence of magnetic field is shown in Fig. 4.16 for the p–spray design. The 3 T magnetic field is parallel to the pixel plane and tracks are normal to the pixel plane. Fig. 4.17 shows the fraction of lost hits when the impact angle with respect to the normal direction is 10°. The corresponding plot for an angle of -10° is shown in Fig. 4.18. In this case the spread due to the Lorentz force is

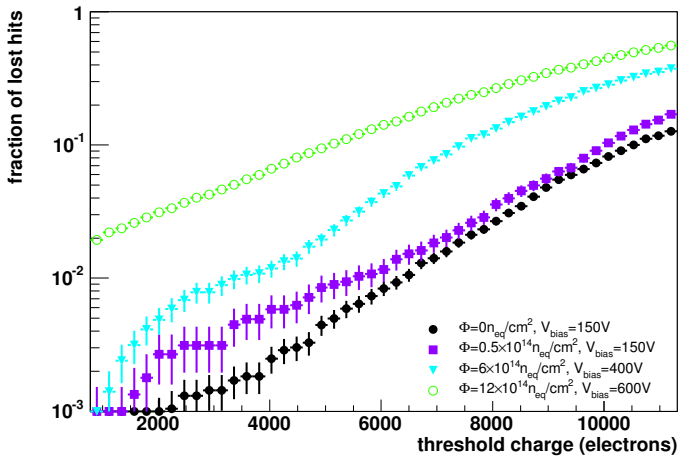

Figure 4.18. Particles detection inefficiency of the p–spray design for different irradiation fluences in the presence of the magnetic field of 3 T. The particles are incident at angle -10° to the normal of the pixel plane. The magnetic field is parallel to the pixel plane.

larger than for perpendicular tracks. The fraction of the lost hits with magnetic field is slightly higher when the tracks are incident perpendicularly to the pixel plane. This effect is due to the higher signal spread between pixels. The particle detection efficiency depends very weakly on the magnetic field.

4.4.4. Charge collection efficiency as a function of sensor depth

The charge collection efficiency is a function of the location of the charge deposition in the sensor bulk. The electron–holes pairs created throughout the depth of the bulk of a fully

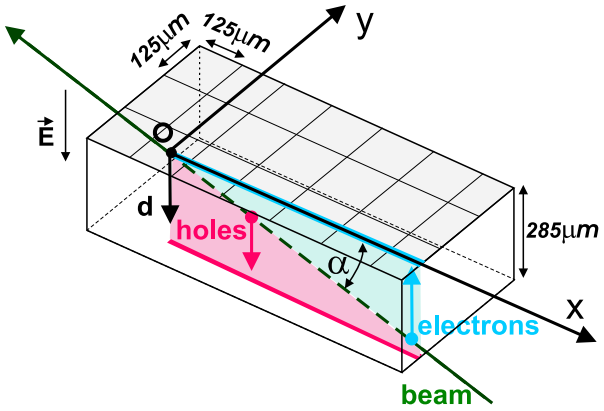

Figure 4.19. Principle of the charge collection measurements. The signal in the pixels along the x axis probes the charge collection efficiency at a certain depth, d.

depleted unirradiated sensor reach the electrodes and contribute to the signal, while for irradiated sensors, the variation of the electric field, and the trapping centers modify the probability that charge reaches the electrode.

The charge collection efficiency was measured with particles crossing the sensor at a shallow angle of $\alpha = 15°$ with respect to the pixel plane (Fig. 4.19). The sensor was aligned in such a way that the beam crosses along a pixel row, x axis in Fig. 4.19. The particle exits the sensor at the point "O". This point is defined as (0,0) in the xy plane. Electrons and holes created in the silicon bulk are collected along the x axis. The signal induced on a specific pixel electrode depends on the position of the pixel center in the xy plane. The relation between a pixels

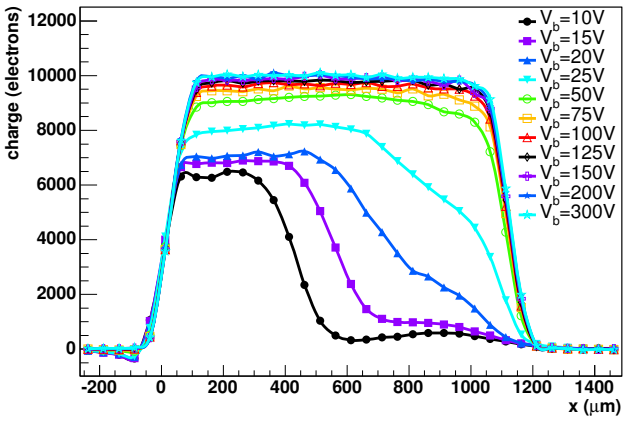

Figure 4.20. Signal as a function of the distance to the track exit point for the p–spray sensors exposed to a fluence $0.5{\times}10^{14}\,\mathrm{n_{eq}/cm^2}$ for different bias voltages.

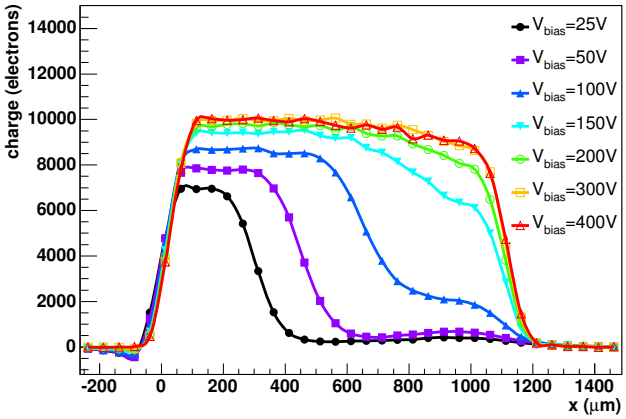

Figure 4.21. Signal as a function of the distance to the track exit point for the p–spray sensors exposed to a fluence $2{\times}10^{14}\,\mathrm{n_{eq}/cm^2}$ for different bias voltages.

position x and the origin of the electron–hole pairs, d, is given by $d = x \tan\alpha$. Hence, by

measuring the signal as a function of distance from the particle exit point "O" one probes the charge collection efficiency at a certain depth. The signal was averaged over the pixel along y, since the particle entry positions were uniformly spread in y. The averaged signal is shown as a function of x for various bias voltages for a fluence of $0.5\times10^{14}\,\mathrm{n_{eq}/cm^2}$ (Fig. 4.20), for a fluence of $2\times10^{14}\,\mathrm{n_{eq}/cm^2}$ ((Fig. 4.21) and for a fluence of $6\times10^{14}\,\mathrm{n_{eq}/cm^2}$ (Fig. 4.22). After

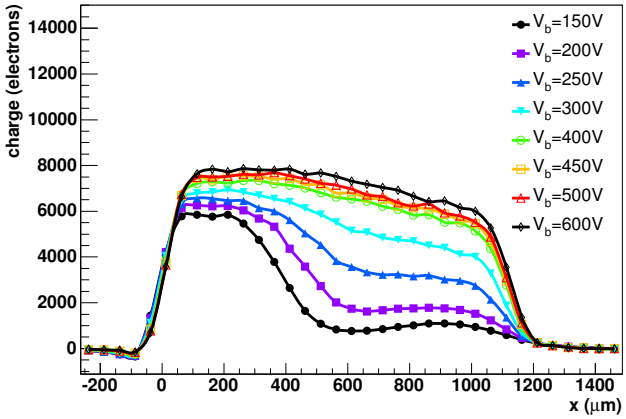

Figure 4.22. Signal as a function of the distance to the track exit point for the p–spray sensors exposed to a fluence $6\times10^{14}\,\mathrm{n_{eq}/cm^2}$ for different bias voltages.

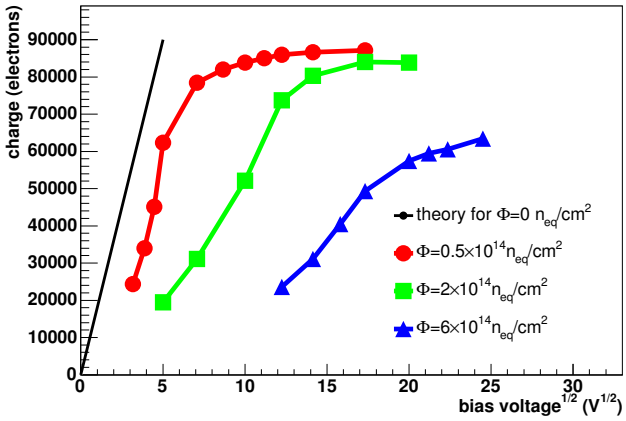

Figure 4.23. The total collected charge as a function of the square root of the bias voltage for p–spray designs. The three curves correspond to different irradiation fluences.

irradiation and type inversion the depletion starts from the implant side. Thus charge will be collected from the depletion region close to the pixel implant at low bias voltages. However, the measured dependence of charge collection efficiency indicates that even at low bias voltages the charge is collected from both side of the sensor. This means that for the irradiated sensors the depletion starts from both sides of the sensor bulk.

In the usual picture the total collected charge is proportional to $\sqrt{V_{bias}}$ (Eq. 2.1), up to the full depletion voltage. The sum of the signals from all pixels along the particle trajectory, the total collected charge is shown in Fig. 4.23 as a function of $\sqrt{V_{bias}}$. These curves do not exhibit the classical $\sqrt{V_bias}$ shape. This is attributed to the behavior of the electric field which does not follow the usual behavior (Fig. 2.1) explained for an unirradiated device. Measurements of the electric field in the bulk are presented and discussed in Section 4.6.

4.5. Measurement of the Lorentz angle

In the presence of the magnetic field the Lorentz force acts on the moving electrons and holes, which are deflected from their drift along the electric field lines. The deflection angle is called the Lorentz angle (Θ_L). In this work two basic techniques are used to measure the Lorentz angle, the angle scan and the grazing angle method (Fig. 4.24). In the angle scan method,

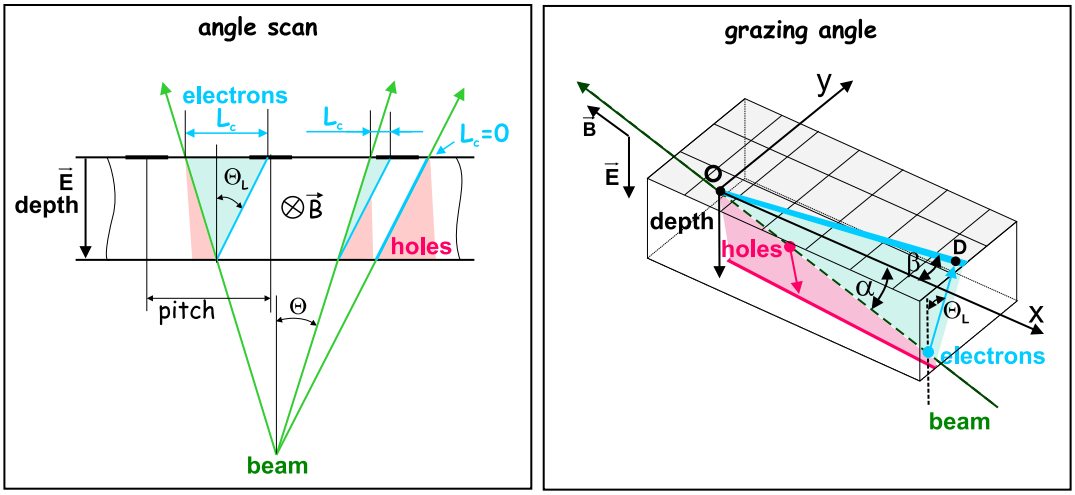

Figure 4.24. Two methods for the Lorentz angle measurements. The angle scan methods (left) and the grazing angle method (right).

the beam enters the plane at various angles Θ with respect to the normal to the sensor plane. The cluster length L_c is determined with the Lorentz angle and the angle Θ. L_c is a minimum when the Lorentz angle is equals to Θ. This method was used in [25] for measuring the Lorentz angle in silicon strip sensors. In the case of the sparse readout, where only the strips above a certain threshold are read out, the cluster length L_c depends on the threshold. Therefore the L_c has to be properly modeled. This approach was used for microstrip detectors [26].

In the grazing angle method [27] the beam enters the sensor plane at a shallow angle α and the signal from the electrons is induced along the segment "OD" Fig. 4.24. Knowing the position of "OD" and the angle β on the xy plane, one can derive the Lorentz angle

$$\tan\Theta_L = \tan\beta / \tan\alpha. \tag{4.1}$$

The angle scan method gives a Lorentz angle averaged over the sensor depth, while with the grazing angle measures the Lorentz angle as a function of the sensor depth. The fact that the Lorentz angle in the irradiated sensor depends on the depth was spotted in [9], but was

not understood nor studied in detail. In Section 4.6 the detailed measurement of the Lorentz deflection as a function of the depth is presented.

4.5.1. Lorentz angle with the angle scan method

The charge fraction as a function of the distance to the pixel center is shown in Fig 4.25(a). The charge normalized to the maximum value at the pixel center. The magnetic filed is 3 T and the angle Θ is -10° . The charge is spread over the length L_c. The larger the distance to the pixels center the smaller fraction of the charge is collected by the pixel. The points at which the charge fraction is 80% and 20% used to estimate the charge spread. The distance between these two points determines the charge spread length. The charge spread length was measured for each scanned value of the angle, and the length dependence on the angle is fit to a parabola shown in Fig. 4.25(b). The minimum of the parabola determines the Lorentz angle.

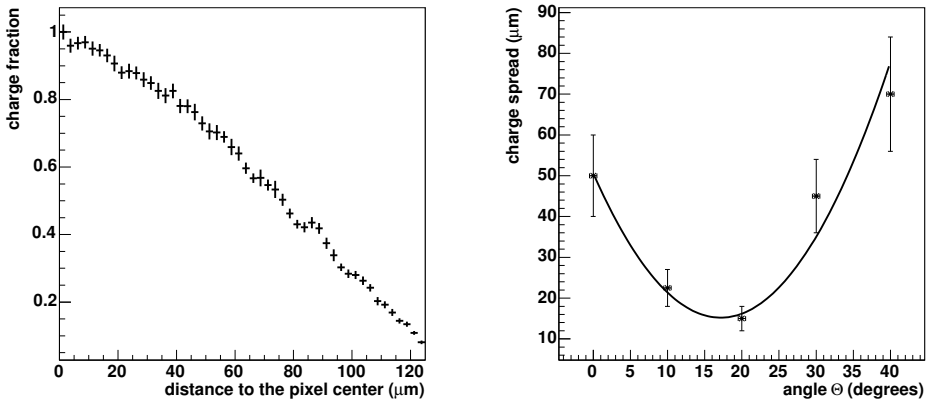

(a) (b)

Figure 4.25. a) Signal in pixel as a function of distance to the pixel center in a 3 T magnetic field and angle $\Theta = -10°$. b) Parabolic fit of the angular dependence of the charge spread.

The measured averaged Lorentz angle for the p–spray design for different fluences with the angle scan method is shown in Tab. 4.6. The measured value of the Lorentz angle is in a

Fluence	Bias Voltage	Lorentz angle at 3 T
0 n_{eq}/cm^2	150 V	$17.2° \pm 1.3°$
2×10^{14} n_{eq}/cm^2	200 V	$16.0° \pm 1.0°$
6×10^{14} n_{eq}/cm^2	400 V	$11.9° \pm 1.0°$

Table 4.6. The Lorentz angle measured with the angle scan method for p–spray design.

good agreement with the Lorenz angle measured using the grazing angle method (Table 4.7).

4.5.2. Lorentz angle with the grazing angle method

The Lorentz angle is obtained by the direct measurement of the charge carriers displacement in a 3 Tesla magnetic field using the grazing angle method. The average signal as a function of the distance to the beam exit point is shown in Fig. 4.26(a) for the unirradiated p–spray sensor.

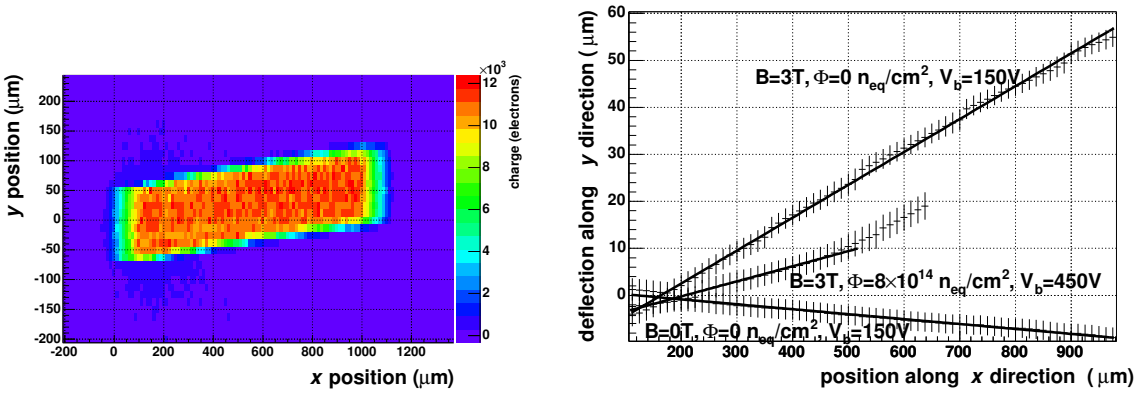

(a) (b)

Figure 4.26. a) Deflection of the collected charge in a 3 T magnetic field. b) Deflection of the collected charge as a function of the x position. The solid line represents the linear fit to the measured values.

The angle β is measured by creating slices of the plot perpendicular to the x–axis. The position of the center of each slice is shown in Fig. 4.26(b) as a function of position along the x–axis. A measurement without magnetic field is used to correct for the detector misalignment with respect to the beam (bottom line in Fig. 4.26(a)). For the irradiated device in Fig. 4.26(b) there are two regions which have different slopes, hence two different values of the Lorentz angle. This behavior was already noticed in [27, 9]. The difference in the Lorentz angle can be explained by the behavior of the electric field which reaches maximum values near both surfaces of the sensor (Section 4.6). As most of the charge is collected from the region close to the pixel implant, the average Lorentz angle shown in Fig. 4.27 is measured for the region close to the pixel implant. In Fig. 4.27 the measured Lorentz angle is shown for both unirradiated and irradiated sensors scaled from the measured at 3 T to 4 T using the Equation 2.16 which corresponds to the CMS case. A strong dependence of the Lorentz angle on the electric field is observed weakly affected by the irradiation or sensor design. With the unirradiated sensors a Lorentz angle of 26° can be reached at a bias voltage of 100 V, while irradiated sensors have to be operated at higher bias voltages, where the Lorentz angle drops to 10°. Since the electron mobility increases with decreasing temperature the Lorentz angle measured at the lower temperature of −20° C is 1° to 2° larger. The values of the Lorentz angle are also in a good agreement with previous measurements and simulations in [28, 29]. In these works the Lorentz angle in the unirradiated sensor for electrons is 30° at 4 T magnetic field and bias voltage of 40 Volts. After irradiation and increasing bias voltage up to 100 V the Lorentz

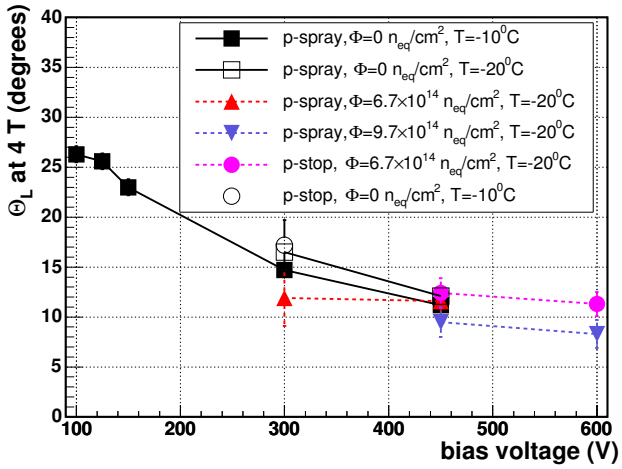

Figure 4.27. Lorentz angle as a function of the bias voltage for 4 T magnetic field in the region closer to the pixel implant.

angle decreases by 25 %.

The p–spray design sensors will be used in the pixel barrel part of the detector where the Lorentz angle improves the charge sharing. The Lorentz angle measurements for the p–spray sensor design are summarized in the Table 4.7.

Fluence	Bias Voltage	Lorentz angle at 4 T grazing angle method	Lorentz angle at 4 T angle scan method
0 n_{eq}/cm^2	100 V	$26.3° \pm 0.8°$	
0 n_{eq}/cm^2	125 V	$25.6° \pm 0.8°$	
0 n_{eq}/cm^2	150 V	$23.0° \pm 0.8°$	
0 n_{eq}/cm^2	150 V		$22.4° \pm 1.7°$
0 n_{eq}/cm^2	300 V	$14.7° \pm 0.6°$	
0 n_{eq}/cm^2	450 V	$11.2° \pm 0.6°$	
2×10^{14} n_{eq}/cm^2	200 V		$20.9° \pm 1.4°$
6×10^{14} n_{eq}/cm^2	400 V		$15.6° \pm 1.3°$
6.7×10^{14} n_{eq}/cm^2	300 V	$11.9° \pm 2.8°$	
6.7×10^{14} n_{eq}/cm^2	450 V	$11.6° \pm 1.4°$	
9.7×10^{14} n_{eq}/cm^2	450 V	$9.5° \pm 1.5°$	
9.7×10^{14} n_{eq}/cm^2	600 V	$8.3° \pm 1.4°$	

Table 4.7. The Lorentz angle in p–spray type sensor measured with grazing angle and angle scan methods.

4.6. Measurements of electric field and mobility

4.6.1. Measurement technique

We now describe a refined method to determine Θ_L as a function of depth. The following measurements are based on the grazing angle technique explained in Section 4.5. The beam enters the pixel plane at a shallow angle α =15° and the 3 T magnetic field is parallel to the beam as shown in Fig. 4.28(a). The position of the beam exit point "O" is reconstructed in the

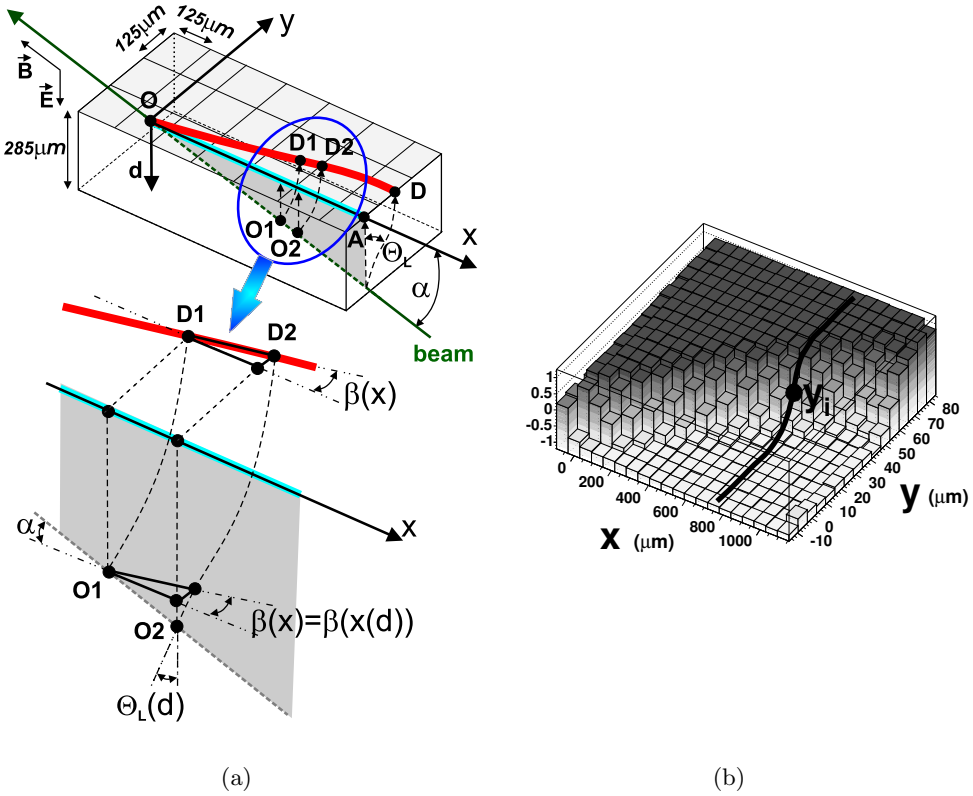

(a) (b)

Figure 4.28. a) The deflection measurement technique. b) Asymmetry as a function of position in the xy plane for unirradiated sensor.

pixel coordinates system using the beam telescope. In the absence of magnetic field electrons and holes produced by the traversing particles drift toward the electrodes. The electrons move toward the n^+ side and are collected along the segment $\overline{OA}$. The holes move in the opposite direction and, together with the electrons, induce the net current on the pixels situated along $\overline{OA}$. In the presence of a magnetic field charge carriers are deflected by the Lorentz force and the resulting current is induced on the pixels along the segment $\overline{OD}$. This measurement technique was developed in [27] and used to measure the average Lorentz angle Θ_L by fitting the deflection $\overline{OD}$ with a straight line [9]. In case of irradiated sensor, the segment $\overline{OD}$ is curved, because the Lorentz angle depends on the electric field, which changes over the depth. This technique is used for measuring the Lorentz angle as a function of sensor depth. The bottom part of Fig. 4.28(a) shows the definition of $\beta(x)$ for an infinitely small section of the

segment $\overline{\mathrm{OD}}$. Knowing the beam incident angle α=15° and the deflection angle $\beta(x)$ the Lorentz angle at a certain depth $\Theta_L(d)$ is given by

$$\tan\Theta_L(d) = \frac{\tan\beta(x(d))}{\tan\alpha}. \tag{4.2}$$

Therefore, the Lorentz angle is calculated in each point in depth with the tangent to the segment $\overline{\mathrm{OD}}$. The geometrical position of the segment $\overline{\mathrm{OD}}$ in the xy plane can be determined from the signal asymmetry of two neighboring pixels. The asymmetry at the (x, y) position is defined as

$$A(x, y) = (Q_{x,y+p} - Q_{x,y})/(Q_{x,y+p} + Q_{x,y}),$$

where $Q_{x,y}$ and $Q_{x,y+p}$ are the charges collected in pixels, centered at (x, y) and $(x, y + p)$, respectively, and $p = 125$ µm is the pixel size. The asymmetry is averaged over all events in each (x, y) bin and is shown in Fig. 4.28(b). The asymmetry plot was divided into slices along the x axis. The i–th slice located at x_i (e.g. represented by the solid line in Fig. 4.28(b)). An example of asymmetry as a function of y at a fixed x_i position is shown in Fig. 4.29. For each

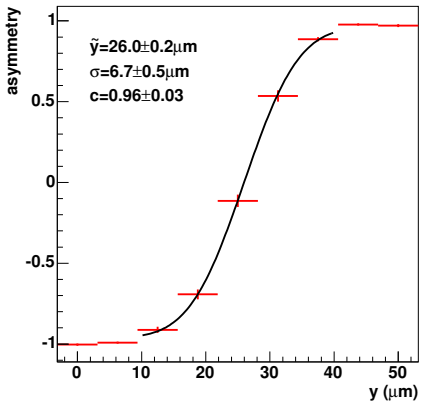

Figure 4.29. Red markers represent the asymmetry. The solid curve is the fit. The parameter $\tilde{y}$ is the position along y, where the asymmetry is zero. The other parameters are from Equation 4.3

slice at x_i point the $A(y)$ was fitted with the function

$$A(y) = c \times \sqrt{\frac{2}{\pi}} \int_{-\infty}^{(y-\tilde{y})/\sigma} e^{-t^2/2} dt - c, \tag{4.3}$$

where the parameter $\tilde{y}$ corresponds to the zero asymmetry position along the y coordinate, c and σ are the constant and spread parameters of the fit. For each slice at x_i position the $\tilde{y}_i$ was determined. The set of points ($\tilde{y}_i$,x_i) determines the segment $\overline{\mathrm{OD}}$. For the measurement of the angle β the location of the segment $\overline{\mathrm{OD}}$ on the pixel plane is not important. The slight rotation (the line $\overline{\mathrm{OA}}$ can be rotated with respect to the pixel row) of the sensor in the xy plane was subtracted using the data without magnetic field. Each point x_i corresponds to a certain depth via the relation $d_i = x_i \tan\alpha$ and the deflection $\tilde{y}_i$ can be expressed as a function of depth. The points $\tilde{y}_i$ were fitted with a 5–th order polynomial function $P_5(d)$ as shown in

Fig. 4.30 in order to obtain smooth derivative, which is needed for calculation of the Lorentz angle.

The signal is induced on the pixels along the segment $\overline{\text{OD}}$ (Fig. 4.28(a)). Since the electric field in irradiated sensors is not linear, the segment between the points "O" and "D" is curved, and in each point its tangent determines the deflection angle β. The deflection $\tilde{y}$ as a function of the depth d in the silicon bulk is shown in Fig. 4.30 for different fluences and bias voltages. It

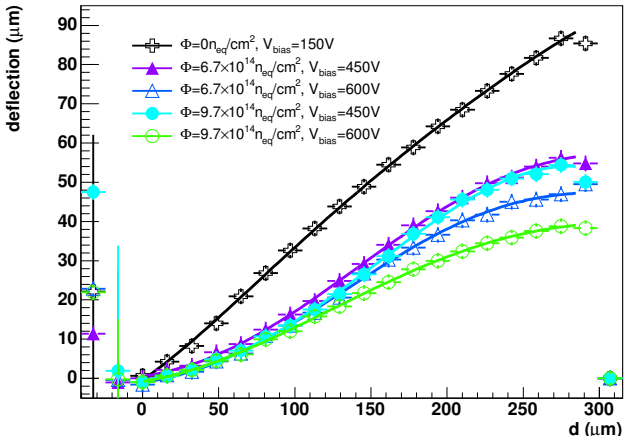

Figure 4.30. Lorentz deflection ($\tilde{y}$) of the charge in the magnetic field of 3 T$\times cos15°$ as a function of the depth. The solid lines are 5–th order polynomial fit functions.

must be noticed, that at the edges of the silicon bulk (d $<$ 17 μm or d $>$ 268 μm) the measured deflection has high systematic uncertainties (not shown in Fig. 4.30) due to the geometrical distortions of the electric field lines and incorrect reconstruction of the deflection curve $\overline{\text{OD}}$.

The Lorentz angle is found from the derivative (i.e. $\tan\beta(d)$ in Equation 4.2) of the polynomial fit $P_5(d)$ (Fig. 4.30) over d. The Lorentz angle as a function of depth is shown in Fig. 4.31. The Lorentz angle depends on the depth because of the mobility and electric field

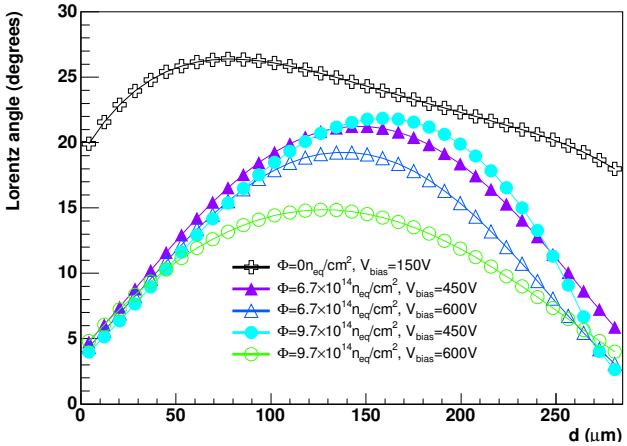

Figure 4.31. Lorentz angle as a function of the depth recalculated for 4 T magnetic field.

depends on the depth. Since the electric field is not uniform in irradiated sensors, the Lorentz

angle variation is also large, from 5°C to 20°C.

4.6.2. Electric field strength across the silicon bulk

Using the measured Θ_L (shown in Fig. 4.31 and Equation 4.2) and assuming that most signal is due to electrons as shown below (Fig. 4.36(b)), one can calculate the electron mobility as a function of the depth

$$\mu_e(d) = \frac{\tan\Theta_L(d)}{r_h B}, \tag{4.4}$$

where $r_h = 1.15$ is the Hall factor[5] for electrons and $B = 4$T. The measured electron mobility

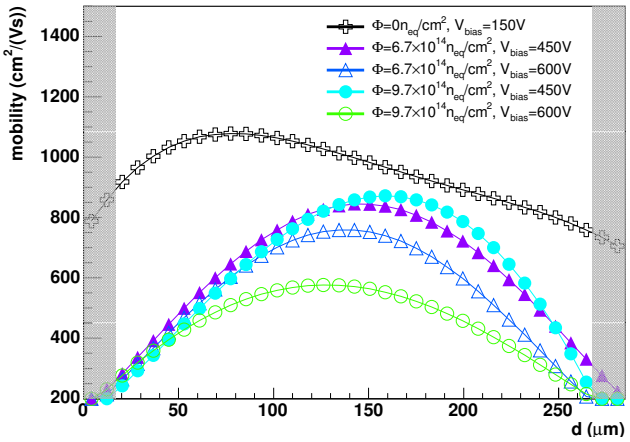

Figure 4.32. Measured electrons mobility as a function of depth for different fluences and bias voltages. The shaded regions correspond to the depth values where the mobility has large systematic uncertainties.

as a function of the sensor depth is shown in Fig. 4.32 for different fluences and bias voltages. Using an empirical parameterization of the field dependence of the electron mobility [14], one can derive the electric field as a function of depth

$$E(d) = E_{ce}\left[\left(\frac{\mu_{0e}}{\mu_e(d)}\right)^{\gamma_e} - 1\right]^{1/\gamma_e}, \tag{4.5}$$

where μ_e is the measured electron mobility, μ_{0e} low electric field electron mobility, E_{ce} the critical electric field and γ_e are known empirical parameters from [14]. Fig. 4.33 shows the electric field obtained by neglecting the electric field lines distortion close to the pixel implants. The measurement is restricted to the depth range 17 µm <d< 268 µm for the reasons explained in Section 4.6.1. For the unirradiated sensor the electric field is close to the classical linear field of an abrupt p–n junction. For the heavily irradiated sensors the electric field has a double peak with a distinct minimum close to the middle of the bulk. The origin of the double–peak electric field is qualitatively described in [20]. A model producing a doubly–peaked electric field was implemented in a detailed detector simulation and the simulated charge collection was found to be in good agreement with the measurements [30, 31]. By integrating the electric field

[5]The Hall factor is the ratio between the drift and the Hall mobilities.

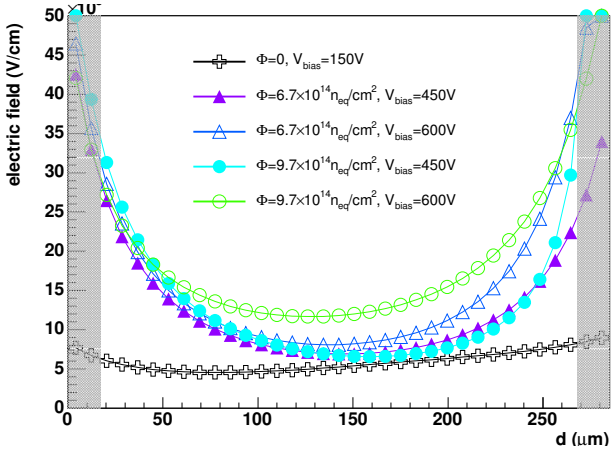

Figure 4.33. Electric field as a function of depth for the unirradiated and irradiated silicon sensors at different bias voltages. The shaded regions correspond to the depth values where the electric field has large systematic uncertainties.

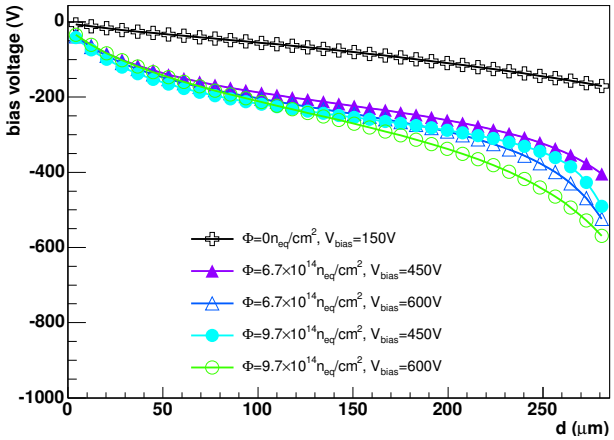

Figure 4.34. Calculated potential across the silicon bulk as a function of depth for the unirradiated and irradiated silicon sensors at different biases.

over depth one can determine the potential drop across the silicon bulk as shown in Fig. 4.34. The potential drop agrees with the applied bias voltage within 15% for all sensors.

4.6.3. Cross–check of the measured electric field

To check the measured electric field a simulation of the signal induced in the pixels was performed. The particle crossed the silicon sensor with an angle $\alpha = 15°$ (Fig.4.28(a)) and the energy loss was assumed to be uniformly distributed. Neither energy loss fluctuation nor charge diffusion was taken into account. In this simulation the electric field lines were assumed to be perpendicular to the silicon sensor planes and the electric field value as function of the depth was taken from the measurement shown in Fig. 4.33. The time dependence of the

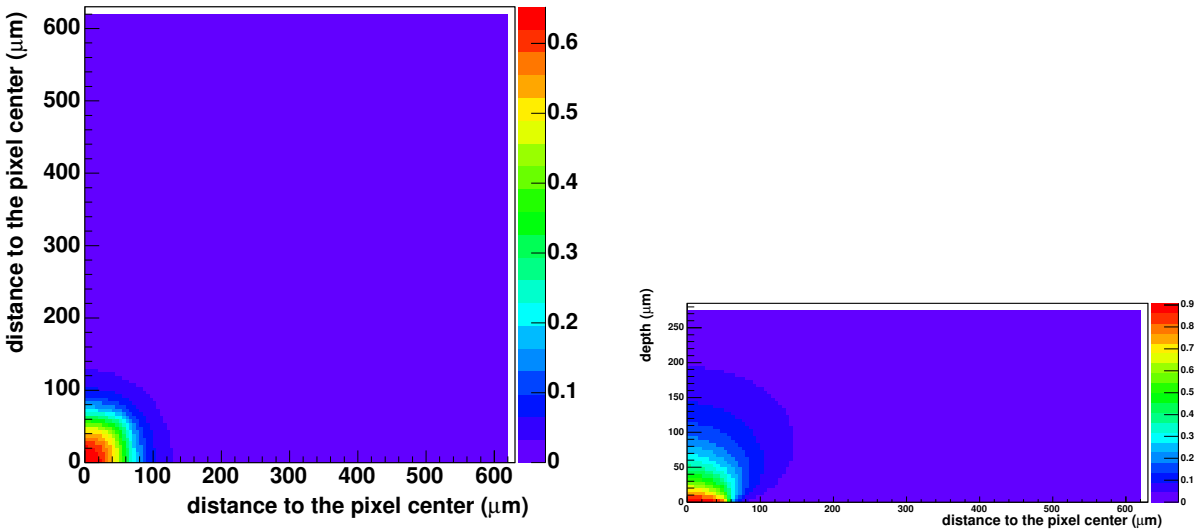

(a) (b)

Figure 4.35. a) Planar section of the effective potential at a depth of 50 μm in the silicon bulk. The pixel center is located at (0,0). The color scale is in Volts.
b) Transversal section of the effective potential. The pixel center is located at (0,0). The color scale is in Volts.

induced current was calculated using the Shockley–Ramo theorem [15, 16]

$$\begin{aligned} i(t) &= Q_h(t)\vec{E}(d(t)) \cdot \vec{v}_h(d(t)) + \\ & \quad Q_e(t)\vec{E}(d(t)) \cdot \vec{v}_e(d(t)), \end{aligned} \tag{4.6}$$

where Q_h and Q_e are the holes and electrons charges deposited by the particle energy loss,$\vec{E}$ is the effective field, $\vec{v_h}$ and $\vec{v_e}$ the holes and electrons drift velocities, respectively. The drift velocity was calculated using the measured electric field. The electrons and holes are trapped during the drift time according to the exponential laws

$$Q_h(t) = Q_{0h}e^{-t/\tau_h}, \quad Q_e(t) = Q_{0e}e^{-t/\tau_e}, \tag{4.7}$$

where τ_h and τ_e are the trapping constants. The trapping constants fluence dependence was taken from [19]. The effective potential used in Equation 4.6 for one pixel is shown in Fig. 4.35(a) and 4.35(b).

The induced signal was calculated separately for holes Fig. 4.36(a)) and electrons Fig. 4.36(b)) taking into account the Lorentz force. The contribution from holes is significant only at the region close to the pixel implant while the total induced current is dominated by the electrons. The total induced signal is shown in Fig. 4.37(a). Fig. 4.37(b) shows the measured and simulated deflection as a function of depth. The charge deflection predicted by the simulation reproduces the measurements well. The simulation was also performed without magnetic field

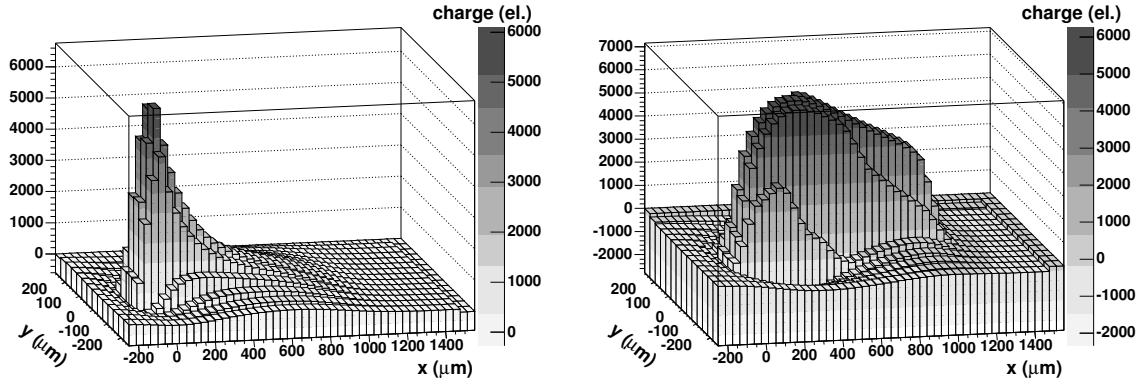

(a) (b)

Figure 4.36. a) Simulated signal induced by holes.
b) Simulated signal induced by electrons in a magnetic field of 3 T. The signal from electrons dominates the total signal.

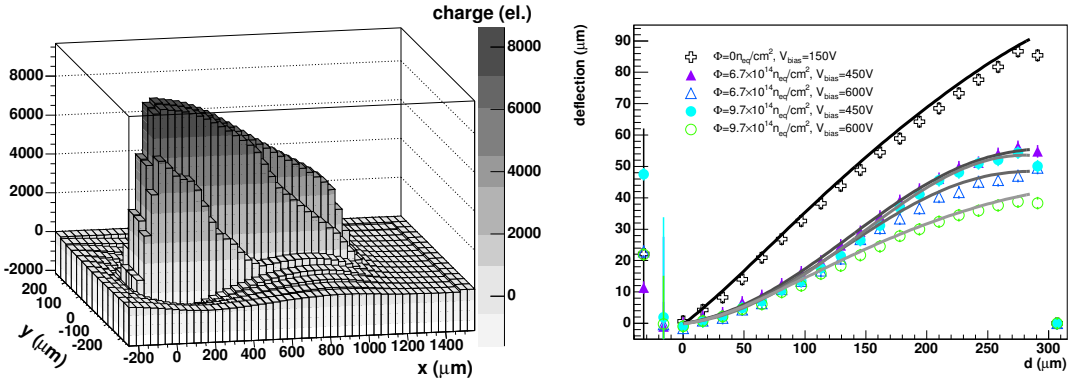

(a) (b)

Figure 4.37. a) Simulated total induced signal along the particle track projection with a magnetic field of 3 T. b) Measured (markers) and simulated (solid lines) deflection as a function of depth for different fluences and bias voltages.

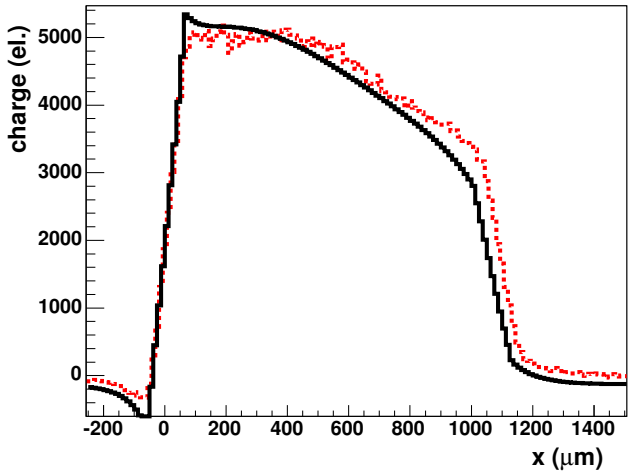

Figure 4.38. Measured (dotted line) and simulated (solid line) collected charge along the particle track for a sensor irradiated at $6.7\times10^{14}\,n_{eq}/cm^2$.

to compare the charge collection with the measurement. The simulation reproduces the measured values very well (Fig. 4.38). The small discrepancies might be due to charge diffusion, fluctuations in energy deposition and electric field distortion between pixel implants. The simulation did not account for these processes.

4.7. Summary

Several designs of the CMS prototype pixels sensors were tested up to 600 V bias voltage and after exposure to particle fluences up to 2.6×10^{15} n_{eq}/cm^2. The unirradiated sensors are depleted at a bias voltage below 100 V and the Lorentz angle is 26° at 4 Tesla magnetic field. The particle fluence of about $6\times10^{14}\,n_{eq}/cm^2$ corresponds to first four years of detector operation. After exposition to a fluence of $6\times10^{14}\,n_{eq}/cm^2$ the bias voltage will have to be increased to about 450 Volts. At this fluence:

- The leakage current increases up to about 1×10^{-6} A per single pixel.
- The maximum charge collection efficiency is 70% and it depends on the charge deposit position in the pixel area.
- The signal–to–noise ratio is very high, up to 50.
- The particle detection efficiency at a threshold of 2000 electrons (about 0.1 minimum ionizing particle signal) is above 95% for p–stop design and 99% for p–spray design.
- The Lorentz angle is 12° ±3° .

A method to measure the electric field through the bulk of irradiated silicon pixel sensors was presented. The method is based on a precise measurement of the Lorentz deflection as a function of depth in the silicon sensor bulk. The measured electric field was checked by a

sensor simulation which reproduces satisfactory both the charge collection and the Lorentz deflection.

5. CMS pixel detector resolution

The performances of the silicon sensors described in the previous chapter are used to perform a realistic simulation of the CMS pixel detector which will have $100\times150\mu m^2$ in a magnetic field of 4 T. The simulation is compared with test beam data and the resolution of the CMS pixel detector is estimated for the unirradiated sensors and fluences up to $9.7\times10^{14}\,n_{eq}/cm^2$. The geometry of a CMS pixel barrel module implemented in the simulation is shown in Fig. 5.1. The colliding proton beams are parallel to the magnetic field. The angle ϕ is the azimuthal

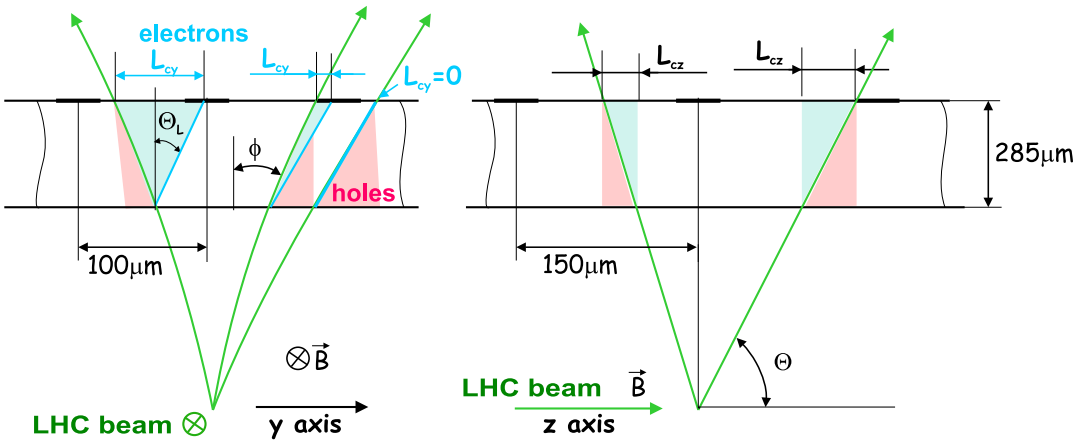

Figure 5.1. CMS pixel barrel module geometry. Transverse to the magnetic field (left) and parallel to the magnetic field (right).

angle, which is in the range of $\pm10°$. The range is determined by the width of the module and the radius of the barrel layer. The length of the charge spread L_{cy} is determined by the Lorentz force and the azimuthal angle. Depending on the position of the incoming particle and the length L_{cy}, the charge can be spread on several pixels. In the right part of Fig. 5.1 the projection along the beam direction is shown. The angle Θ is the polar angle which can be as small as $10°$ for the innermost barrel layer. Since there is no Lorentz force along the beam direction (z axis) the charge spread along this direction L_{cz} only depends on Θ.

5.1. Sensor simulation

The purpose of the simulation is to predict the spatial resolution of a pixel sensor of 100×150 μm^2 pitch size in a 4 T magnetic field for different azimuthal and polar angles. The sensor used in the beam test (pixel size 125×125 μm^2) was also simulated in a 3 T magnetic field in order

to validate the simulation. The physical properties of the silicon sensors were measured and

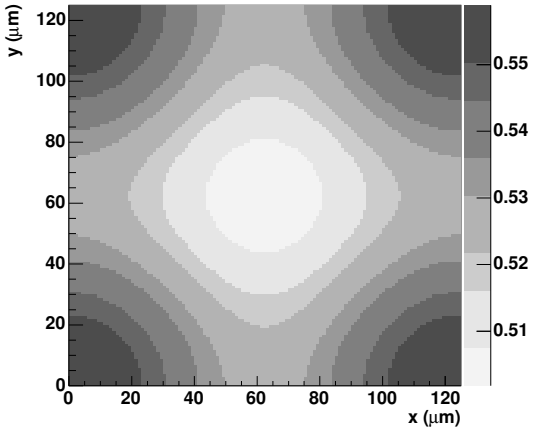

Figure 5.2. Drift potential in the pixel plane at a depth of 60 μm. The gray scale is in Volts.

described in Chapter 4. The electric field, the charge carriers mobilities as well as the Lorentz angle only weakly depend on the pixel pitch and can be therefore used in the simulation.

The Lorentz angle at 4 T magnetic field is obtained from the measurements (Fig. 4.31). The non–linearity and the noise of the preamplifier is also taken from the measurements. The distribution of the noise is Gaussian with a r.m.s. of 350 electrons, while the non–linearity of the preamplifier is taken from Fig. 3.6).

The path of the particle in the sensor bulk is divided into steps and the energy loss fluctuations in each step are simulated with a Landau distribution (Equation 2.5). The energy loss δE is smeared with 3μm around the particle trajectory in order to take into account low energy secondary electrons. The high energetic δ–electrons are not taken into account. The energy for an electron–hole pairs creation is taken as 3.6 eV, therefore the number of pairs is

$$N = \frac{\delta E}{3.6\,\mathrm{eV}} \tag{5.1}$$

The distribution of the number of the created electron–hole pairs N is assumed to be Gaussian but the Fano factor F is fixed to 0.12

$$\frac{\delta N}{N} = \sqrt{\frac{F}{N}} \tag{5.2}$$

The drift field is assumed to be flat, with field lines perpendicular to the pixel planes and its value is taken from the measurements discussed in Section 4.6.2. This assumption simplifies the simulation process, since the equations of the charge carrier motion are solved analytically. However, corrections are applied to account for field line focusing at the pixel implants.

The electrons and holes are propagated through the sensor bulk using the mobilities and velocities given in Eqs. 2.9 and 2.10. The Lorentz angle is calculated with these mobilities and the given magnetic field. The current induced on the pixel electrodes is calculated using the Ramo–Shockley theorem, Eq. 2.17. For the irradiates sensors the charge carriers are trapped according to the exponential law, Eq. 2.19, and the trapping times for electrons and holes are

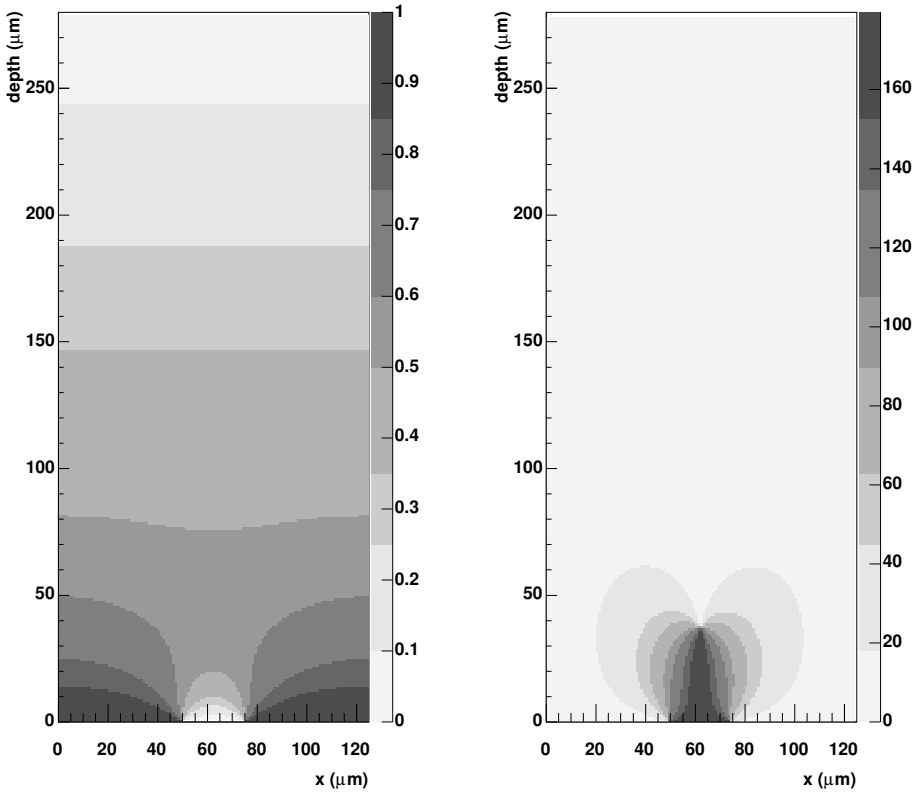

(a) (b)

Figure 5.3. a) The transversal view of the drift potential. The gray scale is in Volts. b) The angle (degrees) between the drift field lines and the direction perpendicular to the pixel plane. The gray scale is in degrees.

taken from [19]. Fig. 5.2 shows the drift potential in the plane parallel to the sensor surface at a depth of 60 μm for a 125×125 μm^2 pixel size. The center of the pixel is located at (0,0) and the applied voltage is 1 V. The transversal projection of the potential is shown in Fig. 5.3(a). The potential is non–uniform in the regions close to the pixel implants. The drift field lines are bent and for depth below 50 μm the assumption of parallel field lines is not valid. The angle between the drift field lines and the direction perpendicular to the pixel plane is shown in Fig. 5.3(b). Clearly, the drift angle for depths smaller than 50 μm is larger than the Lorentz angle and the charge carriers are captured by the nearest pixel. Therefore the charge carriers reaching the region between pixels at this depth are captured by the nearest pixel. In addition, the electric field in the inter–pixel region is larger and the Lorentz angle decreases. To take into account these effects a cut–off parameter of 58 μm is introduced. If the charge carrier position is below this cut–off depth, the Lorentz force is assumed to be zero. This cut–off

parameter was optimized by adjusting the simulated spatial resolution to the measured one. The value found with this procedure agrees well with what expected from the Fig. 5.3(b).

5.2. Measured spatial resolution of the p–spray sensors

The resolution is obtained by comparing the position reconstructed with the pixel detector to the beam telescope prediction. The precision of the beam telescope is about 1 μm. The

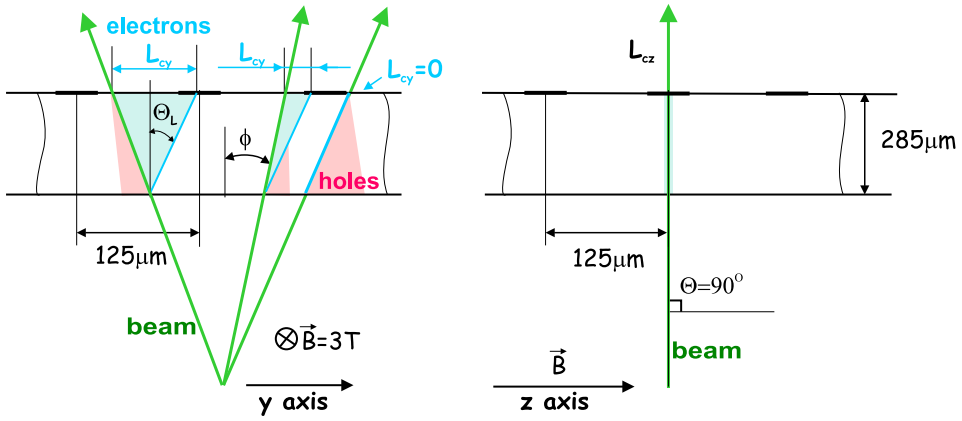

Figure 5.4. Test beam geometry. Transverse to the magnetic field (left) and parallel to the magnetic field (right).

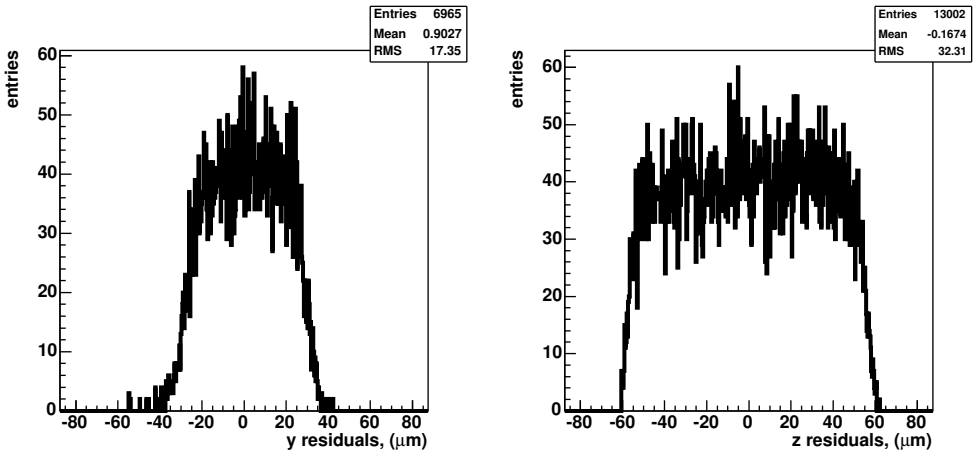

Figure 5.5. The distribution of the residuals between the position predicted by the beam telescope and pixel for one–pixel cluster events along the y (left) and z (right) directions. The azimuthal angle ϕ is zero and the polar angle is 90° . The pixel size is 125×125 μm^2 and the magnetic field 3 T. Because of the charge spread due to the Lorentz force the region of one–pixel cluster events is smaller and hence the resolution is better along the y direction.

resolution is measured separately along and perpendicular to the Lorentz deflection, the y and z directions respectively (Fig. 5.4). The azimuthal angle ϕ varied in the range from -20° to 30° . The resolution along the z direction measured for perpendicular to the sensor surface tracks. The pixel size, 125×125 μm^2, and the 3 T magnetic field are also shown in Fig. 5.4. A pixel threshold of 2000 electrons is applied to find hits in the pixel sensor. The events are

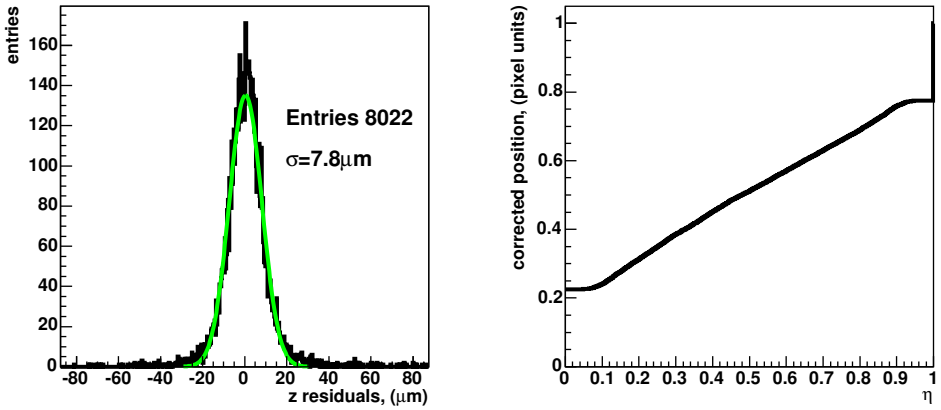

Figure 5.6. The residuals distribution for two–pixel cluster along the y direction (left) and η correction function (right). The azimuthal angle ϕ is zero and the polar angle is 90° . The pixel size is 125×125 μm^2 and the magnetic field 3 T. The charge sharing is due to the Lorentz force. The number two–pixel events is about 55% of total number of events.

divided into the clusters of one and two pixels. If more than one pixel above threshold is found and the pixels are adjacent, the position is reconstructed using the a center of gravity algorithm. For the two–pixel cluster an η correction algorithm (Section 3.2.4) is applied.

The residuals are defined as the difference between the positions predicted by the beam telescope and the ones reconstructed with the pixel. In the case of one–pixel clusters the standard deviation, or r.m.s., of the residuals distribution is calculated. In the case of two–pixel clusters the distribution of residuals is fitted with a Gaussian.

Examples of the residuals distribution for the unirradiated p–spray sensor at a bias voltage 150 V are shown in Fig. 5.5, 5.6, 5.7. The azimuthal angle ϕ is zero degrees and the polar angle is 90° .

The residuals for one–pixel cluster events along the y and z directions are shown in Fig. 5.5. The residuals distribution along the y direction for two–pixel clusters is shown in the left part of Fig. 5.6. In the right part of Fig. 5.6 the η correction function is shown. The residuals distribution along the z direction and η correction function are shown in the left and right part of Fig. 5.7, respectively. The resolution is defined as the square root of weighted sum of the squared r.m.s of the residuals distribution for one–pixel clusters and the squared σ of the Gaussian fit for the two–pixel clusters. The weights are given by the fractions of one– and two–pixel clusters. Neglecting the resolution of the beam telescope, the resulting sum is used as an estimate of the sensor resolution.

The resolution is shown in Fig. 5.8 as a function of the azimuthal angle ϕ for the unirra-

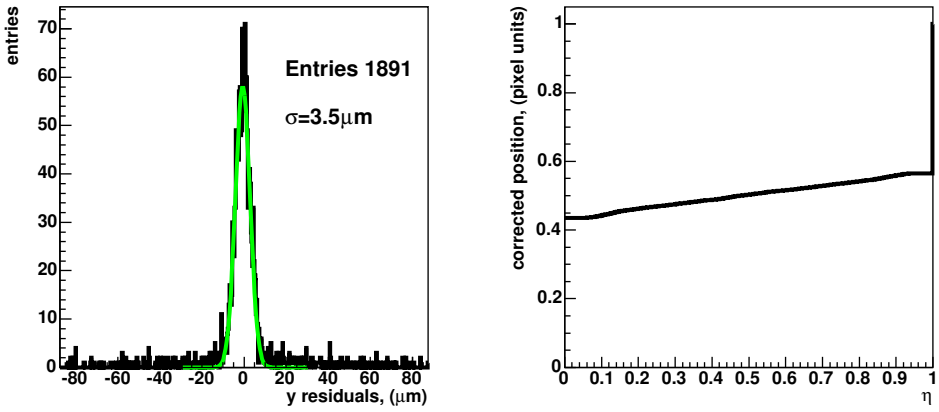

Figure 5.7. The residuals distribution for two–pixel cluster along the z direction (left) and η correction function (right). The azimuthal angle ϕ is zero and the polar angle is 90°. The pixel size is 125×125 μm^2 and the magnetic field 3 T. The charge sharing due to the diffusion. The number two–pixel events is about 13% of total number of events.

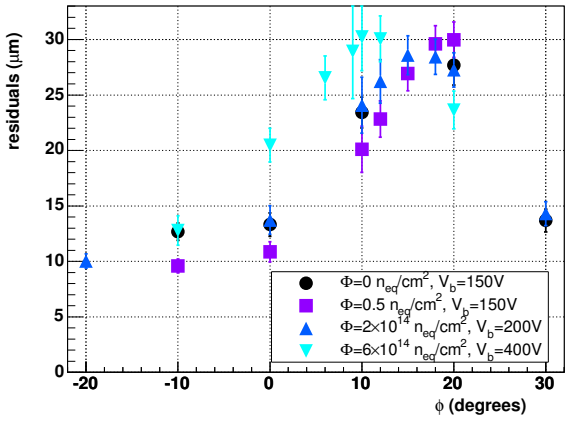

Figure 5.8. Resolution as a function of the azimuthal angle ϕ for unirradiated and irradiated sensors. The polar angle Θ is set to 90 degrees. The pixel size is 125×125 μm^2 and the magnetic field 3 T.

diated and irradiated sensors. The polar angle is 90°. The resolution depends on the angle ϕ and on the charge spread due to the Lorentz force. The best resolution is obtained for ϕ ∼-10° and can be achieved even with the heavily irradiated sensors.

5.3. Comparison of the measured and simulated spatial resolution

The beam test conditions are simulated (geometry in Fig. 5.4) and residuals distributions are compared with the measured ones. The resolution of the beam telescope in the simulation is

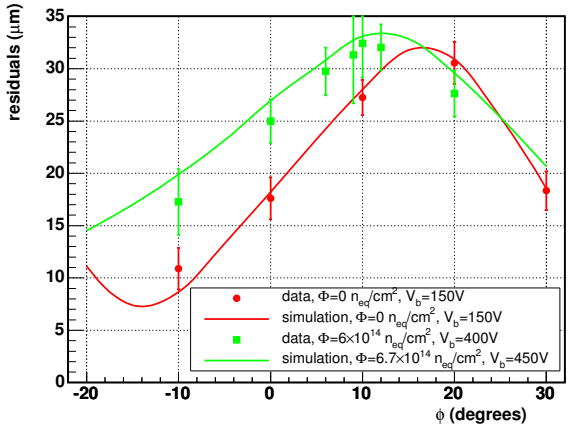

Figure 5.9. Standard deviation of the residuals distribution as a function of the azimuthal angle ϕ for measured and simulated one–pixel cluster events. The polar angle Θ is 90° and the magnetic field 3 T. The pixel size is 125×125 μm^2.

fixed to 1 μm. The beam entry point is uniformly distributed over the pixel area. The com-

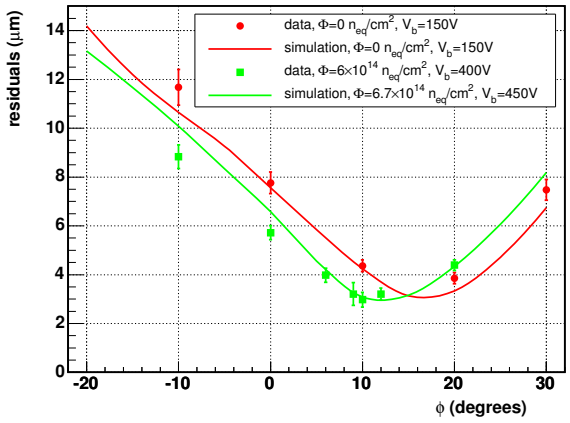

Figure 5.10. Sigma of the Gaussian fit of the residuals distribution as a function of the azimuthal angle ϕ for measured and simulated two–pixel cluster events. The polar angle Θ is 90° and the magnetic field 3 T. The pixel size is 125×125 μm^2.

parison of the standard deviation of the residuals distribution for one–pixel clusters is shown in Fig. 5.9 for unirradiated and irradiated sensors. The simulation describes the measured resolution very well. Fig. 5.10 shows the comparison of the sigma the residuals distribution for

two–pixel clusters. The comparison of the resolution is shown in Fig. 5.11. The data measured

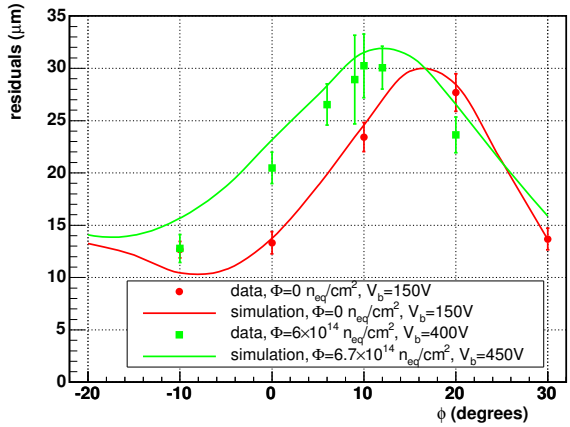

Figure 5.11. Total residuals (weighted sum of one–pixel and two–pixel clusters) as a function of the azimuthal angle ϕ for measured and simulated events. The polar angle Θ is 90° and the magnetic field 3 T. The pixel size is 125×125 μm^2.

with the sensor irradiated at 6×10^{14} n$_{eq}$/cm^2 are compared to a simulation with slightly higher fluence and bias voltage. In fact, the electric field used in the simulation was obtained for a sensor irradiated at 6.7×10^{14} n$_{eq}$/cm^2 and a bias voltage of 450 V. For the unirradiated sensor the simulation describes the data very well. For the irradiated sensor the description is satisfactory and the few discrepancies are due to the difference between simulated and measured samples. Since the simulation is validated by the measurements, it can be used to predict the resolution of the CMS pixel detector. The results are presented in the following section.

5.4. Predicted spatial resolution for the CMS pixel detector

The geometry of the CMS pixel sensors was implemented in the simulation described in Section 5.1. The magnetic field was set to 4 T. The purpose of this study was to estimate the response of the CMS pixel detector and to calculate the spatial resolution as function of the azimuthal and polar angles. In Fig. 5.12 the resolution along the y direction is shown as a function of the azimuthal angle ϕ, for two irradiation fluences and bias voltages. The angle Θ is set to 90°. The resolution at both fluences is optimum for a bias voltage of 450 V and this value is used hereafter for the irradiated sensors.

In Fig. 5.13 the resolution along the y direction is shown as a function of azimuthal angle ϕ for different irradiation fluences and polar angles Θ. The resolution weakly depends on the polar angle, the difference is less than 2 μm.

In Fig. 5.14 the resolution along the z direction is shown as a function of the polar angle. For each polar angle the resolution is averaged over the azimuthal angle in the range of $\phi = \pm10°$. Fig. 5.14 shows a strong dependence of the resolution along the z direction on the number of pixel crossed by the particle. At large polar angles one–pixel clusters dominate and the resolution is close to the binary 150 μm/$\sqrt{12}$. The resolution improves with decreasing

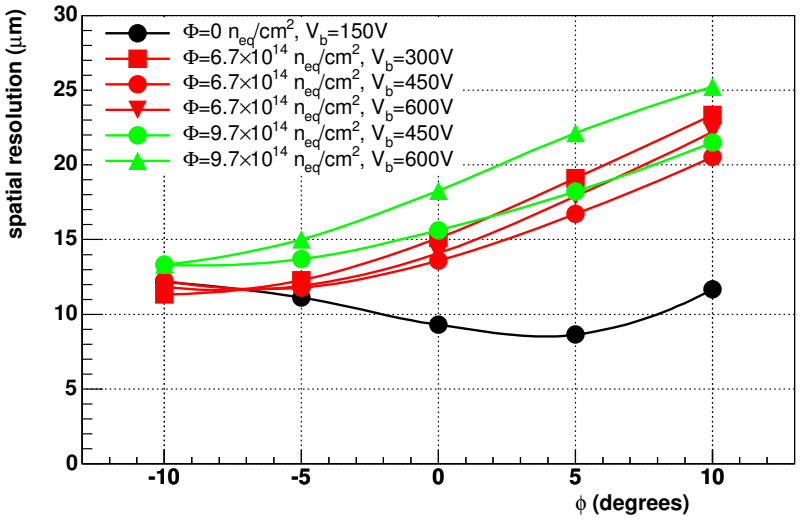

Figure 5.12. Predicted position resolution along the y direction as a function of the angle ϕ for different irradiation fluences and bias voltages. The pixel size is 100×150 μm^2. The magnetic field is 4 T.

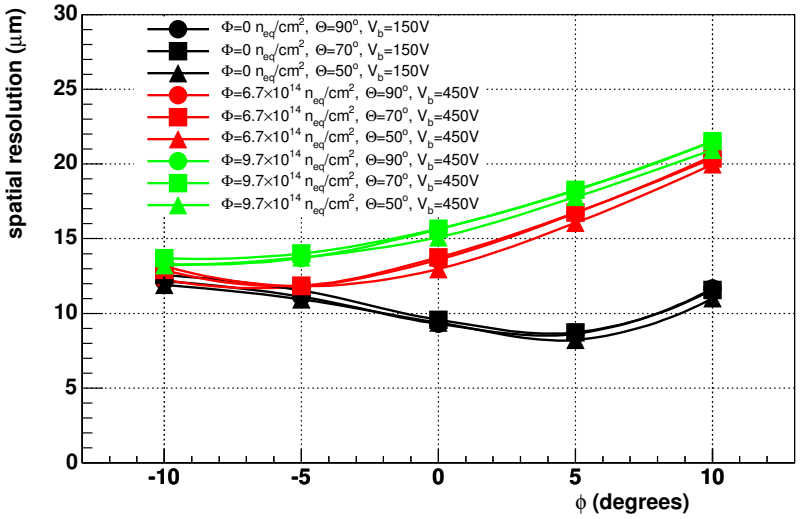

Figure 5.13. Predicted position resolution along the y direction as a function of the angle ϕ for different angles Θ and irradiation fluences. The optimum bias voltage is applied to the irradiated sensors. The pixel size is 100×150 μm^2. The magnetic field is 4 T.

polar angles. The improvement observed at $\Theta < 60°$ is due to the increase of the cluster size from one to two pixels.

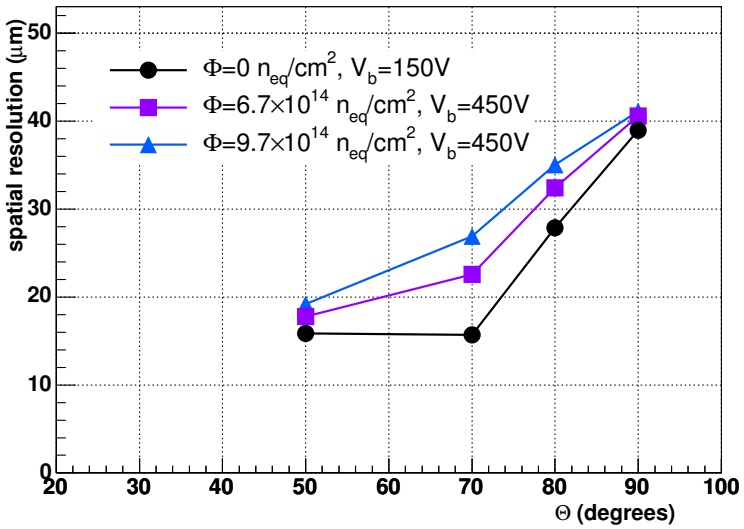

Figure 5.14. Position resolution along the z direction as a function of the angle Θ. The pixel size is 100×150 μm^2.

The simulation shows that the resolution along the y direction (azimuthal angle direction) is between 10 μm and 20 μm, depending on the irradiation fluence and the polar angle. After a fluence equivalent to the first four years of operation at the innermost barrel layer the resolution is still below 20 μm along the azimuthal angle direction and depends weakly on the polar angle. The resolution along the z direction is also below 20 μm if the particle crosses at least two pixels (small angle Θ), and is below 40 μm for the region of large angles Θ.

The resolution along the z direction depends very weakly on the irradiation fluence, while the resolution along the y direction depends on the irradiation fluence because of the Lorentz angle.

6. Conclusions

In this work the properties of the sensors designed for the CMS pixel detectors were measured before and after irradiation using high energy pions at CERN. The electric field in the silicon sensors was measured and its peculiar behavior after irradiation validated with a simulation. The simulation of the final CMS pixel geometry implements the measured properties of the silicon sensors. The resolution of the CMS pixel barrel module was then predicted for unirradiated and irradiated detectors. The results can be summarized as follows:

1. Pixel sensors can be operated up to an irradiation fluence of $10^{15} \mathrm{n_{eq}/cm^2}$, which is much higher than what was originally specified for the CMS pixel detector. The charge collection efficiency is about 60% of that for the unirradiated sensors after a fluence of $10^{15} \mathrm{n_{eq}/cm^2}$. This value drops to 25% after a fluence of $2.6{\times}10^{15}\,\mathrm{n_{eq}/cm^2}$. The first four years of LHC correspond to a fluence of $6{\times}10^{14}\,\mathrm{n_{eq}/cm^2}$ for the innermost detector layer.

2. Irradiated sensors show trapping of charge carriers and the bias has to be increased to 450 V to collect more charge and reach full depletion.

3. The charge collection efficiency is lower in the punch–through regions in the case of p–spray design. After irradiation an additional region of inefficiency arises along the biasing grid.

4. For the p–spray design the charge collection efficiency is higher than for the p–stop design.

5. The signal–to–noise ratio is about 70 for the unirradiated p–spray sensors, about 50 for the sensors exposed to a fluence of $6{\times}10^{14}\,\mathrm{n_{eq}/cm^2}$ and about 10 for the sensors at a fluence of $2.6{\times}10^{15}\,\mathrm{n_{eq}/cm^2}$.

6. For the unirradiated p-stop sensors the signal-to-noise ratio is about 35 for the design with two openings and about 50 for the design with one opening. In both cases it drops to 40 after a fluence of $6{\times}10^{14}\,\mathrm{n_{eq}/cm^2}$.

7. The p–spray and p–stop designs with two openings exposed to a fluence of $6{\times}10^{14}\,\mathrm{n_{eq}/cm^2}$ have a particle detection efficiency of 99% with a threshold of 2000 electrons. The respective value for the p-stop design with one opening is 95%. The p–spray design is preferred over the p–stop.

8. The Lorentz angle does not depend on irradiation or sensor design, but strongly depends on the bias voltage. The Lorentz angle with a magnetic field of 4 T is $26.3^\circ \pm 0.8^\circ$ for the unirradiated devices and a bias voltage of 100 V. It drops to $8.3^\circ \pm 1.4^\circ$ for the sensors irradiated at $10^{15} \mathrm{n_{eq}/cm^2}$ and a bias voltage of 600 V.

9. In the irradiated sensors charge is collected from both sides of the sensor bulk and the main contribution to the total signal is given by electrons. The measured electric field as a function of the detector depth has a minimum around the middle of the sensor bulk and increases at the edges.

10. A simulation of the sensors is in good agreement with the data. The resolution of the CMS pixel detector is estimated for the unirradiated sensors and for sensors irradiated up to $9.7\times10^{14}\,\mathrm{n_{eq}/cm^2}$. The r.m.s resolution along the $r\phi$ direction (azimuthal angle direction) is between 10 µm and 20 µm, depending on irradiation fluence and polar angle. After a fluence equivalent to the first four years of operation at the innermost barrel layer the resolution is still below 20 µm along the azimuthal angle direction and depends weakly on the polar angle. The resolution along the z direction is below 20 µm if the particle crosses at least two pixels ($\Theta < 60^\circ$), and is below 40 µm for large angles Θ. The resolution along the z direction depends weakly on the irradiation fluence. On the other hand, the resolution along the $r\phi$ direction strongly depends on irradiation fluence because of the change in the bias voltage and, consequently, in the Lorentz angle.

11. For the irradiated devices the charge collection, and therefore the signal height, increases with bias voltage but the Lorentz angle decreases. For this reason the bias voltage must be optimized for the best performance of the CMS pixel detector. The optimum bias voltage is 450 V for fluences from $6.7\times10^{14}\,\mathrm{n_{eq}/cm^2}$ to $9.7\times10^{14}\,\mathrm{n_{eq}/cm^2}$.

Bibliography

[1] C. Wulz, *CMS conference report*, CMS CR 2001/016.

[2] R. Rainwater, M. Spira and D. Zeppenfeld, *Higgs Boson Production at Hadron Colliders*, hep-ph/0203187.

[3] L. Silvestris, Nucl. Instrum. Meth. **A392**, 161 (1997).

[4] Particle Data Group, S. Eidelman *et al.*, Phys. Lett. **B592**, 1 (2004).

[5] *The tracker project, Technical design report*, CMS Collaboration, CMS TDR 5, CERN-LHCC-1998-06, 1998.

[6] M. Barbero *et al.*, Nucl. Instrum. Meth. **A517**, 349 (2004).

[7] RD48(ROSE), M. Moll, E. Fretwurst, and G. Lindstrom, Nucl. Instrum. Meth. **A439**, 282 (2000).

[8] T. Rohe *et al.*, IEEE Trans. Nucl. Sci. **51**, 1150 (2004).

[9] R. Kaufmann, *Development of radiation hard pixel sensors for the CMS experiment*, PhD thesis, University of Zürich, 2001.

[10] H. Bichsel, Rev. Mod. Phys. **60**, 663 (1988).

[11] L. Landau, J. of Phys. (U.S.S.R) **8**, 201 (1944).

[12] W. Boersch-Supan, J. Res Natl. Bur. Stand. , 245 (1961).

[13] C. Canali *et al.*, IEEE Transaction on Nuclear Science NS-19(4) (1972).

[14] N. Arora, J. Hauser, and D. Roulston, IEEE Trans. Electron Devices , 292 (1982).

[15] W. Shokley, J . Appl. Phys. 9 **9**, 635 (1938).

[16] S. Ramo, Proceedings of the IRE **27**, 584 (1939).

[17] R. Turchetta, Nucl. Instrum. Meth. **A335**, 44 (1993).

[18] M. Moll, *Radiation Damage in Silicon Particle Detectors, microscopic defects and macroscopic properties*, PhD thesis, University of Hamburg, 1999, DESY-THESIS-1999-040.

[19] G. Kramberger, V. Cindro, I. Mandic, M. Mikuz, and M. Zavrtanik, Nucl. Instrum. Meth. **A481**, 297 (2002).

[20] V. Eremin, E. Verbitskaya, and Z. Li, Nucl. Instrum. Meth. **A476**, 556 (2002).

[21] C. Amsler *et al.*, Nucl. Instrum. Meth. **A480**, 501 (2002).

[22] V. Dubacher, *Test of a silicon pixel detector with 50 GeV/c pions*, Diploma thesis, University of Zürich, 1996.

[23] M. Pernicka and H. Steininger , *Pixel readout,* Available at `http://wwwhephy.oeaw.ac.at/p3w/electronic2/ELEK2/ARCHIV/CMS/PIX_READ_SYS/pxrd_sys_js.html`.

[24] D.Meer, *Bau und Messen eines Multichip Pixelmodules als Prototyp für den CMS Traker*, Diploma thesis, ETH Zürich, 2000.

[25] M. Aleppo, Nucl. Instrum. Meth. **A465**, 108 (2000), physics/0012050.

[26] I. Johnson *et al.*, Nucl. Instrum. Meth. **A540**, 113 (2005).

[27] B. Henrich and R. Kaufmann, Nucl. Instrum. Meth. **A477**, 304 (2002).

[28] V. Bartsch *et al.*, Nucl. Instrum. Meth. **A478**, 330 (2002).

[29] V. Bartsch *et al.*, Nucl. Instrum. Meth. **A497**, 389 (2003), physics/0204078.

[30] M. Swartz, Nucl. Instrum. Meth. **A511**, 88 (2003).

[31] V. Chiochia *et al.*, submitted for publication to IEEE-TNS (2004), physics/0411143.

List of Figures

List of Tables

Acknowledgments

First of all I wish to thank Prof. Claude Amsler for giving me the opportunity to make a PhD study and for his constant support during my work.
I am also grateful all members of Zürich group: Yves Allkofer, Vincenzo Chiochia, Ian Johnson, Kirill Prokofiev, Hendrik Pruys, Christian Regenfus and Thomas Speer helping me in the measurements, analysis and for their very useful discussions and also for careful reading and corrections.
I wish also to thank for all peoples who helped in the beam test shifts: Daniela Bortoletto, Lucien Cremaldi, Susanna Cucciarelli, Dongwook Kim, Marcin Konecki, David Sanders, Seunghee Son and Morris Swartz.
This work would not be possible without the support from CMS pixel crew at PSI: Kurt Gabathuler, Roland Horisberger, Christoph Hörmann, Danek Kotlinski and Tilman Rohe. I thank them for introducing me to the pixels world, very useful discussions and for their help in preparing the tests and during the beam periods.
I also gratefully acknowledge the help from Silvan Streuli from ETH Zurich and Fredy Glaus from PSI for their immense effort on the bump bonding of the pixel sensors.
I would like to thank Maurice Glaser and Michael Moll from CERN for carrying out the irradiation, Kurt Bösiger from the Zürich workshop for the mechanical construction, György Bencze and Pascal Petiot from CERN for the H2 beam line support and finally the whole CERN-SPS team.
Finally I want to thank my family and all my friends for their great support and empathy.